ABSTRACT

Title of Dissertation:	PREPARATION OF A NANOSUSPENSION OF THE PHOTOSENSITIZER VERTEPORFIN FOR PHOTODYNAMIC AND LIGHT-INDEPENDENT THERAPY IN GLIOBLASTOMA
	John Andrew Quinlan, Doctor of Philosophy, 2024
Dissertation directed by:	Associate Professor Huang-Chiao Huang, Fischell Department of Bioengineering

Photodynamic therapy (PDT) using verteporfin (VP) has treated ocular disease for over 20 years, but recent interest in VP's light-independent properties has reignited interest in the drug, particularly in glioblastoma (GBM) (NCT04590664). Separate efforts to apply PDT to GBM using 5-aminolevulinic acid (5-ALA)-induced protoporphyrin IX (PpIX) have also garnered attention (NCT03048240), but, unfortunately, clinical trials using 5-ALA-induced PpIX-PDT have yet to yield a survival benefit. Previous studies have shown VP to be a superior PDT agent than 5-ALA-induced PpIX. Our lab has shown that 690 nm light activates VP up to 2 cm into the brain, while 635 nm light only activates PpIX at depths <1 cm into the brain. Additionally, VP is a more effective photosensitizer than PpIX because it has a higher singlet oxygen yield and is active in the vasculature as well as target tumor cells. However, the hydrophobicity of VP limits effective delivery of the drug to the brain for treatment of GBM.

In this context, this thesis aims to re-evaluate the delivery method for VP. VP traditionally requires lipids for delivery as Visudyne. Recent shortages of Visudyne and potential drawbacks of liposomal carriers motivated our development of a carrier-free nanosuspension of VP, termed NanoVP. Previous work has shown that cellular uptake of VP is greater when delivered as NanoVP rather than liposomal VP, resulting in improved cell killing after light activation.

This thesis builds on this previous work by (1) evaluating synthesis and storage parameters for NanoVP, (2) determining the pharmacokinetics, biodistribution, and brain bioavailability of NanoVP, and (3) evaluating the potential efficacy of NanoVP as a PDT and a chemotherapy agent, and by supporting development of a zebrafish model of the blood-brain barrier (BBB) for mechanistic studies of improved drug delivery to the brain.

PREPARATION OF A NANOSUSPENSION OF THE PHOTOSENSITIZER VERTEPORFIN FOR PHOTODYNAMIC AND LIGHT-INDEPENDENT THERAPY IN GLIOBLASTOMA

by

John Andrew Quinlan

Dissertation submitted to the Faculty of the Graduate School of the
University of Maryland, College Park, in partial fulfillment
of the requirements for the degree of
Doctor of Philosophy
2024

Advisory Committee:
Associate Professor Huang-Chiao Huang, PhD, Chair
Chief of Laboratory of Cell Biology Michael M. Gottesman, MD
Associate Professor Helim Aranda-Espinoza, PhD
Assistant Professor Jenna Mueller, PhD
Professor Wolfgang Losert, PhD, Dean's Representative

Disclosures

John Quinlan holds no financial interest in the work described here. Huang-Chiao Huang and Collin Inglut hold patents for an amorphous nanosuspension of verteporfin (NanoVP). Joel R. Walker and Wenhui Zhou are or were employees of Promega corporation and hold patents for furimazine and its analogs. Promega provided furimazine and its analogs for the research described here.

Acknowledgements

First, I would like to express my gratitude to my advisor, Huang-Chiao Huang, for his involvement throughout this experience, without which this thesis would not have been possible.

Many thanks to my NIH mentors, Michael Gottesman and Robert Robey, for your extensive support throughout this process. I learned an incredible amount about science and the context in which we work from you both, for which I am immensely grateful.

I would like to acknowledge the MPower Fellowship for supporting my first year of research, and the NCI-UMD Partnership for Integrative Cancer Research and the NIH Intramural Research Program for supporting subsequent years of research.

This work could not have been completed without significant support from lab mates both at UMD and NIH. Many thanks to Idrisa Rahman, Payal Srivastava, Carla Arnua del Valle, Shruti Vig, Chen-Hua Ma, Joanna Thomas, Crystal Lipsey, Sashank Sabbineni, and Michelle Kwarteng for your direct contributions to this project and for your support along the way. A huge thank you to Kaylin Baumiller and Anandita Gaur, two amazing undergraduates who were incredibly supportive and did excellent work to support this project. Working with you two was probably the most rewarding part of this experience for me. This project wouldn't have been possible without the excellent groundwork established by Collin Inglut and Barry Liang. Many thanks to UMD lab members Brian Schnoor, José Delgado, Sumiao Pang, Rebecca Johnson, Kathryn McNaughton, Kaitlyn Moore, Kassa Tizale, Sunniya Iftikhar, Aaron Sorrin, Anika Dasgupta, Nada Fadul, Renee Jaranson, Amber Baumiller, Anju Meda, Riley Schoch,

and Tanvi Kotta for fostering a learning environment that truly challenged me to grow. For NIH lab members Allison Mitchell, Nisha Pawar, Priya Mondal, Ednah Ooko, Chaunte Lewis, Will Frye, and José Gonzalez Dalmasy, thank you for fostering such a warm and supportive environment.

Significant administrative help made this work possible. Many thanks to Bill Churma, Melanie Prange, Rachel Chang, Debbie Chu, and Erica Benkert within the Fischell Department of Bioengineering and Thursa Garcia at NIH for making the administrative side of everything a breeze. Within the Medical Scientist Training Program at the University of Maryland, Baltimore, I thank Mary-Claire Roghmann, Achsah Keegan, Jane Bacon, and Yufan Li for continuous excellent support and for still making me feel connected to the program back in Baltimore while in College Park. I thank George Lieman and Will Rhodes at NIH for their editorial assistance and their patience with my awful grammar. I thank Sijie Hao and Christian Pick in the BioWorkshop for their extreme patience and extensive help with training and troubleshooting on several pieces of equipment. Many thanks to Beth Bauer, Betre Legesse, Cecily Holland, Nakita Charles, Rebecca Leggieri, and the Department of Laboratory Animal Resources for their patience in training, expertise, and care that provided me with the privilege to perform animal studies as a part of this thesis. I thank Wen-An Chiou of the Advanced Imaging and Microscopy Lab for his patience and expertise in acquiring transmission electron microscopy images.

Several individuals outside of the lab directly contributed to this work. Many thanks to Nadia Tsankova, Balagopal Pai, and Thenzing Hurtado for their collaborative efforts in biodistribution studies. I owe huge thanks to BIOE students Stephanie

Krondstadt, Divya Muthusamy, Marzyeh Kheradmand-Hajibashi, and Taya Lee who took time to train me on new techniques and provide materials for studies in this thesis.

I am grateful for my experiences with the Bioengineering Graduate Student Society, and I am particularly thankful for the privilege of serving on the board for two years while in the program. BGSS and the graduate student body enriched my experience and provided immense support throughout the process. I am so grateful to have met such wonderful individuals along the way. I owe a specific thanks to Romanus Hutchins, Lauren Smith, Allison Boboltz, Jeff Yang, Chenchen Handler, and many others on the fourth floor and in the department who provided me with much-needed levity on a regular basis.

On a personal note, many thanks to my parents, John and Jennifer Quinlan, for their support through all my educational endeavors. Growing up with two PhDs in the house taught me how to craft an argument at a very young age – a skill which I believe has served me well.

A final but most significant thank you to Matt Miklosovich. Completing this work was difficult, but dealing with me while I completed this work must have been worse. I will be forever thankful for your endless support and patience in all areas of life – it has made this process a million times more enjoyable, and I am grateful to have you by my side along the way. Thank you for tolerating the late nights, the long weekends, and my insistence on bringing a dog into the house. A closely related thank you to Ollie (formerly Chug the Pug) for helping to keep things in perspective.

Table of Contents*

* Several chapters of this thesis have been adapted and/or reproduced from John Quinlan's previous publications. Permission from publishers was acquired before inclusion in this thesis. Chapter and figures adapted from previous publications are cited in footnotes on chapter title pages and on individual figure pages.

List of Tables

List of Figures

List of Abbreviations

%ID – percent injected dose

5-ALA – 5-aminolevulinic acid

AAALAC – Association for Assessment and Accreditation of Laboratory Animal Care International

ABC – ATP-binding cassette

ABCB1 – ATP Binding Cassette Subfamily B Member 1 (human, gene)

ABCB1 – ATP Binding Cassette Subfamily B Member 1 (human, protein)

Abcb1a - ATP binding cassette subfamily b member 1a (mouse, gene)

Abcb1b - ATP binding cassette subfamily b member 1b (mouse, gene)

abcb4 – ATP binding cassette subfamily b member 4 (zebrafish, gene)

Abcb4 – ATP binding cassette subfamily b member 4 (zebrafish, protein)

ABCG2 – ATP Binding Cassette Subfamily G Member 2 (human, gene)

ABCG2 – ATP Binding Cassette Subfamily G Member 2 (human, protein)

Abcg2 - ATP binding cassette subfamily g member 2 (mouse, gene)

Abcg2a – ATP binding cassette subfamily g member 2 variant a (zebrafish, protein)

abcg2a – ATP binding cassette subfamily g member 2 variant a (zebrafish, gene)

ACN – acetonitrile

ANOVA – analysis of variance

ATCC – American Type Culture Collection

ATP – adenosine triphosphate

au – arbitrary units

AUC – area under the curve

BBB – Blood-brain barrier

BCRP – Breast Cancer Resistance Protein

BD - biodistribution

BEH – ethylene bridged hybrid

BPD-MA – benzoporphyrin derivative monoacid ring A

BTB – blood-tumor barrier

CD – Cluster of Differentiation

CED – convection-enhanced delivery

C_{max} – maximum serum concentration of a drug

DAPI – 4’,6-diamidino-2-phenylindole

DLS – dynamic light scattering

DMEM – Dulbecco’s Modified Eagle Medium

DMPC – 1,2-dimyristoyl-sn-glycero-3-phosphocholine

DMSO – dimethyl sulfoxide

DNA – deoxyribonucleic acid

DOTAP – dioleoyltrimethylammoniumpropane

dpf – days post fertilization

DPPC – dipalmitoylphosphatidylcholine

DSPE-mPEG2000 – distearoylphosphatidylethanolaminemethoxy polyethylene glycol

EGFR – epidermal growth factor receptor

EMEM – Eagle’s Minimum Essential Medium

EtOH – ethanol

EV – empty vector

FBS – fetal bovine serum

FDA – Food and Drug Administration

FGS – Fluorescence-guided surgery

FL – fluorescence

FLIR – forward looking infrared

GBM – glioblastoma

GFAP – glial fibrillary acidic protein

GI_{50} – median growth inhibitory concentration

Gy – Gray

H&E – Hematoxylin and eosin

HEPA – high efficiency particulate air

HPD – hematoporphyrin derivative

HPLC-MS/MS – H-class ultra-performance liquid chromatography-tandem mass spectrometry

i - inhibitor

I.D. – inner diameter

IACUC – Institutional Animal Care and Use Committee

IC_{25} – 25% inhibitory concentration

IC_{50} – median inhibitory concentration

IDH – isocitrate dehydrogenase

IHC - immunohistochemistry

INDYGO – INtraoperative photoDYnamic therapy for GliOblastomas

IP – intraperitoneal

ISMMS – Icahn School of Medicine at Mount Sinai

IV – intravenous

Ko143 - tert-butyl 3-((3R,6S,12aR)-6-isobutyl-9-methoxy-1,4-dioxo-1,2,3,4,6,7,12,12a-octahydropyrazino[1',2':1,6]pyrido[3,4-b]indol-3-yl)propanoate

K_p – brain to plasma ratio

$K_{p,uu,brain}$ – unbound brain to plasma partition coefficient

$K_{p,uu,brain}$ –brain to unbound plasma partition coefficient

LDL – low-density lipoprotein

LITT – Laser interstitial thermal therapy

MeOH – methanol

MGMT – O^6-methylguanine-DNA methyltransferase

MRI – magnetic resonance imaging

MRM – multiple reaction monitoring

MTIC – 5-(3-methyl-1-triazeno)imidazole-4-carboxamide

MTT – (3-(4,5-dimethylthiazol-2-yl)-2,5-diphenyltetrazolium bromide

NaCl – sodium chloride

NanoLuc – NanoLuciferase

NanoVP – Nanosuspension of Verteporfin

NBD palmitic acid – 16-[(7-nitro-2-1,3-benzoxadiazol-4-yl)amino] palmitic acid

NTA – nanoparticle tracking analysis

NUMA1 – nuclear mitotic apparatus protein 1

NVU - neurovascular unit

PBS – phosphate buffered saline

Pdi – polydispersity index

PDP – photodynamic priming

PDT – Photodynamic Therapy

PDX – patient-derived xenograft

PEI – polyethyleneimine

PG – L-α-phosphatidylglycerol

P-gp – P-glycoprotein

PK - pharmacokinetics

pKa – acid dissociation constant

PO – *per os*

PpIX – protoporphyrin IX

RDT – radiodynamic therapy

ROS – reactive oxygen species

RPM – revolutions per minute

RRID – Research Resource Identifier

SD – standard deviation

SDT – sonodynamic therapy

SEM – standard error of the mean

$t_{1/2}$ –half-life

TAZ – transcriptional coactivator with PDZ-binding motif

TBST – tris-buffered tween-20

TEAD – transcriptional enhanced associate domain

TEM – transmission electron microscopy

TERT – telomerase reverse transcriptase

THZ - (E)-N-(3-((5-chloro-4-(1H-indol-3-yl)pyrimidin-2-yl)amino)phenyl)-4-(4-(dimethylamino)but-2-enamido)benzamide

TIC – total ion chromatograph

TQD – tandem quadrupole mass spectrometer

UPLC – ultra-performance liquid chromatography

UV-Vis – ultraviolet-visible spectrum

VP – Verteporfin

YAP – Yes-Associated Protein

ZO-1 – zonula occludens-1

Chapter 1: Introduction

1.1 Thesis Goal

The overarching goal of this thesis is to evaluate synthesis of a nanosuspension of verteporfin (VP) through solvent-antisolvent precipitation, termed NanoVP, and its potential to manage glioblastoma (GBM). *I hypothesize that the properties of NanoVP are tunable by altering the dispersion of VP monomers in antisolvent, and that NanoVP's dissociation in serum will permit its use in GBM, although the nanoformulation alone will not overcome the challenges presented by the disease.* In *Part 1*, I evaluated key parameters in the synthesis of NanoVP, and identified parameters that allowed for modulation of the nanoparticle's diameter, polydispersity (Pdi), concentration, and charge. I then combined traits to scale the diameter and concentration of the resulting nanosuspension. In *Part 2*, I evaluated the pharmacokinetics (PK), biodistribution (BD), and brain penetration of NanoVP, as well as its kinetics in human serum. In *Part 3*, I evaluated the efficacy of NanoVP as a therapeutic agent. This included both *in vitro* and *in vivo* characterization of its effects as a photosensitizer for use in photodynamic therapy (PDT), as well as its potential *in vitro* to perform in a light-independent manner, potentially through modulation of Hippo pathway signaling. I also evaluated the combinatorial potential of the light-dependent and light-independent activity of the drug. Finally, I characterized tool

molecules to support a zebrafish model of the blood-brain barrier (BBB) to further study the ability of NanoVP-based PDT.

The clinical challenge that this thesis aims to address is two-fold. Primary GBM's high mortality rate is attributable to tumor cells that have invaded into healthy brain tissue and must be eradicated. Most patients see recurrence attributable to cells within 2 cm of the tumor border within a year. Primary and recurrent GBM can also occur near eloquent structures, making resection difficult and risky. This thesis aims to understand the ability of therapy with NanoVP, both as a PDT agent and as a chemotherapy, to manage both these recurrent cells as well as inoperable tumors. Additionally, several photosensitizers are available for clinical application. This thesis aims to address the clinical challenge of unresectable tumor cells and identify the most efficacious photosensitizer and formulation for use in GBM.

1.2 Thesis Organization

This thesis contains six chapters.

Chapter 1 begins with the goal and organization of the thesis. This chapter also includes the clinical motivation for my research, as well as relevant background on VP as a therapeutic agent and background on carrier-free nanoparticle synthesis.

Chapter 2 examines the potential to tune the characteristics of a nanoaggregate of VP by hand, develops an automated production system for NanoVP, and identifies appropriate long-term storage options for NanoVP. I also characterize a liposomal formulation of VP made of the same components as Visudyne, which serves as a clinically relevant control in later studies.

Chapter 3 evaluates the pharmacokinetics and biodistribution of NanoVP. PK and BD were evaluated after intravenous (IV) injection of NanoVP in mice bearing flank patient-derived xenograft (PDX) GBM39 tumors. Tissue penetration was further characterized in mice bearing either flank or orthotopic GBM39 tumors after IV or intraperitoneal (IP) injection of NanoVP. VP levels in tissues and serum were quantified by a high-performance liquid chromatography-tandem mass spectrometry (HPLC-MS/MS) protocol that I developed.

Chapter 4 investigates the potential of NanoVP to perform as a PDT agent, in a light-independent manner, and in a combinatorial manner as a single agent against GBM. Cell viability studies post-PDT and post-light-independent incubation were performed with (3-(4,5-dimethylthiazol-2-yl)-2,5-diphenyltetrazolium bromide (MTT) assay and CellTiter Glo. Clonogenic capacity of cells treated with NanoVP-PDT or light-independent NanoVP was evaluated by clonogenic assay. Anti-migratory effects after light-independent incubation were evaluated *via* exclusion zone or gap closure assay. PDT was performed *in vitro* before CellTiter Glo or clonogenic assays, and was performed *in vivo* for the evaluation of survival in mice bearing orthotopic GBM39 tumors.

Chapter 5 works towards using zebrafish as a tool to study PDT-meditated BBB permeabilization. To contribute to a model where NanoLuciferase (NanoLuc) is expressed behind the zebrafish BBB under the glial fibrillary acidic protein (*GFAP*) promoter, I evaluated the Adenosine triphosphate (ATP) Binding Cassette (ABC) transporter substrate status of various novel NanoLuc substrates for human and zebrafish ABC transporters expressed at the BBB. Next, I evaluated the tolerability of

NanoVP for zebrafish in a light-independent manner. As zebrafish are also used for toxicity screening, this study also served as an evaluation of the safety of NanoVP.

Chapter 6 concludes the thesis by highlighting the major discoveries of this thesis and my contributions to the field and discusses future directions for this work.

1.3 Glioblastoma

1.3.1 Pathology and Epidemiology

GBM remains the most common and lethal form of primary brain cancer in adults, accounting for 45-50% of malignant brain tumors [1]. Patients typically present with headaches, seizures, neurocognitive impairment, and focal neurological deficits. Contrast-enhanced magnetic resonance imaging (MRI) is helpful in confirming suspicions, but tumor tissue is required for a definitive diagnosis, which is usually obtained during maximal surgical resection [2]. GBM is characterized by isocitrate dehydrogenase (IDH) mutation status, high cellular density, marked nuclear atypia, high mitotic activity, necrosis, and microvascular proliferation, and frequently displays epidermal growth factor receptor (EGFR) amplification, telomerase reverse transcriptase (TERT) promoter mutation, or concurrent gain of chromosome 7 and loss of chromosome 10 [3]. IDH-wild-type GBM arises *de novo* and has no precursor lesion, while IDH-mutant GBM arises from diffuse or anaplastic astrocytoma and typically has better outcomes [4].

GBM classically invades extensively along white matter tracts and blood vessels, and rarely metastasizes outside of the brain [5]. GBM recurrence is considered inevitable, with progression-free survival of only ~7 months with current treatments

[2]. Around two-thirds of incidences of recurrence occur within 2 cm of the tumor border, indicating that locally invaded cells present a major challenge to the management of GBM [6]. Ultimately, most patients succumb to the disease with 5-year survival rates of only ~6.9% [1].

The incidence rate for GBM is 3.62 per 100,000 individuals, and the incidence rate is highest in individuals ages 75 to 84 years with a median age of 65 years due to steady incidence through all ages and a marked increase in old age. GBM is 1.6 times more common in males than females, with the highest incidence in non-Hispanic White individuals [1]. The only widely accepted modifiable risk factor for glioma is exposure to ionizing radiation [4, 7]. Inherited genetic mutations also are accepted as a cause of glioma or GBM, although familial mutations only account for ~5% of cases [8, 9]. There is some evidence that a history of allergies, eczema, or asthma may be protective against GBM [10, 11]. Recent meta-analyses attempting to identify modifiable risk factors have noted that limited studies about the etiology of GBM have been unable to identify causative or protective factors [12].

1.3.2 Current Clinical Standards for Management

In newly diagnosed patients who can tolerate resection, chemotherapy, and radiation, patients receive maximal surgical resection, with more extensive resection resulting in improvements in overall and progression-free survival [13, 14] in both IDH-wild type and IDH-mutant GBM [15]. Recent Food and Drug Administration (FDA) approval of fluorescence-guided surgery (FGS) with orally administered 5-aminolevulinic acid (5-ALA), which is converted inside tumor cells to photoactive and

fluorescent protoporphyrin IX (PpIX), has aided neurosurgeons in achieving greater extent of resection [16, 17]. Three to six weeks after resection, patients typically receive radiation and concomitant chemotherapy according to the Stupp protocol [18, 19]. This includes 60 Gray (Gy) delivered as 30 2-Gy fractions over 6 weeks. Concomitant with radiation, patients receive daily alkylating chemotherapy with temozolomide dosed at 75 mg/m^2. After a four-week break, patients receive 6 cycles of temozolomide dosed at 150 mg/m^2 for 5 days of a 28 day cycle. Temozolomide is converted inside cells to 5-(3-methyl-1-triazeno)imidazole-4-carboxamide (MTIC), a potent deoxyribonucleic acid (DNA) methylator, particularly of guanine. Nicks in the DNA combined with insufficient DNA repair machinery lead to cell cycle arrest and apoptosis [20]. DNA Epigenetic silencing (promoter methylation) of the O^6-methylguanine-DNA methyltransferase (MGMT) DNA repair gene confers a survival benefit with temozolomide treatment [21] as MGMT reverses alkylation caused by temozolomide [22].

After initial treatment, patients are regularly monitored *via* MRI for recurrence. Upon recurrence, further resection is often recommended, as well as re-irradiation, additional chemotherapy with procarbazine, lomustine, and vincristine, as well as enrollment in clinical trials [23]. Several combination therapies have been explored in recurrent GBM, although none have definitively improved survival. N-nitrosurea alkylating agent lomustine has proven to be most effective, and there is some interest in application of antiangiogenic bevacizumab in combination or as a monotherapy in recurrent disease [24]. Engineered carmustine wafers (Gliadel) placed interstitially in the resection cavity to bypass the BBB and locally deliver chemotherapy have provided

some survival benefits after either primary (13.9 months with Gliadel versus 11.6 months with placebo post-resection [25]) or secondary resection (7.8 months with Gliadel versus 5.7 months with placebo post-resection [26]) [27, 28], although this therapy has not become standard in the clinical management of GBM after over 20 years of clinical experience with the wafers [29].

Patients often experience several complications and frequently receive other therapies for symptom management. Cerebral edema can be treated with dexamethasone or bevacizumab [2]. There are concerns that dexamethasone may worsen outcomes due to decreased tumor cell turnover and therefore reduced susceptibility to chemoradiation; as such, bevacizumab may be preferable for management of edema-related symptoms [30, 31]. Seizures occur in up to 75% of patients [32], and non-hepatically metabolized anti-epileptics such as clobazam, lacosamide, or levetiracetam are frequently prescribed perioperatively or in patients with a history of seizures, but not prophylactically in patients without seizure history [33]. Venous thromboembolism also occurs in up to 30% of patients particularly in the postoperative period [2], and risk of thrombosis outweighs risk of intracranial hemorrhage, so most patients receive anticoagulation therapy [34].

1.3.3 Limitations to Current Treatments

Patients diagnosed with GBM receive maximal surgical resection, radiation therapy, and then systemic or local chemotherapy. Aggressive invasion is a hallmark of all malignant gliomas [5], and invaded GBM cells are deeply intertwined with functional brain tissue [35].

Resection aims to remove the bulk of the tumor but is unable to remove invading tumor cells. These locally invading tumor cells directly cause recurrence, and a greater extent of resection reduces recurrence. When resection with narrow borders is performed, 87.5% of patients had recurrence within 2 cm of the margin of resection. When extended margins (1-2 cm of healthy white matter beyond the tumor by histology) were excised, 67% of patients experienced recurrence within 2 cm of the margin of resection [36]. While the decrease in local recurrence was statistically significant, extensive resection is not feasible near eloquent structures. Furthermore, two in three patients still experienced local recurrence.

Patients receive radiation therapy and chemotherapy. Radiotherapy relies on exogenous high-energy photons and local oxygen to damage DNA and induce cell death in cancer cells and has been shown to provide a modest survival benefit as a monotherapy in patients that cannot undergo surgery [37]. In the context of GBM, local hypoxia, radioresistant stem-like cancer cells, and upregulated DNA damage response mechanisms limit the efficacy of radiotherapy [38].

Chemotherapy is also an important part of GBM management. Temozolomide, a DNA alkylating agent, is the first-line chemotherapy in GBM [39]. It is a substrate of both ATP Binding Cassette Subfamily B Member 1 (ABCB1) and ATP Binding Cassette Subfamily G Member 2 (ABCG2), two drug efflux transporters located at the BBB, but it is still bioavailable enough for use in GBM [40]. It is estimated that the temozolomide concentration in the brain interstitium is 17.8 ± 13.3% of serum levels [41]. The mechanism of resistance of temozolomide is well-known. Unmethylated MGMT reverses the alkylation caused by temozolomide, meaning that temozolomide

is essentially ineffective in the 45-55% of patients with unmethylated MGMT [42]. Temozolomide treatment ultimately fails to control disease, as an unplanned retrospective meta-analysis found no survival benefit for continuing the drug past six cycles of temozolomide treatment [43]. Development of other drug options for the management of residual disease has been largely unsuccessful due to the presence of an intact BBB protecting unresectable cells from cytotoxic agents [44].

Even after standard of care therapy with resection and radiochemotherapy, local recurrence occurs in 79.3% of patients [45]. As such, the next generation of GBM therapies should complement current approaches and work to eradicate the population of cells that drives recurrence.

1.3.4 Physical Modalities to Manage Recurrent Disease

The primary challenge to modern GBM treatment is eradication of locally invading cells in healthy brain matter. A number of intraoperative or local treatment modalities are under investigation to manage residual GBM cells and to prevent or manage recurrence [46]. Physical approaches to eradicate residual cells include thermal heating and PDT.

The goal of thermal heating is to reach a temperature of 43°C for 90% of the tumor volume for 10 minutes to cause cell death [47] or to 40-44°C to slow tumor growth [48]. This can be accomplished in a few different ways:

(1) Laser interstitial thermal therapy (LITT) utilizes a burr hole to provide access for a laser fiber to reach deep-seated tumors or tumors next to eloquent tissue [49]. Light energy from the laser is absorbed by

chromophores in the tissue, including hemoglobin and water [50]. LITT has provided outcomes similar to resection for patients with recurrent GBM, with the added benefit of shortened hospital stays compared to resection [51]. The efficacy of LITT has been enhanced through the addition of nanoparticles [52] to improve the specificity and efficacy of the therapy. LITT is currently under clinical investigation for GBM management (NCT04699773, NCT05663125, NCT04181684, NCT05318612) and BBB permeabilization (NCT02372409).

(2) Focused ultrasound uses high-intensity acoustic waves to generate thermal effects by generation of acoustic cavitation [53]. Focused ultrasound has been used for thermal ablation of brain tissues in other diseases, but not tumor ablation, and has been used for peritumoral BBB permeabilization [54].

(3) Radiowaves creating an alternating magnetic field have been used to heat stereotactically placed iron magnetic beads, and results have been promising in a few trials [55].

The challenge with thermal-based therapies is that they generally perform best with existing tumors, and their application to the surgical bed post-resection has not been explored, likely due to concerns about damage to healthy tissue with heat application. Heat-based therapies offer options once recurrence takes place, but are not optimal to prevent recurrence.

Local radiotherapy, where emitting materials are placed stereotactically at a site of recurrence or post-surgically in the resection cavity, is an emerging option to manage recurrence. Stereotactically placed radiotherapy was found to be safe and feasible in a salvage situation with low-dose iodine-125 [56, 57]. With radiation during surgery, where 10-40 Gy of 50 kV X-rays were applied to the surgical margin, local recurrence was reduced to 35.3% when combined with standard radiotherapy and chemotherapy [58], an improvement over standard therapies alone. A 15-patient prospective study for intraoperative radiotherapy in newly diagnosed GBM, where patients received 20-30 Gy at the surgical border post-resection, observed radionecrosis in 33% of patients, and grade 3 adverse events in 33% of patients [59]. While these toxicities are manageable, local radiotherapy may ultimately be limited by the high rate of complications and treatment failures [60].

PDT relies on systemically delivered photosensitizers accumulated within tumor tissues that are then activated by light of a specific wavelength to produce reactive oxygen species (ROS) and induce biological changes. To date, the focus has been PDT utilizing 5-ALA-induced PpIX. 5-ALA was approved for FGS in GBM [17] where 405 nm (blue) light is used to activate pink fluorescence in tumor tissues, which preferentially accumulate PpIX due to a number of metabolic aberrancies in cancer cells [16]. Application of higher-energy light at a wavelength of 635 nm, a Q-band for PpIX, results in greater ROS generation [61]. Perioperative 5-ALA-induced PpIX PDT is feasible, but so far has still resulted in a 75% local recurrence rate [62], which is comparable to standard recurrence patterns. Another study that utilized FGS during resection followed by PDT with Photofrin and radiation compared to resection and

radiation alone found an improvement in overall survival of 6.6 months in the experimental group [63], although the study has been criticized because there was no FGS control, and greater extent of resection may have been responsible for the survival benefit. Others found that FGS with 5-ALA PDT was superior to FGS alone [64], indicating a potential role for 5-ALA-mediated PDT. There are a number of ongoing efforts to explore the potential of 5-ALA-induced PpIX PDT in the clinic [65] (**Table 1-1**).

Table 1-1. Parameters in clinical applications of 5-ALA photodynamic therapy. A summary of currently ongoing 5-ALA PDT clinical trials and reports from clinical trials.*

Clinical Trial Code or Citation	5-ALA dose, mg/kg	Drug-light interval	Light Parameters	Notes
NCT04391062	-	4-6h	400, 600, 800 J/cm^2	Phase II; Light dose escalation; patients receive maximal safe and intracavitary PDT followed by Stupp protocol radiochemotherapy
NCT04469699	20	3.5-4.5h	-	Phase II; Stereotactic photodynamic therapy for recurrent GBM with best possible radiochemotherapy at investigator's discretion
NCT03897491	20	3.5-4.5h	-	Phase II; Safety and efficacy of stereotactic interstitial PDT
Quach *et al* [66]	20	3h	mean 12240 J total dose; 1h irradiation; 200 mW/cm	Interstitial PDT on inoperable tumors
Vermandel *et al* [65]	20	6h	200 J/cm^2; mean 1772 J total dose; 10 min irradiation	Post-resection PDT in surgical field

* This table was first published in Quinlan JA, Baumiller K, Gaur A, Chiow W-A, Robey RW, Gottesman MM, and Huang H-C, "Self-Assembled Verteporfin Nanoparticles for Photodynamic and Light-Independent Therapy in Glioblastoma." *Adv NanoBiomed Res.* 2024;2400098. doi: 10.1002/anbr.202400098.

1.3.5 Methods to Overcome the Blood-Brain Barrier to Manage or Prevent Local Disease

The BBB is a major challenge to effective treatment of GBM, especially in cases of invasion where the BBB may still be intact [67]. While temozolomide is delivered orally for systemic delivery to the tumor and crosses the BBB due to its small size [20], several other approaches are under investigation for improving delivery to the tumor.

Convection-enhanced delivery (CED) creates a fluid pressure gradient to infuse materials deeper into the brain [68]. This has been attempted using liposomal irinotecan as Onyvide (NCT02022644, NCT03086616) and topotecan [69, 70] most notably. Challenges with CED are largely technical and have to do with the clinical implementation of the therapy. A cannula must be placed by a trained surgeon, and proper placement of the cannula is challenging even for experienced neurosurgeons [71]. Additionally, CED has primarily been applied to existing tumors, not residual disease before recurrence takes place.

Implanted or injected biomaterials have also been of interest for improving outcomes post-resection. The most well-known example is Gliadel wafers, which are carmustine-loaded biodegradable wafers inserted in the cavity created by resection [25]. Gliadel aims to deliver the alkylating chemotherapy directly to residual cells, but its use is controversial due to limited survival extension (2 months) and high complication rates (~47%) [72]. With Gliadel placement, extent of resection was still more important to survival than wafer insertion, and the insertion of more wafers increased complication rates [73].

Local intraarterial and intratumoral delivery has also been attempted. Intra-arterial delivery almost always requires a BBB disrupting agent like mannitol, and many attempts have been made with carboplatin, nimustine, bevacizumab, cetuximab, and temozolomide [74]. Intraarterial delivery is ultimately challenged by several factors. The PK/BD of locally infused materials is poorly understood, there are few drugs that are both locally and systemically tolerated when infused directly into the blood, and a process known as "streaming," where the agent is diluted in the blood so much that it doesn't enter the tissue to a greater degree, is a concern. Finally, the technique still relies on local BBB permeabilizers, and has other clinical issues such as catheter placement, local site reactions, and challenging vascular access [75]. Intratumoral nimustine, another alkylating agent, combined with local BBB permeabilization had low improvements in survival when combined with temozolomide and radiation therapy [76].

Intraventricular and intrathecal delivery of nitrosoureas and methotrexate have had issues with infection, catheter obstruction, and inadequate drug distribution, and there is little bulk flow in this area, which limits local movement of the drug [77].

1.3.6 Models for Studying Drug Delivery to the Brain

The BBB and its supporting neurovascular unit (NVU) [78] (composed of endothelial cells, astrocytes, neurons, pericytes, microglia, and the basement membrane [79]) protect the brain by regulating the delivery and clearance of circulating molecules [80]. While this protects the brain from toxins, it also limits drug penetration. The passive barrier of the BBB consists of both the basement membrane and specialized

endothelial cells that express tight junction transmembrane complexes to block paracellular diffusion of many molecules [81, 82]. The active barrier of the BBB endothelial cells consists of ATP-binding cassette (ABC) transporters, which efflux toxins and therapeutics against their concentration gradient back into the bloodstream [83]. Two of the highly expressed ABC transporters at the human BBB are ABCB1 (also known as P-glycoprotein or P-gp) and ABCG2 (also known as Breast Cancer Resistance Protein or BCRP). The surrounding astrocytes, neurons, pericytes, and microglia adjacent to the endothelial cells are important to their barrier function [84]. Overcoming the BBB is a major challenge for the management of brain malignancies [85] as many therapeutics cannot successfully enter the brain due to diffusion limitations or because they are transported by one or both ABC transporters [86].

Despite evidence that ABC transporters remain a significant challenge to the management of BBB-protected malignancies, no therapies have been approved to increase the penetration of chemotherapy drugs into the brain. This may be due to challenges in modeling the BBB. Typical *in vitro* models of the BBB are often incomplete, lacking components of the NVU, while murine and large *in vivo* models are expensive to maintain and are not amenable to high-throughput screening [87]. Thus, improved model systems to identify strategies to increase drug delivery to the brain are needed.

Mouse models remain the gold standard for modeling BBB penetration due to the complexity of the BBB and the similarity of the mouse BBB to the human BBB [88]. The zebrafish (*Danio rerio*) has surprising homology to the human NVU and BBB, and may be a cheaper and more efficient model for studying transport at the BBB

[89, 90]. Endothelial cells that make up the zebrafish BBB form tight junction complexes *via* claudin-5 and zonula occludens-1 (ZO-1), providing a passive barrier like the mammalian BBB [91]. Zebrafish also have a comparable active barrier. Zebrafish ATP binding cassette subfamily b member 4 (Abcb4) and ATP binding cassette subfamily g member 2a (Abcg2a) function similarly to human ABCB1 and ABCG2, respectively, in terms of substrate and inhibitor profile. Both Abcb4 and Abcg2a are present at the zebrafish BBB [92-95]. In addition to homologous ABC transporters and tight junctions, zebrafish also have an analogous NVU to humans, with pericytes and radial glial processes that may function similarly to human astrocytic end feet [96]. These similarities, combined with the potential for high-throughput screening in zebrafish, make the organism a tempting model for studying the BBB.

1.4 Verteporfin as a Therapeutic Agent

1.4.1 Mechanisms of Photodynamic Therapy

PDT relies on photochemistry to induce biological changes, avoiding temperature or mechanical damage along the way. photosensitizers are delivered systemically and activated at the site of interest using light of a specific wavelength. Light energy is absorbed by the photosensitizer. The photosensitizer is excited from its ground singlet state (S_0) to its excited singlet state (S_1). Intersystem crossing causes S_1 to give rise to an excited triplet state, T_1, which is magnetically different from S_1. T_1 can then initiate photochemistry directly (a type I reaction, free radical production, resulting in superoxide production (O_2^-)) or indirectly (a type II reaction, transferring

its energy to ground state oxygen, $^3O_2$, leading the production of singlet oxygen ($^1O_2$)) [97].

All photochemistry relies on the presence of oxygen, light, and photosensitizers. The amount of light and photosensitizer, however, can impact the biological effects of PDT. At higher doses of photosensitizer and light (>1 μM × J/cm^2), the photosensitizer VP generates ROS (e.g. $^1O_2$, •OH) and induces mitochondrial depolarization [98], leading to apoptosis and cell death [98]. At lower light doses, typically <1 μM × J/cm^2, activated photosensitizer generates ROS, but at much lower concentrations. This modulates nearby tissues without inducing cell death, termed photodynamic priming (PDP).

PDT with VP has been performed using liposomal VP as Visudyne in age-related wet macular degeneration. In this original treatment scheme, VP was infused over 10 minutes at a dose of 6 mg/m^2, and, 15 minutes later, light (690 nm, 600 mW/cm^2, 50 J/cm^2, approx. 83 seconds of irradiation) was delivered through the eye [97]. VP-PDT has also been applied to locally advanced pancreatic cancer. In a phase I/II study, 0.4 mg/kg VP was infused 60-90 minutes before light irradiation (interstitial fiber, 690 nm, 5 J-240 J, 150 mW for 33 seconds per 5 J dose), and 12 mm ablation zones were observed in patients receiving 40 J without limiting toxicity [99]. A similar study using Visudyne at similar doses (0.4 mg/kg VP; interstitial fiber delivered *via* endoscopic ultrasound, 690 nm light, 50 J/cm, 150 mW for 333 seconds) found similar ablation zones but reported that 3 of 8 enrolled patients were nonresponders [100].

1.4.2. Photodynamic Therapy in the Context of Glioblastoma

The use of photosensitizers to manage GBM first made headway *via* the 2017 FDA approval of 5-ALA for FGS during resection [17]. 5-ALA accumulates in tumor cells as PpIX, permitting visualization under blue light [61]. After the approval of FGS, 5-ALA PDT has been explored. The INtraoperative photoDYnamic Therapy for GliOblastomas (INDYGO) clinical trial demonstrated that PDT performed with systemically delivered drug and light administered within the surgical resection cavity only adds 35 minutes surgery [65]. In this trial, patients received FGS followed by 5-ALA induced PpIX PDT. Other approaches, such as stereotactic PDT where a light diffusing fiber is inserted into the brain, are under investigation for smaller recurrences that may not warrant full resection or that may be in inoperable locations [66] [NCT03897491]. While the INDYGO trial demonstrated feasibility, improvements in survival remain to be seen [65] and light dose escalation studies are currently under way to find an efficacious but safe dose [NCT04391062, NCT05736406].

There are several limitations that may explain the limited efficacy of 5-ALA PDT to date. It has been noted that accumulation of PpIX can vary between cells based on their molecular drivers [101], and that differential expression of several enzymes in the heme synthesis pathway results in loss of sensitivity to 5-ALA PDT [102]. Whereas the only FDA-approved PDT treatment relies on vascular shutdown [97], PpIX accumulation is expected in cells with dysfunctional heme synthesis pathways, meaning that 5-ALA PDT should have no activity in the vasculature or in any other cell types. While 5-ALA PDT has proven safe for FGS, its specificity, which is a mechanism by which toxicity is avoided, may also be its downfall as a PDT agent. As

such, consideration of other PDT agents may yield more promising results. What's more, 5-ALA is thought not to be BBB penetrant [103], meaning that accumulation of PpIX is likely poor in invading cells behind an intact BBB.

VP is delivered as an active photosensitizer, meaning that it will be active both in vasculature and in target cells. Our lab has previously shown that VP can be activated up to 2 cm into the rodent brain while PpIX is limited to <1 cm [104], consistent with observations from others [105-108]. In all, the potentially limited accumulation of PpIX and greater depth of activation for VP indicates that VP may be a favorable tool for PDT in GBM. Our lab has previously demonstrated that PDP with VP can increase intratumor accumulation of liposomal irinotecan, ONIVYDE, by up to 11-fold in pancreatic cancer due to vessel permeabilization [109]. We found that, mechanistically, VP-PDP alters the phenotype of continuous tight junctions in brain endothelial cells, permitting enhanced model drug flux through a monolayer [110]. In the brain, this results in BBB permeabilization permitting accumulation of model drugs [111]. We have also demonstrated that VP is a substrate for both ABGC2 and P-gp, and, when light-activated, can photooxidize amino acid residues and induce crosslinking, resulting in nonfunctional transporters [112, 113].

In all, VP may be a more suitable photosensitizer for use in GBM because it is active in the vasculature and can be activated at a greater depth from the light source. The ability to activate VP up to 2 cm is beneficial both because of the location of residual cells and the potential side effects of PDT. Either direct cell killing or BBB permeabilization in the 2 cm zone where most cells that cause recurrence lie is beneficial, but cell killing and BBB permeabilization in the healthy brain is undesirable.

Disruption of the BBB in otherwise healthy tissue can lead to ion dysregulation, edema, neuroinflammation, increased intracranial pressure, neuronal dysfunction, and neuronal degradation [114]. In the context of PDT post-resection or interstitial PDT of an unresectable tumor, the ability of light to penetrate to depths in which cells of concern exist but not deeper is favorable for patient safety. PDT with VP offers direct cell killing, vascular shutdown [115], vascular permeabilization, and inhibition of ABC transporter activity to a self-limited depth. As such, the application of VP in GBM for PDT may improve outcomes over 5-ALA PDT.

The use of photosensitizers in GBM management includes PDT, FGS, Yes-associated protein (YAP) sequestration, radiodynamic therapy (RDT), and sonodynamic therapy (SDT). Ongoing clinical trials using photosensitizers in these contexts are outlined in **Table 1-2**. RDT relies on an observed combinatorial effect of photosensitizer administration and concomitant ionizing wave administration, although a specific mechanism of action is unclear [116]. SDT relies on ultrasound to activate photosensitizers, although there is not yet a consensus on its mechanism of action [117].

Table 1-2. Current clinical trials using photosensitizers in glioblastoma. Trials are primarily focused on the application of 5-ALA as a PDT, RDT, SDT, or FGS agent. VP is used as a chemotherapy in one trial, and various other photosensitizers or dyes are used in various studies.

Clinical Trial	**Phase**	**Agent**	**Therapy**
NCT04590664	I/II	Visudyne	Chemotherapy
NCT05929456	I	Cetuximab-IRDye800CW	FGS
NCT04780009	Observational	5-ALA	FGS
NCT05363826	I	Photobac	PDT
NCT03897491	II	PL L 506	PDT
NCT04469699	II	5-ALA	PDT
NCT05736406	I/II	5-ALA	PDT
NCT04391062	II	5-ALA	PDT
NCT05590689	I/II	5-ALA	RDT
NCT04845919	II	5-ALA	SDT
NCT05362409	I	5-ALA	SDT
NCT06039709	I	5-ALA	SDT

1.4.3 Verteporfin as a Hippo Pathway Modulator

An ongoing clinical trial (NCT04590664) is evaluating the ability of Visudyne infused weekly to limit the progression of GBM in patients with recurrent disease. VP was identified in 2012 as a binder of the transcriptional coactivator YAP [118], blocking the ability of YAP to interact with transcriptional enhanced associate domain (TEAD) transcription factors, ultimately inhibiting Hippo pathway-mediated transcription [118]. In cancers, YAP/transcriptional coactivator with PDZ-binding motif (TAZ) signaling can drive a stem-like phenotype [119]. This property of VP has recently been leveraged in a number of preclinical studies in GBM [120-124], retinoblastoma [125], conjunctival melanoma [126], ovarian cancer [127], esophageal cancer [128], and pancreatic ductal adenocarcinoma [129].

It is worth noting that the screen that identified VP as a modulator of Hippo pathway signaling also identified PpIX and hematoporphyrin derivative (HPD) as a modulator of Hippo pathway signaling [118]. The authors did not pursue PpIX or HPD as candidates due to their lower binding affinity for YAP than VP. Combined with concerns about limitations to the efficacy of 5-ALA-induced PpIX in GBM, it may be worth considering VP alone for both PDT and light-independent YAP sequestration over 5-ALA.

1.4.4 Delivery Routes for Verteporfin and Suitability for Glioblastoma

Due to its hydrophobic nature, VP has been delivered in the clinic as Visudyne, which requires lipid carriers to solubilize the drug and permit intravenous infusion. Visudyne is a largely polydisperse population of particles (200-2000 nm) with a high

Pdi (>0.7) [130]. Several studies have shown that, compared to VP delivered in organic solvent, liposomal delivery of VP decreases intracellular accumulation within cancer cells by 1-2 orders of magnitude [131-133], which is a common challenge for drugs delivered with lipid carriers [134, 135]. Liposomes can also be recognized by both the innate and adaptive immune systems, leading to hastened clearance and accumulation in the mononuclear phagocyte system [136]. While this was likely not a major concern in the original application of Visudyne, where the drug was infused once and PDT was performed after 15 minutes, this may be less desirable for new applications of VP where VP is infused in larger quantities, regularly, over weeks to months.

Finally, in the context of GBM, penetration into the brain is an important factor for therapeutic efficacy. As a nanoparticle, the diameter of Visudyne particles may significantly impact their movement through the brain. Studies have found that ~75% of pores in fresh human brain are less than 125 nm [137]. Functional studies have identified an upper limit of 64 nm for free diffusion of particles between cells in the brain [138]. As such, for effective delivery to the brain, particles less than 64 nm in diameter are desirable, which is not feasible with Visudyne. Drugs that cross the BBB generally have a molecular weight less than 500 Da, are lipophilic, but not so much so that they cannot exit the endothelial cells making up the BBB, and are not actively effluxed from the brain stroma to the blood [139]. Monomeric VP has a molecular weight of 718.8 Da, is lipophilic, and is a substrate of ABC transporters at the BBB [113, 132, 139]. Intravenously delivered VP in Visudyne has been measured in resected tumor from human patients [121] and animal studies indicate that VP may access the brain when delivered systemically [120]; however, the ability of VP to cross the BBB

is still poorly understood. Careful evaluation of brain accumulation, particularly in regions with an intact BBB, must be undertaken, and strategies to improve delivery to the brain will remain desirable.

1.5 Carrier-Free Drug Formulations

1.5.1 Synthesis Methods

Broadly, pure-drug nanosuspensions are formulated either by "top-down" techniques, where large particles are broken down into smaller particles, or "bottom up" techniques, where the nanosuspension is formulated from a molecular dispersion, frequently through wet or dry milling, high pressure homogenization, and co-grinding [140]. These processes are good for industrial production, where a large amount of material is available for synthesis. Several of these techniques also cause significant heat generation, so either thermally stable molecules or cooling systems are needed to protect the therapeutic agent.

Bottom-up processes are generally thought to be simpler, require less energy, and require simpler tools than top-down processes, and can result in more monodisperse and smaller populations of particles [141]. Bottom-up processes include ultrasonication, liquid emulsion, and solvent-antisolvent precipitation [140].

Not all nanosuspensions are truly carrier-free. After formulation, many nanosuspensions require stabilization to avoid aggregation, sedimentation, transformation to crystalline structures during storage, or to avoid dissolution in plasma or chemical instability upon administration [142]. Common stabilizers include poloxamers, modified amino acids, cellulose-based additives, polyethylene glycol,

surfactants like tweens, sodium dodecyl sulfate, or Cremophor, and, in some cases, residual organic solvents have all been used to stabilize nanosuspensions [140, 142]. Lyophilization and spray drying are often used post-production to improve stability [143].

While several nanosuspensions are used clinically, efforts to finely tune the properties of nanosuspensions have been limited. Work has been done to evaluate how synthesis parameters impact the diameter of paclitaxel nanoaggregates, finding that the concentration of paclitaxel in solvent and increased solvent:antisolvent ratios resulted in increased diameters [144]. Beyond this, because many synthesis schemes are proprietary, minimal information is available on how particle properties can be managed.

1.5.2 Clinical Utility of Nanosuspensions

Nanosuspensions permit the delivery of hydrophobic molecules in aqueous solutions without the need for excipients or carrier molecules. The utility of nanosuspensions comes from the inability to use organic solvents clinically in large volumes. One of the most commonly used organic solvents, dimethyl sulfoxide (DMSO), is a polar solvent miscible with water and is capable of dissolving a number of polar and nonpolar small molecules [145]. Long-term (up to 2.5 years) DMSO therapy in humans has been well-tolerated, and the solvent has shown a number of favorable pharmacological properties including membrane penetration, anti-inflammation, enhanced activity of concomitantly administered drugs, and nonspecific enhancement of immunity, among other properties [146]. The most common adverse

events reported after therapy including DMSO included gastrointestinal and skin reactions, and most adverse reactions were transient and did not require intervention [147]. DMSO has been FDA-approved for the management of interstitial cystitis/bladder pain syndrome *via* intravesicular delivery since 1978, although its mechanism of action in managing pain in this disease is poorly understood [148]. DMSO, ultimately, is not inert and does modify cellular processes [149]. Ultimately, DMSO may have some potential as a carrier at low percentages, but its utility and its off-target effects are understudied at this time.

Pure drug nanosuspensions can be made up of particles with either a crystalline character (referred to as nanocrystals) or with amorphous character (referred to as nanoaggregates). Nanocrystals may form because of material properties or due to higher energy input to form a lattice, generally forming a more stable structure than nanoaggregates, which require less energy to form and can generally have greater solubility as a result [150]. Nanocrystals have high stability post-injection due to the minimized Gibbs free energy [151]. This means that larger nanocrystals are less soluble than smaller ones due to reduced relative surface area, and they take more time to disassociate. Nanocrystals have been leveraged for extended-release of antiretroviral therapies [152-154], anticancer drugs [155, 156], and other medications [157]. However, in the context of PDT, the potential for prolonged photosensitizer bioavailability from nanocrystals could potentially be unfavorable in terms of skin phototoxicity. In contrast, amorphous nanodrugs generally possess a higher saturation solubility and, consequently, an increased dissolution velocity (creation of high maximal serum concentration (C_{max}), reduction of half-life ($t_{1/2}$)) compared to equally

sized nanocrystals [158]. In other words, larger nanoaggregates will dissolve in solution faster, and will dissociate faster than comparable nanocrystals.

Carrier-free nanosuspensions help overcome drug solubility and bioavailability issues, and the simplicity of the system improves potential to translate the product to market, removes potential toxic side effects of excipients, and permits around 100% drug loading within particles [159]. A number of commonly used drugs are nanosuspensions, including paclitaxel as Abraxane for chemotherapy, methyl phenidate hydrochloride as Ritalin for attention deficit hyperactivity disorder and narcolepsy, nabilone as Cesament, aprepiant as Emend for nausea, and fenofibrate as Tricor or Triglide for hypercholesterolemia, among others [140].

The best-studied nanodrug for anticancer effects is paclitaxel, a widely used chemotherapeutic drug, which stabilizes microtubules to induce defects in mitotic spindle assembly, chromosome segregation, and cell division. Pure-drug nanosuspensions of paclitaxel, as well as carrier-free co-delivery of paclitaxel with other chemotherapies, photothermal agents, and photodynamic agents have been developed [160]. The most successful application of paclitaxel nanoaggregates is with albumin as Abraxane, which showed improved tumor response and decreased neutropenia compared to Taxol, which is paclitaxel delivered with the emulsifier Cremophor EL [161]. Improved efficacy and reduced side effects were observed likely because tumoral accumulation was similar between the two agents despite 5-fold lower plasma levels with Abraxane [162]. This is likely attributable to improved paclitaxel distribution and tissue penetration when delivered as Abraxane compared to solvent-

based paclitaxel [163]. As a result, Abraxane is used in combination therapies for advanced breast cancer, non-small cell lung cancer, and pancreatic cancer [164].

In all, nanosuspensions present a promising and clinically relevant way to deliver hydrophobic drugs.

Chapter 2: Synthesis of NanoVP, a Nanosuspension of Verteporfin*

2.1 Introduction

We recently described a new formulation of VP, termed NanoVP, which capitalizes on the self-aggregation of VP in aqueous solution to form carrier-free nanoaggregates [111]. Self-aggregation of VP in water has been noted for decades [165] and has been observed in cells with high concentrations of the drug [166]. Aggregates of various porphyrins have been detected and were historically described as "micelle-like" aggregates [167], but because VP was initially developed as a photosensitizer, concerns about reduced photoactivity in aqueous aggregated forms [168] led to clinical application of the drug in lipids as Visudyne. Visudyne has been reported to have large and variable diameters (733.8 ± 488.9 nm) and a high Pdi (0.66 ± 0.20) [130]. It is thought that a particle diameter <150 nm is needed to extravasate from leaky vasculature at the site of a tumor, and a diameter <50 nm helps evade mononuclear phagocyte system-mediated clearance or to permit adequate delivery to the brain [169]. While Visudyne's broad size is desirable for keeping VP in vasculature

* This chapter was adapted from Quinlan JA*, Inglut CT*, Srivastava P, Rahman I, Stabile J, Gaitan B, Arnau del Valle C, Baumiller K, Gaur A, Chiou W-A, Karim B, Connoly N, Robey RW, Woodworth GF, Gottesman MM, and Haung H-C, "Carrier-Free, Amorphous Verteporfin Nanodrug for Enhanced Photodynamic Cancer Therapy and Brain Drug Delivery." *Adv Sci (Weinh).* 2024;11(17):e2302872. doi:10.1002/advs.202302872 and Quinlan JA, Baumiller K, Gaur A, Chiow W-A, Robey RW, Gottesman MM, and Huang H-C, "Self-Assembled Verteporfin Nanoparticles for Photodynamic and Light-Independent Therapy in Glioblastoma." *Adv NanoBiomed Res.* 2024;2400098. doi: 10.1002/anbr.202400098. Permission was obtained from the publisher to use this material in the current dissertation.

for light-mediated vascular shutdown [97], new formulations that improve delivery to tumors may be useful. Originally, liposomal VP was adopted as the delivery route for VP because it outperformed VP delivered in DMSO in early biodistribution and efficacy studies [170, 171]. It was noted in these studies, however, that delivery of VP in DMSO resulted in some aggregation and was not translationally relevant [171]. It is now thought that VP almost immediately dissociates from lipids in Visudyne to redistribute to biomolecules in the plasma [172]. Considering practical limitations with acquiring Visudyne [173], a new focus on VP as an anti-cancer drug in the absence of light, and historic motivations for utilizing lipids to deliver VP, we believe NanoVP may have clinical utility. Here, we have carefully evaluated key parameters in its synthesis and stability, and further evaluated its antitumor efficacy in GBM.

Our initial formulation of NanoVP was limited to a theoretical maximum concentration of 140 μM [111], which limited application of the nanosuspension for *in vivo* use. With the goal of increasing concentration, we noticed that the diameters of particles changed. I studied how altering parameters in the solvent-antisolvent synthesis process impacted the diameter of NanoVP. My data provide insights into methods to alter the parameters of amorphous nanoparticles produced by this synthesis method, increase the concentration of the resulting nanosuspension, and provide details on appropriate long-term storage of the end product.

2.2 Methods

2.2.1 Chemicals

VP (also known as benzoporphyrin derivative monoacid ring A (BPD-MA)) was acquired from US Pharmacopeia (Rockville, MD, USA). UltraPure distilled water was acquired from Invitrogen (Life Technologies, Grand Island, NY, USA). DMSO was acquired from Fisher Chemical (Waltham, MA, USA). Acetone was acquired from Fisher Chemical (Waltham, MA, USA). Ethanol (EtOH) was acquired from Pharmco (Brookfield, CT, USA). HPLC-grade Methanol (MeOH) was acquired from Alfa Aesar (Ward Hill, MA). Calcbiochem OmniPur 10X phosphate buffered saline (PBS) concentrate was acquired from Millipore (Burlington, MA, USA) and diluted to 1X in deionized water. Instant Ocean was acquired from Spectrum Brands (Blacksburg, VA, USA) and dissolved in water at a working concentration in deionized water. Acetonitrile (ACN), dextrose, sodium chloride (NaCl) solution (5 M, diluted to 0.9 w/v% in deionized water), HPLC-grade water, crystal violet, chloroform, and 10% formalin were acquired from Sigma-Aldrich (St. Louis, MO, USA).

2.2.2 NanoVP Formulation

VP dissolved in DMSO was added dropwise with a 10 µL pipette to UltraPure water stirred with a 10 mm x 3 mm stir bar (Fisher Scientific, Waltham, MA, USA) on a Cimarec+ Stirring Hotplate (7.25” x 7.25” or 10.25” x 10.25”) (Thermo Scientific, Waltham, MA, USA) over a five-minute period. After all VP in DMSO was added, the nanosuspension was allowed to mix until homogenous (approximately 3 minutes), then transferred to Spectra/Por 300 kD Cellulose Ester Float-A-Lyzer G2 dialysis device or

Spectra/Por 300 kD Biotech Cellulose Ester Tubing (Repligen, Waltham, MA, USA) and dialyzed against PBS for 24 hours at 4°C. VP concentration was determined based on UV-Vis absorbance in DMSO (Synergy Neo2, BioTek Instruments, Winooski, Vermont, USA) using the established molar extinction coefficient (VP: ε=80,500 $M^{-1}cm^{-1}$ at 435 nm, ε=34,895 $M^{-1}cm^{-1}$ at 687 nm).

2.2.3 Dynamic Light Scattering

Hydrodynamic diameter, Pdi, and Zeta potential were measured using a particle sizer and Zeta potential analyzer (NanoBrook Omni, Brookhaven Instruments, Holtsville, NY, USA). For hydrodynamic diameter and Pdi, 20 µL NanoVP was mixed with 2000 µL UltraPure water. In the case of very low concentrations of sample (e.g., 1% solvent:antisolvent ratio; 1 mM VP in DMSO; acetonitrile, ethanol, and methanol samples after filtration) the full volume used was sample. For Zeta potential, 20 µL sample was mixed with 1600 µL 10 mM sodium chloride.

2.2.4 Transmission Electron Microscopy

NanoVP samples were either made fresh and dialyzed against deionized water before transmission electron microscopy (TEM) or dialyzed from PBS against deionized water to remove salts from the sample. The size, morphology, and microstructure of NanoVP were studied using a transmission electron microscope (JEOL JEM-2100 LaB6, 200 kV; Peabody, MA, USA). For conventional TEM, NanoVP (10 µL) was pipetted onto a Lacey carbon grid (Ted Pella, Redding, CA, USA) and air dried overnight before the examination. Images were taken at high magnifications (10,000-100,000x). Due to small particle sizes and to enhance

diffraction intensity, selected area electron diffraction was used to collect electron diffraction patterns.

2.2.5 Nanoparticle Tracking Analysis

NanoSight nanoparticle tracking analysis (NTA) was used to quantify nanoparticle concentration and calculate VP molecules per construct. Particles were diluted in water (NanoVP, 1:200; liposomal VP, 1:100,000) to a total volume of 500 µL, then loaded onto the NanoSight LM10 (Malvern Instruments; Malvern, UK). NTA analytical software version 3.4 was used to analyze three 30 second videos of each sample, with the sample advanced through the imaging chamber between each capture. The detection threshold was set to two for all measurements. From the output of particles/mL, VP molecules per construct were calculated based on VP concentrations measured by absorbance.

2.2.6 Automated Pump System

An NE-1600 Syringe Pump (New Era Pump Systems, Inc., Farmingdale, NY, USA) was affixed to a 3 mL BD Plastipak Luer-Lok syringe (Becton, Dickinson and Company, Franklin Lakes, NJ, USA). The syringe was affixed to a female luer lock with 1/8” inner diameter (I.D.) polypropylene barb adapter (Avantor Masterflex, VWR LLC, Radnor, PA, USA). The barb adapter connected to ~30 cm of 1/8” I.D. polypropylene tubing (United States Plastic Corp, Lima, OH, USA), which connected to a 1/8” I.D. to male polypropylene luer lock barb adapter (RSN Lab Store). The male luer lock was attached to a 20-gauge blunt tip polypropylene female luer lock hub needle (Jensen Global, Santa Barbara, CA, USA).

2.2.7 Visudyne-Like Verteporfin Formulation

VP, 1,2-dimyristoyl-sn-glycero-3-phosphocholine (DMPC, Avanti Polar Lipids, Alabaster, AL, USA), L-α-phosphatidylglycerol (Egg PG, Avanti Polar Lipids, Alabaster, AL, USA), [16-[(7-nitro-2-1,3-benzoxadiazol-4-yl)amino] palmitic acid (NBD Palmitic Acid, Avanti Polar Lipids, Alabaster, AL, USA), and butylhydroxytoluene (MilliporeSigma, Burlington, MA, USA) were mixed in a 1:3:5:0.1:0.1 molar ratio in chloroform. The mixture was flash-frozen *via* submersion in liquid nitrogen. Chloroform was removed from the sample *via* lyophilization on a FreeZone 6 L Console Freeze Dryer (Labconoco Corp., Kansas City, MO, USA). Samples were stored at -20°C in the dark until use, at which point they were vortexed with sterile PBS containing calcium and magnesium.

2.2.8 Liposomal Verteporfin Synthesis

Liposomes containing VP within phospholipid bilayers were synthesized *via* the freeze-thaw extrusion technique and characterized following our protocol [112]. Briefly, dipalmitoylphosphatidylcholine (DPPC), cholesterol, distearoylphosphatidylethanolaminemethoxy polyethylene glycol (DSPE-mPEG2000), and dioleoyltrimethylammoniumpropane (DOTAP; Avanti Polar Lipids) were mixed in chloroform at 6:3:0.3:0.7 molar ratio and dissolved with 50-200 nanomoles of VP (US Pharmacopeia). Chloroform was removed by a rotary evaporator to create a thin lipid film, which was rehydrated with 1 mL of ultrapure deionized water (Invitrogen). The phospholipid VP suspension was subjected to freeze-thaw cycles (4-45°C). The dispersions were extruded through polycarbonate membranes (0.1 μm pore size; Avanti Polar Lipids) at 45°C to form unilamellar vesicles. Liposomal VP samples

were dialyzed against 1X PBS at 4°C and stored at 4°C until use. The concentration and loading capacity of liposomal VP were determined by ultraviolet-visible (UV-Vis) spectroscopy. Dynamic Light Scattering (DLS) was used to measure hydrodynamic diameter, and Pdi on a particle sizer and Zeta potential was measured using a Zeta potential analyzer (NanoBrook Omni, Brookhaven Instruments).

2.2.9 Statistics

Statistical tests were carried out using GraphPad Prism (GraphPad Software, San Diego, CA, USA) or Microsoft Excel (Microsoft, Redmond, WA, USA). For nanoparticle parameter descriptions, one-way ANOVA statistical tests with Tukey post-hoc tests were performed. For DLS diameter curves, data are presented as mean ± standard deviation. For TEM image quantification, particle diameter was measured using ImageJ, and particle frequency (defined as the frequency of values within a specific histogram bin) is plotted, with a nonlinear fit curve overlayed. For Pdi and Zeta Potential, the central bar indicates the mean, with boxes extending to minimum and maximum values. For diameter cartoons, mean is shown as a thin-lined black circle, with standard deviation represented as green or grey concentric circles. For pH response, raw values are shown. For concentration, data is shown as mean ± standard deviation. For relationships between hydrodynamic diameter, Pdi, and Zeta potential, best-fit lines were produced by simple linear regression. Dotted lines indicate confidence interval.

2.3 Results

2.3.1 Evaluation of Solvents in the Initial Formulation of NanoVP

Solvent-antisolvent precipitation requires the solvent for the drug of interest to be miscible with an aqueous solution, resulting in supersaturation, nucleation, and particle growth [174]. We screened a panel of five organic solvents by adding VP dissolved in solvent dropwise to water, then dialyzing the suspension into PBS (**Figure 2-1A**). VP was dissolved in organic solvent at 7 mM for DMSO, acetone, and ACN, and at the maximum solubility in EtOH (~5 mM) and MeOH (~4 mM). After allowing the solutions to settle, in some cases, larger aggregates and precipitates fell to the bottom of the tube (visible as dark material at the bottom of each sample; left sample of **Figure 2-1C, 2-1D, 2-1E, 2-1F**). Only DMSO did not result in settling of gross aggregates (left sample of **Figure 2-1B**). Agitation of the sample resuspended the settled aggregates in all samples but DMSO (middle sample of **Figure 2-1B, 2-1C, 2-1D, 2-1E, 2-1F**). Through dynamic light scattering (DLS), we evaluated the size of particles in an agitated sample (**Figure 2-1G, 2-1H, 2-1I, 2-1J, 2-1K**) and in the sample filtered with a 0.22 μm filter (**Figure 2-1L, 2-1M, 2-1N, 2-1O, 2-1P**). Only DMSO resulted in monodisperse particles before filtration, and samples for acetone, EtOH, and MeOH resulted in single peaks after filtration. Significant material loss was noted after filtration for ACN, EtOH, and MeOH (right sample in **Figure 2-1D, 2-1E, 2-1F**).

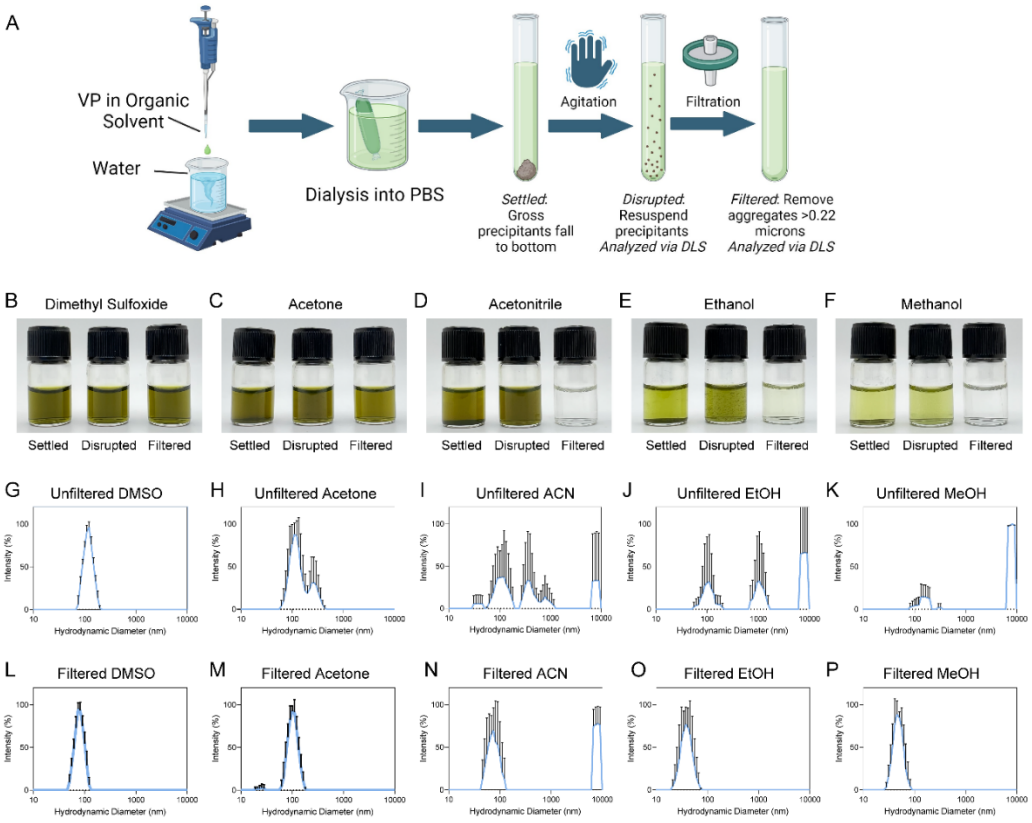

Figure 2-1. Evaluation of solvent on initial formation of nanoaggregates of verteporfin. (A) Workflow for evaluation of other solvents in the formulation of NanoVP. After dropwise solvent-antisolvent precipitation, samples were dialyzed into PBS, then allowed to settle for at least 48 hours. Samples were then agitated and filtered before dynamic light scattering (DLS) measurements. Some samples had aggregates settle after production (left, B, C, D, E, F), which were manually agitated before DLS measurements (middle, B, C, D, E, F). Samples were also filtered before DLS measurements to remove larger aggregates (right, B, C, D, E, F). DLS measurements of agitated, unfiltered samples (G, H, I, J, K) revealed larger aggregates in some cases. DLS measurements on filtered samples (L, M, N, O, P) resulted in purified populations of nanoaggregates. Data shown as mean ± SD. For all groups, $n \geq 3$; DLS traces are from one representative sample per group, with three reads per sample. Graphic (A) made with BioRender.*

* This figure was first published in Quinlan JA, Baumiller K, Gaur A, Chiow W-A, Robey RW, Gottesman MM, and Huang H-C, "Self-Assembled Verteporfin Nanoparticles for Photodynamic and Light-Independent Therapy in Glioblastoma." *Adv NanoBiomed Res.* 2024;2400098. doi: 10.1002/anbr.202400098.

2.3.2 Characterization of NanoVP

NanoVP was formulated by solvent-antisolvent precipitation (**Figure 2-2A**) under parameters outlined in **Table 2-1** as Condition 2. The resulting solution is a dark green translucent nanosuspension of VP, termed NanoVP (**Figure 2-2B**). NanoVP under these initial formulation conditions has a diameter of 109 ± 0.8 nm by DLS with a Pdi of 0.12 ± 0.003 and a Zeta potential of -22.0 ± 0.93 mV (**Figure 2-2C**). TEM images reveal a roughly spherical particle (**Figure 2-2D, 2-2E**) with a diameter of 55.1 ± 29 nm (n=380 particles) (**Figure 2-2F**). Close up TEM (**Figure 2-2G**) and electron diffraction (**Figure 2-2H**) indicate particles are amorphous, with some potential crystalline structure as indicated by the faint halo, although this may be artifact of PBS that was dialyzed off before electron diffraction. We also formulated a liposomal formulation of VP like Visudyne (**Figure 2-3A, 2-3B**) [175] to use as a control. DLS analysis revealed that this formulation had a wide range of diameters (1010 ± 1210 nm; **Figure 2-3C, 2-3D**), a Pdi >0.2, and a negative surface charge (**Figure 2-3E**).

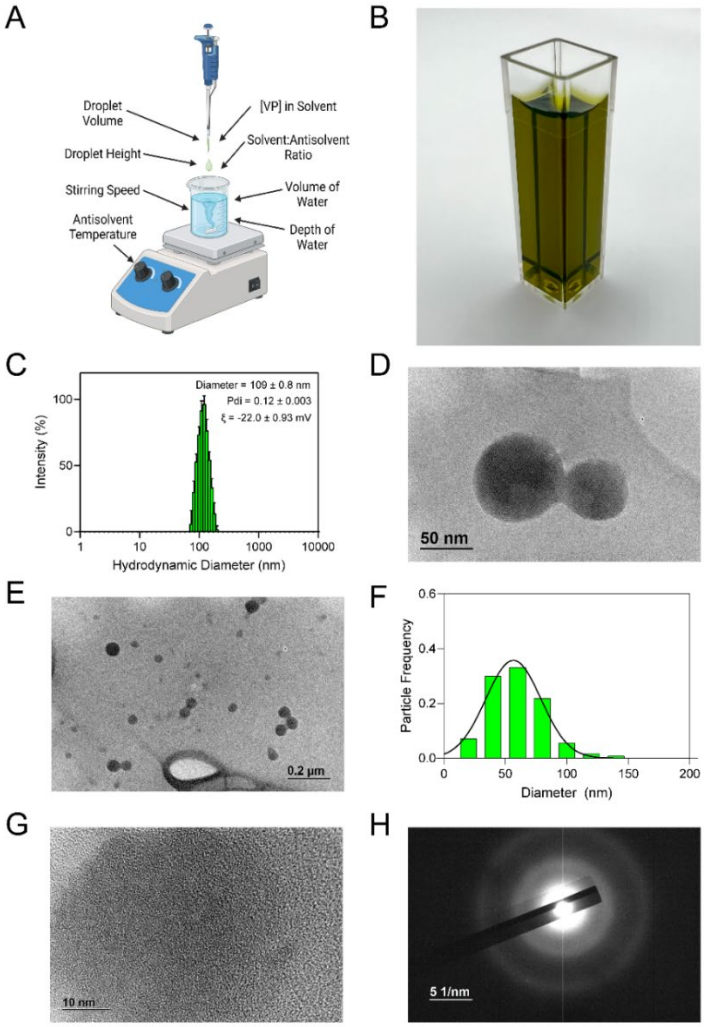

Figure 2-2. Characteristics of the initial formulation of NanoVP. (A) VP dissolved in DMSO is added dropwise to stirring water, resulting in (B) a nanosuspension that is transparent and green in color with no gross aggregates.(C) NanoVP is monodispersed with a negative charge. (D, E) TEM images reveal that NanoVP is roughly spherical. (F) Quantification of diameter from TEM images shows a diameter of 55.1 ± 29 nm (n=380 particles). (G) Close-up TEM and (H) a lack of patterning in electron diffraction indicates an amorphous structure of NanoVP (scale bar is 5 1/nm). Data represented as mean ± SD except for TEM quantification, where raw particle frequency is shown. For all groups, n ≥ 3. Graphic (A) made with BioRender.[*]

[*] This figure was first published in Quinlan JA, Baumiller K, Gaur A, Chiow W-A, Robey RW, Gottesman MM, and Huang H-C, "Self-Assembled Verteporfin Nanoparticles for Photodynamic and Light-Independent Therapy in Glioblastoma." *Adv NanoBiomed Res.* 2024;2400098. doi: 10.1002/anbr.202400098.

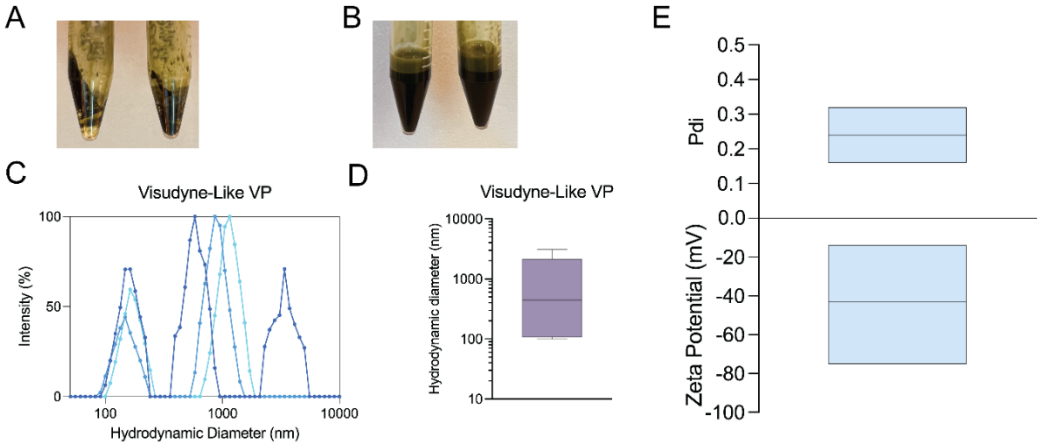

Figure 2-3. Visudyne-like verteporfin. (A) VP was mixed with appropriate lipids in chloroform, then flash-frozen in liquid nitrogen. The frozen mixture was lyophilized for 24 hours, then stored at -20°C in the dark until use. At the time of use, (B) the film was resuspended in PBS with calcium and magnesium *via* vortexing. Particle analysis revealed (C) broad peaks, indicating many particles of varying size. (D) The mean diameter was 1010 ± 1210 nm. (E) The Pdi was 0.24 ± 0.07, and the Zeta potential was -43.2 ± 25. DLS traces show three replicate reads from a single representative sample. Hydrodynamic diameter is presented with a bar at the mean, bars and whiskers extending to maximum and minimum, and the box extends from the lower to upper quartile. For Pdi and Zeta potential, a bar is at the mean, and boxes extend to the maximum and minimum.[*]

[*] This figure was first published in Q Quinlan JA, Baumiller K, Gaur A, Chiow W-A, Robey RW, Gottesman MM, and Huang H-C, "Self-Assembled Verteporfin Nanoparticles for Photodynamic and Light-Independent Therapy in Glioblastoma." *Adv NanoBiomed Res.* 2024;2400098. doi: 10.1002/anbr.202400098.

2.3.3 Identification of Key Factors in the Formulation of NanoVP

First, we increased the solvent:antisolvent ratio and concentration of VP in DMSO in the initial solvent-antisolvent synthesis scheme in order to increase overall solution concentration. We noticed an increase in NanoVP size with increased solvent-antisolvent ratio (**Figure 2-4A**) and increased concentration of VP in DMSO (**Figure 2-4B**). With these parameters altered, the nanostructure visualized *via* TEM remained amorphous and spherical (1 mM VP in DMSO with 2% DMSO:water ratio, **Figure 2-4C**; 20 mM VP in DMSO with 2% DMSO:water ratio, **Figure 2-4D**; 7 mM VP in DMSO with 6% DMSO:water ratio, **Figure 2-4E**; 7 mM VP in DMSO with 25% DMSO:water ratio, **Figure 2-4F**). A starting VP concentration beyond 15 mM or a DMSO:water ratio higher than 6% resulted in multi-peak size distribution (**Figure 2-4A, 2-4B).**

Nanoparticle tracking analysis was used to quantify the number of particles formed for each construct, and calculate how many molecules of VP were loaded into each particle. Nanoparticle tracking analysis revealed $(1.04 \pm 0.22) \times 10^{14}$ liposomal VP per milliliter and $(1.04 \pm 0.22) \times 10^{14}$ NanoVP per milliliter at the initial formulation condition (7 mM VP in DMSO, 2% DMSO to water ratio), with particle number increasing with increased initial concentration of VP in DMSO (**Figure 2-5A**). NanoVP formulated at the most stable conditions (7 mM VP in DMSO, 1:50 DMSO:water ratio) contained approximately $(7.06 \pm 0.38) \times 10^{5}$ VP particles per construct, while liposomal VP contained approximately 485 ± 75 VP molecules per construct (**Figure 2-5B**), representing 1455-fold greater VP loading per construct for

NanoVP compared to liposomal VP and consistent with previous estimates of VP loading in liposomal VP [112, 130].

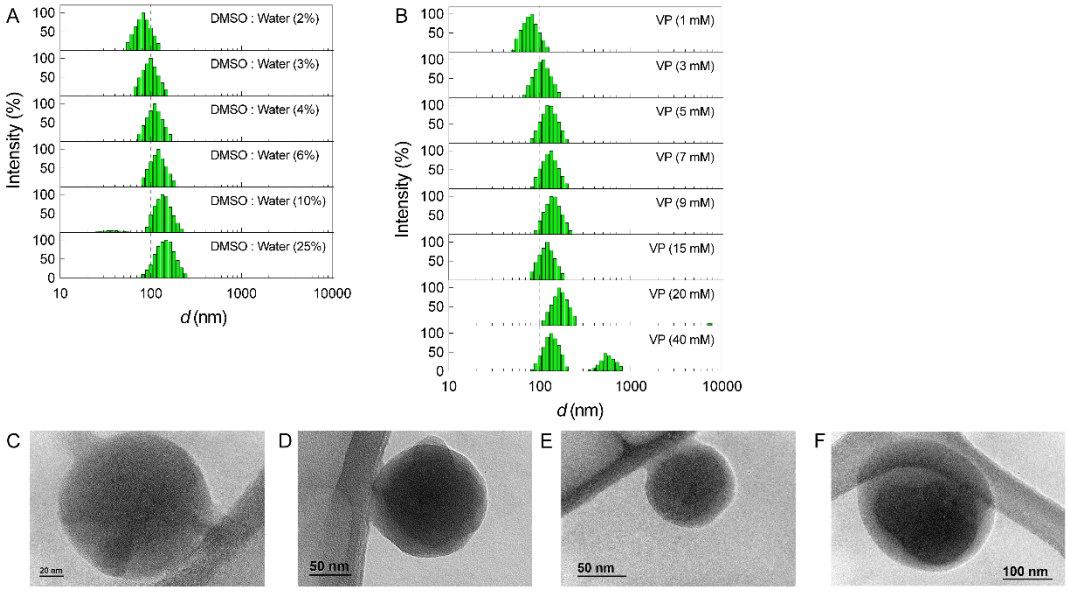

Figure 2-4. NanoVP parameters to increase concentration changes diameters. Representative intensity plots of NanoVP as a function of (A) DMSO: Water ratio and (B) initial VP concentration. Representative TEM images of NanoVP formulated as (C) 1 mM VP in DMSO with 2% DMSO:water ratio, (D) 20 mM VP in DMSO with 2% DMSO:water ratio, (E) 7 mM VP in DMSO with 6% DMSO:water ratio, and (F) 7 mM VP in DMSO with 25% DMSO:water ratio.*

* This figure was first published in Quinlan JA*, Inglut CT*, Srivastava P, Rahman I, Stabile J, Gaitan B, Arnau del Valle C, Baumiller K, Gaur A, Chiou W-A, Karim B, Connoly N, Robey RW, Woodworth GF, Gottesman MM, and Haung H-C, "Carrier-Free, Amorphous Verteporfin Nanodrug for Enhanced Photodynamic Cancer Therapy and Brain Drug Delivery." *Adv Sci (Weinh).* 2024;11(17):e2302872. doi:10.1002/advs.202302872.

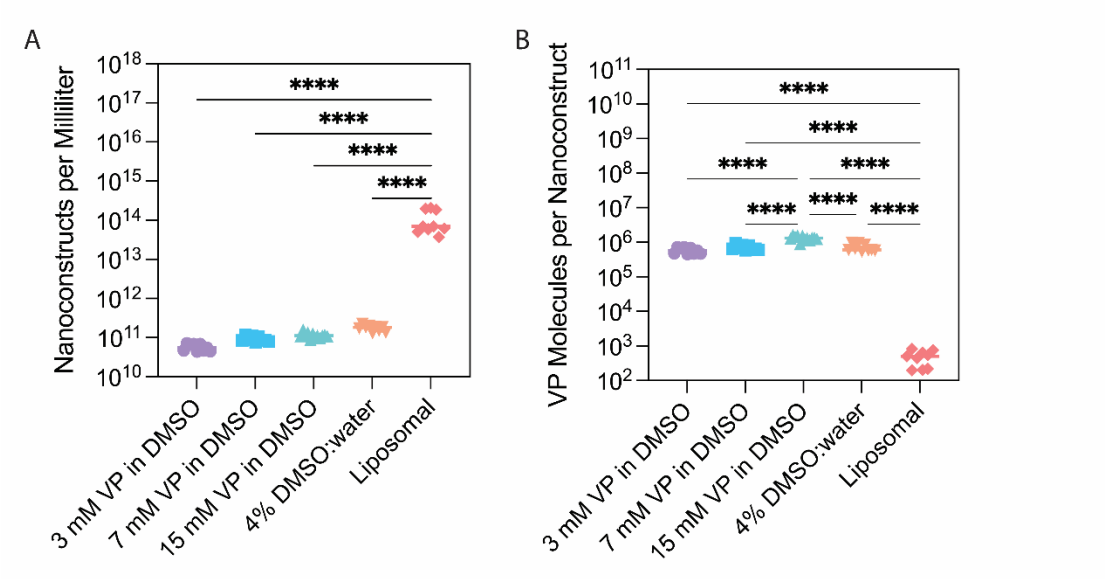

Figure 2-5. Quantification of nanoconstruct concentration and loading. Nanoparticle tracking analysis reveals that (A) NanoVP, under several formulation conditions, contains fewer nanoconstructs per milliliter of nanosuspension than NanoVP, with (B) more VP molecules per nanoconstruct than liposomal VP. The 3 mM, 7 mM, and 15 mM samples were 2% DMSO in water, and the 4% DMSO in water sample was 7 mM. Individual data points of raw (A) and calculated (B) values are shown. By one-way ANOVA with Tukey's multiple comparison test, **** indicates $p<0.0001$. For all conditions, $n>3$.

Upon noting this trend in size change, we explored other parameters that impacted characteristics of the nanoparticles. Of the eight identified tunable factors, we found three that significantly impacted the size of NanoVP. The stirring speed of the water was inversely proportional to diameter, as still water (0 revolutions per minute (RPM)) resulted in NanoVP with a diameter of 120 ± 15 nm and water stirred at 1500 RPM resulted in NanoVP with a diameter of 59.7 ± 4.0 nm (**Figure 2-6A**). This resulted in uniform, single-peaked samples (**Figure 2-6B**) and did not impact Pdi or Zeta potential (**Figure 2-6C**). The height at which the pipette was held above the surface of the water also had an inverse on particle diameter. A droplet height of 1 cm resulted in NanoVP with a diameter of 108 ± 14 nm, while a droplet height of 15 cm resulted in a NanoVP diameter of 78.9 ± 12 nm (**Figure 2-6D**). Droplet height had no impact on peakedness of DLS measurements, (**Figure 2-6E**) Pdi, or Zeta potential (**Figure 2-6F**). The concentration of VP in DMSO (VP in solvent) was directly related to NanoVP diameter. One millimolar (1 mM) VP in DMSO resulted in particles with a diameter of 65.8 ± 12 nm, while 15 mM VP in DMSO resulted in particles with a diameter of 108 ± 6.6 nm (**Figure 2-6G**). All concentrations of VP in DMSO resulted in uniform peaks at all concentrations tested (**Figure 2-6H**). Pdi was significantly lower with 7 mM VP in DMSO than 1- or 15-mM VP in DMSO, and there was no significant impact on Zeta potential (**Figure 2-6I**).

We identified five additional factors that did not impact the diameter of the nanoaggregate. The depth of the water that VP in DMSO was dropped into did not impact size (**Figure 2-7A**), but the shallowest water resulted in split peaks on DLS (**Figure 2-7B**). The shallowest water had a significantly higher Pdi than the deepest

water, with no impact on Zeta potential (**Figure 2-7C**). The temperature of water and droplet volume had no impact on diameter (**Figure 2-7D, 2-7G**), peakedness (**Figure 2-7E, 2-7H**), Pdi, or Zeta potential (**Figure 2-7F, 2-7I**). Volume of water, with depth of water fixed by using vessels with different diameters, had no impact on particle diameter (**Figure 2-7J**), Pdi, or Zeta potential (**Figure 2-7L**), but, interestingly, smaller volumes of water or larger volumes of water led to broad peaks on DLS (**Figure 2-7K**). Finally, solvent:antisolvent ratio had no impact on particle diameter (**Figure 2-7M**) or peakedness (**Figure 2-7N**) or Zeta potential, but Pdi was slightly lower with higher percents of DMSO in water (**Figure 2-7O**).

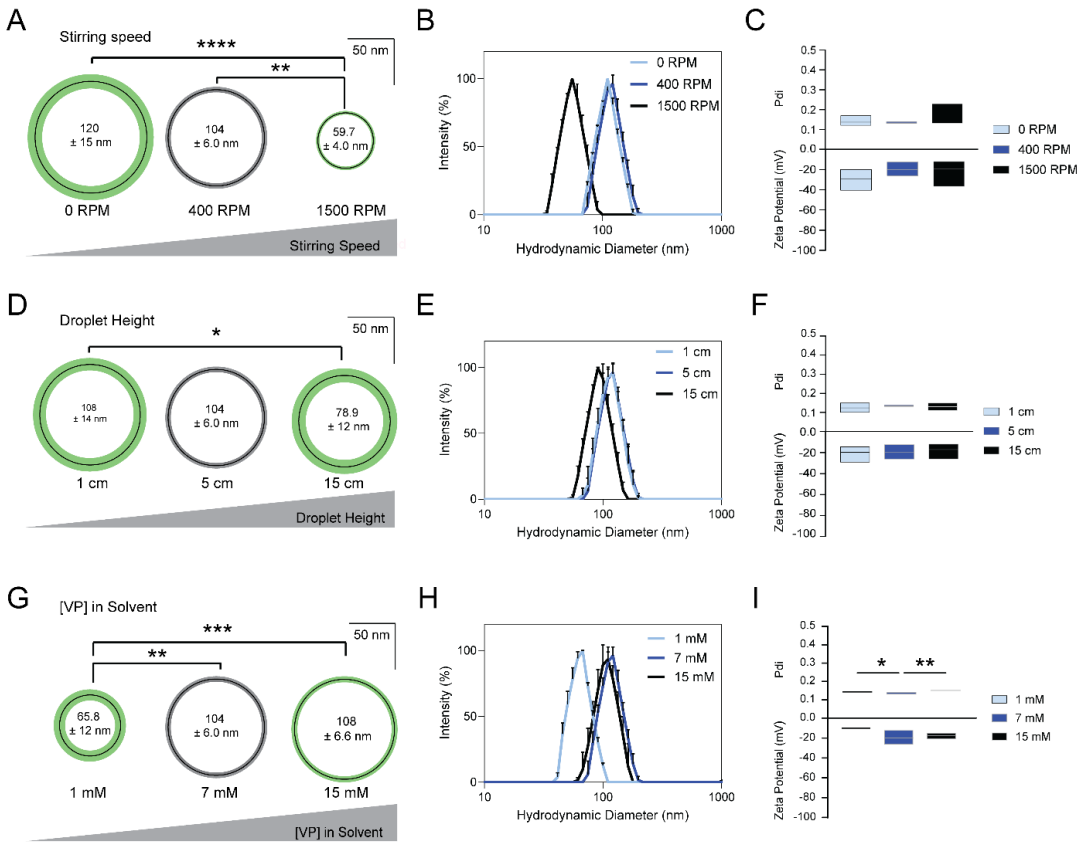

Figure 2-6. Key factors that impact the size of NanoVP. (A) NanoVP decreases in diameter when stirring speed is increased, but (B) remains monodisperse with (C) no changes to Pdi or Zeta potential. (D) As the height from which VP in DMSO is dropped increases, the diameter of NanoVP decreases, maintaining a (E) monodisperse profile with (F) consistent Pdi and Zeta potential. (G) Increasing the VP concentration in DMSO increases the size of VP, resulting in (H) a monodisperse population with (I) a slight increase in Pdi at either extreme of concentration and no changes in Zeta potential. For (A, D, G), thin black circles indicate mean diameter, green or grey concentric rings indicate SD. Grey rings indicate a representative population of NanoVP as described in Figure 1, against which all variations were compared. DLS traces show three replicate measures of a single representative sample. Pdi and Zeta potential indicate the median value, with boxes extending to maximum and minimum values. For all groups, $n \geq 3$. Statistics were determined by one-way ANOVA with Tukey's multiple comparisons test. * Indicates $p<0.05$, ** $p<0.01$, *** $p<0.001$, **** $p<0.0001$.*

* This figure was first published in Quinlan JA, Baumiller K, Gaur A, Chiow W-A, Robey RW, Gottesman MM, and Huang H-C, "Self-Assembled Verteporfin Nanoparticles for Photodynamic and Light-Independent Therapy in Glioblastoma." *Adv NanoBiomed Res.* 2024;2400098. doi: 10.1002/anbr.202400098.

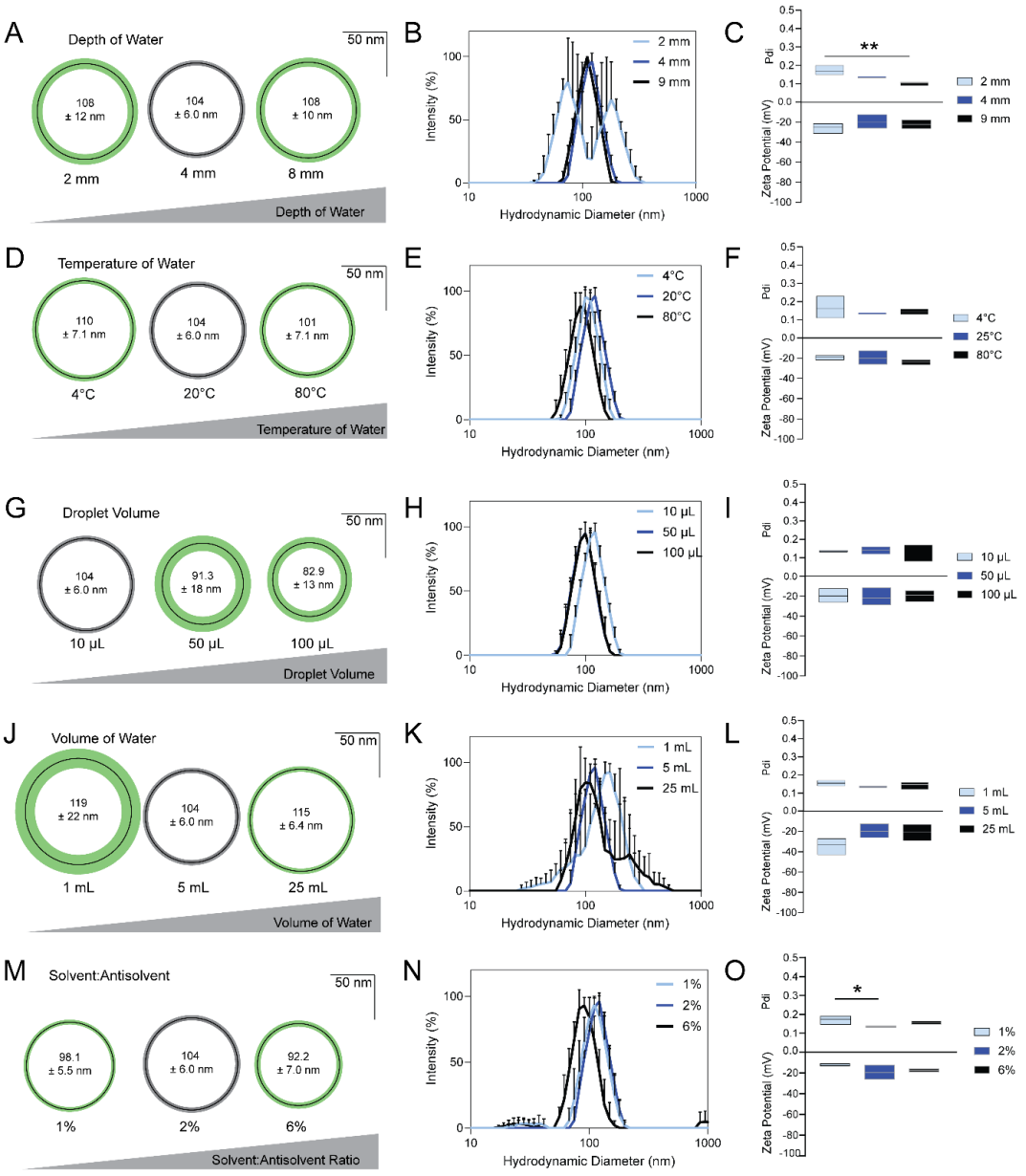

Figure 2-7. Several factors did not alter particle size but did change dispersity or Zeta potential. (A) Altering the depth of water while maintaining volume did not change particle size, but (B) shallower water resulted in a polydisperse population with (C) higher Pdi but no change to Zeta potential. (D, G) Neither temperature of water or droplet volume impacted diameter, (E, H) resulted in monodisperse populations, or (F, I) altered the Pdi or Zeta potential of NanoVP. (J) volume of water did not alter size, but (K) resulted in more polydisperse populations of nanoparticles at lower and higher volumes of water. (L) This did not impact Pdi or Zeta potential. (M) Solvent:antisolvent ratio did not impact diameter in the tested range, with (N) minimal impact on dispersity. (O) Lower solvent:antisolvent ratios did result in a higher Pdi. For (A, D, G, J, M), thin black circles indicate mean diameter, green or grey concentric rings indicate SD. Grey

rings indicate a representative population of NanoVP, as described in Figure 1, against which all variations were compared. DLS traces show three replicate measures of a single representative sample. Pdi and Zeta potential indicate the median value, with boxes extending to maximum and minimum values. For all groups, $n \geq 3$. Statistics were determined by one-way ANOVA with Tukey's multiple comparisons test. * Indicates $p<0.05$, ** $p<0.01$.[*]

[*] This figure was first published in Quinlan JA, Baumiller K, Gaur A, Chiow W-A, Robey RW, Gottesman MM, and Huang H-C, "Self-Assembled Verteporfin Nanoparticles for Photodynamic and Light-Independent Therapy in Glioblastoma." *Adv NanoBiomed Res.* 2024;2400098. doi: 10.1002/anbr.202400098.

2.3.4 Extended Ranges of NanoVP Diameters

We hypothesized that combining factors impacting nanoparticle diameter and polydispersity would enable synthesis of particles with a greater range of diameters. As such, we altered stirring speed, droplet height, and VP concentration in solvent to modify diameter, depth of water, and solvent:antisolvent ratio to modify Pdi as described in **Table 2-1**. We found that these combined factors significantly increased diameter. From the standard formulation size of 104 ± 6.0 nm, combining key factors to decrease diameter resulted in Condition 1 (**Table 2-1**) nanoparticles with a diameter of 49.0 ± 4.4 nm, and combining key factors to increase diameter resulted in Condition 3 (**Table 2-1**) nanoparticles with a diameter of 195 ± 7.1 nm (**Figure 2-8A**). On DLS, all samples had similar peakedness, although the Condition 1 nanoparticles had a population of smaller nanoparticles (**Figure 2-8B**). Consistent with this, the Condition 1 nanoparticles had a higher Pdi than the Condition 2 or Condition 3 nanoparticles (**Figure 2-8C**). Interestingly, the Condition 3 nanoparticles had a significantly more negative Zeta potential than the standard or small nanoparticles (**Figure 2-8C**). Because both the solvent-antisolvent ratio and VP concentration in solvent were increased to make the largest nanoparticle, the resulting concentration of the nanosuspension was elevated. Desiring a more concentrated, smaller diameter particle, we increased stirring speed (**Figure 2-6A**), which had the greatest single-factor impact on diameter, resulting in Condition 4 (**Table 2-1**). The resulting nanoparticles had a diameter of 63.8 ± 5.0 nm (**Figure 2-8D**), had a clean single peak on DLS (**Figure 2-8E**), a Pdi of 0.14 ± 0.01, and a Zeta potential of -17.8 ± 8.0 mV (**Figure 2-8F**). Diameter quantification from TEM confirmed that Condition 4 nanoparticles had a

diameter of 56.2 ± 16 nm with a narrow distribution, Condition 3 nanoparticles had a diameter of 112 ± 51 nm with a broad distribution, and Condition 1 nanoparticles had a diameter of 51.8 ± 19 nm with a narrow distribution (**Figure 2-8G**). Modulating both percent solvent in antisolvent and concentration of VP in solvent permitted tunability of concentration from 9.1 ± 5.2 μM for the smallest particles, 136 ± 10 μM for Condition 2 nanoparticles, 838 ± 45 μM for Condition 3 nanoparticles, and 799 ± 44 μM for Condition 4 nanoparticles (**Figure 2-8H**). By visual inspection, concentration differences are appreciable (**Figure 2-8I,** from left to right, Condition 1, Condition 2, Condition 3, and Condition 4). These different formulations resulted in an encapsulation efficiency of 92.4 ± 5.2% for Condition 1, 97.3 ± 7.1% for Condition 2, 93.1 ± 5.0% for the Condition 3, and 88.7 ± 4.9% for Condition 4.

TEM confirmed that Condition 1 nanoparticles (**Figure 2-8J, 2-8M**), Condition 3 nanoparticles (**Figure 2-8K, 2-8N**), and Condition 4 nanoparticles (**Figure 2-8L, 2-8O**) all retained a roughly spherical shape. Close-up TEM and electron diffraction for Condition 1 (**Figure 2-8P, 2-8S**), Condition 3 **(Figure 2-8Q, 2-8T**), and Condition 4 (**Figure 2-8R, 2-8U**) nanoparticles indicate that the particles remain amorphous under all formulation parameters. Slight halos on electron diffraction may be attributable to residual PBS from initial dialysis.

After observing a decrease in Zeta potential in our largest nanoparticles (**Figure 2-8C**), we investigated more global trends in parameters by diameter, Pdi, and Zeta potential data across many different formulation parameters. We found that diameter was indirectly related to Zeta potential (**Figure 2-9A**), while there was no relationship between diameter and Pdi or Pdi and Zeta potential (**Figure 2-9B, 2-9C**).

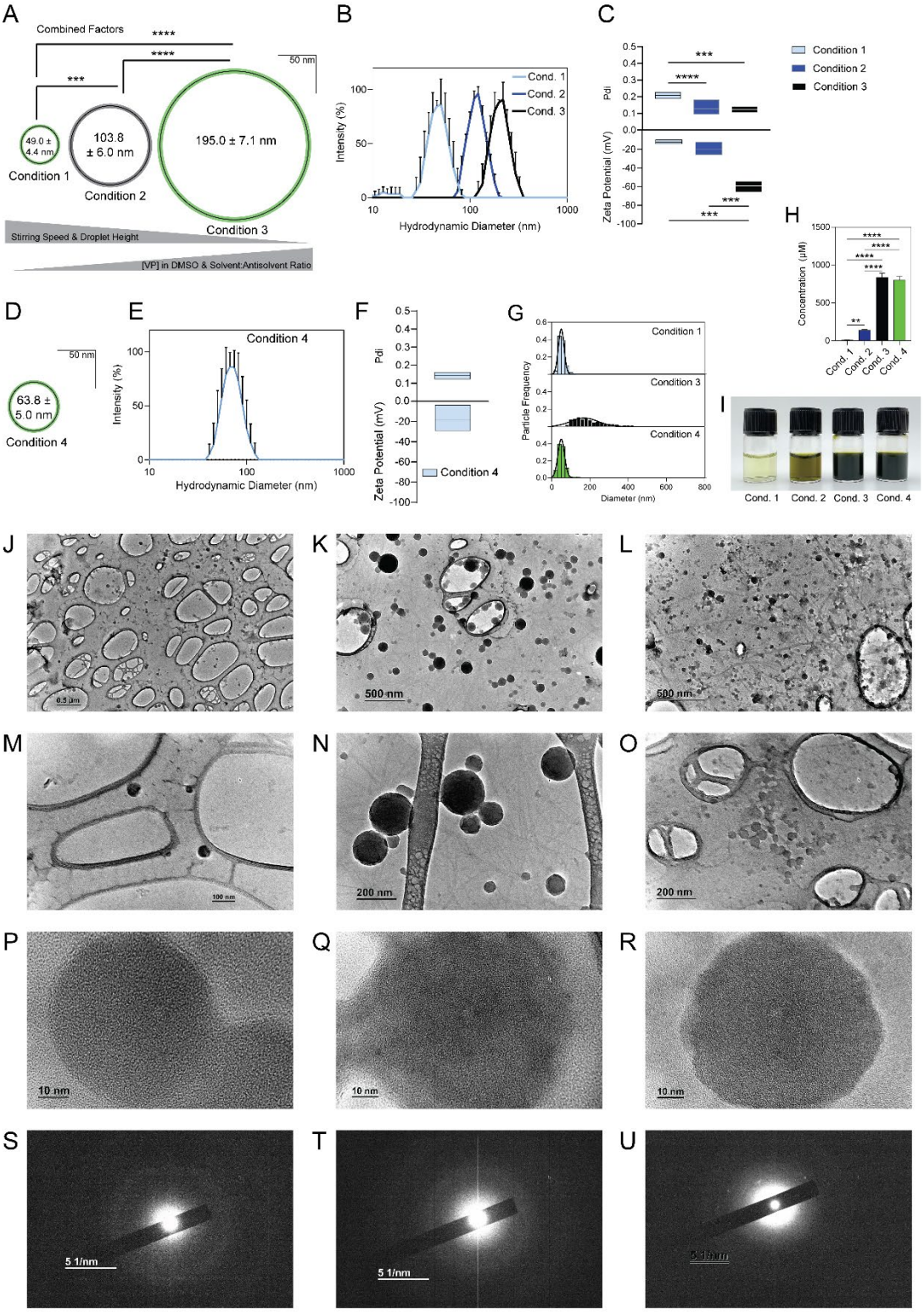
A
Combined Factors
****
****
***
50 nm
49.0 ± 4.4 nm
103.8 ± 6.0 nm
195.0 ± 7.1 nm
Condition 1
Condition 2
Condition 3
Stirring Speed & Droplet Height
[VP] in DMSO & Solvent:Antisolvent Ratio
B
Intensity (%)
Cond. 1
Cond. 2
Cond. 3
Hydrodynamic Diameter (nm)
C
Pdi
Zeta Potential (mV)
Condition 1
Condition 2
Condition 3
H
Concentration (µM)
Cond. 1
Cond. 2
Cond. 3
Cond. 4
D
50 nm
63.8 ± 5.0 nm
Condition 4
E
Condition 4
Intensity (%)
Hydrodynamic Diameter (nm)
F
Pdi
Zeta Potential (mV)
Condition 4
G
Condition 1
Condition 3
Condition 4
Particle Frequency
Diameter (nm)
I
Cond. 1
Cond. 2
Cond. 3
Cond. 4
J
0.5 µm
K
500 nm
L
500 nm
M
100 nm
N
200 nm
O
200 nm
P
10 nm
Q
10 nm
R
10 nm
S
5 1/nm
T
5 1/nm
U
5 1/nm

Figure 2-8. Extended range of NanoVP diameters. (A) As stirring speed and droplet height decrease and VP in DMSO concentration and solvent:antisolvent ratio increase, diameter of nanoparticles increases. (B) This results in single-peaked samples with (C) decreasing Pdi and more-negative Zeta potential. (D) Increasing stirring speed alone decreased nanoparticle diameter, maintaining (E) a monodisperse profile with (F) Pdi and Zeta potential around that of similarly sized nanoparticles. (G) TEM image diameter quantification revealed that Conditions 1 and 4 had a monodisperse profile, while Condition 3 had a broader range of diameters. (H) Concentration was significantly increased in Conditions 3 and 4. (I) Intensity of green tint in the nanosuspensions (Conditions 1, 2, 3, and 4; left to right) correlates with concentration value. Wide-field TEM images for the (J) Condition 1, (K) Condition 3, and (L) Condition 4 and closer-field images for (P) Condition 1, (Q) Condition 3, and (R) Condition 4 particles show roughly spherical aggregates with a range in diameter. Very close-up images and electron diffraction of (P, S) Condition 1, (Q, T) Condition 3, and (R, U) Condition 4 indicate that the particles remain amorphous at all diameters. In (U), the scale bar is 5 1/nm. For (A, D), thin black circles indicate mean diameter, green and grey concentric rings indicate SD. Grey concentric rings indicate a representative population of NanoVP as described in Figure 1, against which all variations were compared. DLS traces show three replicate measures of a single representative sample. Pdi and Zeta potential indicate the median value, with boxes extending to maximum and minimum values. For TEM quantification, raw particle frequency is shown. For all groups, $n \geq 3$. Statistics were determined by one-way ANOVA with Tukey's multiple comparisons test. *** indicates $p<0.001$, **** $p<0.0001$.[*]

[*] This figure was first published in Quinlan JA, Baumiller K, Gaur A, Chiow W-A, Robey RW, Gottesman MM, and Huang H-C, "Self-Assembled Verteporfin Nanoparticles for Photodynamic and Light-Independent Therapy in Glioblastoma." *Adv NanoBiomed Res.* 2024;2400098. doi: 10.1002/anbr.202400098.

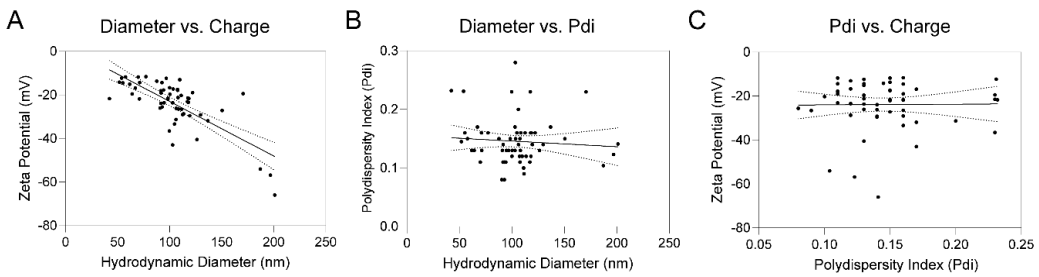

Figure 2-9. NanoVP diameter and charge are inversely related, while other nanoparticle parameters show no relationship. (A) As diameter increases, Zeta potential is more negative for NanoVP particles ($Y = -0.2506*X + 2.090$, $R^2=0.55$, $p<0.0001$). (B) Diameter vs. Pdi ($Y = -0.00009685*X +0.1555$, $R^2=0.006$, $p=0.54$) and (C) Pdi vs. Charge ($Y = -0.001109*X + 0.1176$, $R^2=0.06$, $p=0.08$) show no relationship.[*]

[*] This figure was first published in Quinlan JA, Baumiller K, Gaur A, Chiow W-A, Robey RW, Gottesman MM, and Huang H-C, "Self-Assembled Verteporfin Nanoparticles for Photodynamic and Light-Independent Therapy in Glioblastoma." *Adv NanoBiomed Res.* 2024;2400098. doi: 10.1002/anbr.202400098.

Table 2-1. Specific formulation parameters for NanoVP. From initial parameters (Condition 2), we isolated individual parameters and tested a range of values one-by-one to evaluate impact on diameter, Pdi, and Zeta potential. We combined factors based on trends to minimize size, maximize size, then to maintain concentration but reduce diameter and polydispersity of NanoVP. The "Tested Range" column indicates values tested in **Figure 2-6** and **Figure 2-7**. Only values that altered diameter, concentration, Pdi, or Zeta potential were combined to create Conditions 1, 3, and 4. As such, certain parameters that made no impact on important nanoparticle features, such as droplet volume and volume of water, were not altered in the final combined conditions. "Design Criteria" presents parameters for the ideal formulation of NanoVP. Traits of Visudyne as reported by others [130, 175] are reported in Column 8. By these measures, Condition 4 best met our design goal in all traits except encapsulation efficiency and Zeta potential. For measurements, data is presented as mean ± SD.*

Parameter	Range Tested	Condition 1	Condition 2 (Initial)	Condition 3	Condition 4 (Ideal)	Design Criteria	Visudyne [130, 175]
Droplet Volume (µL)	10-100	10	10	10	10	-	-
Droplet Height (cm)	1-15	15	5	1	15	-	-
Stirring Speed (RPM)	0-1500	1500	400	0	1500	-	-
Antisolvent Temperature (°C)	4-80	20	20	20	20	-	-
[VP] in Solvent (mM)	1-15	1	7	15	15	-	-
Solvent:Antisolvent Ratio (%)	1-6	1	2	6	6	-	-
Volume of Water (mL)	1-25	5	5	5	5	-	-
Depth of Water (mm)	2-8	4	4	4	8	-	-
Diameter (nm)	-	49.0 ± 4.4	104 ± 6.0	195 ± 7.1	63.8 ± 5.0	<64	524.8 ± 547.5; 733.8 ± 488.9
Concentration (µM)	-	9.1 ± 5.2	136 ± 10	838 ± 45	799 ± 44	>500	2780 (Theoretical)
Polydispersity	-	0.21 ± 0.02	0.12 ± 0.01	0.12 ± 0.02	0.14 ± 0.01	<0.20	0.88 ± 0.22; 0.66 ± 0.20
Zeta Potential (mV)	-	-12.1 ± 1.8	-22.0 ± 0.93	-59.0 ± 5.1	-17.8 ± 8.0	<-30	0.155 ± 0.210; 0.16 ± 0.21
Encapsulation Efficiency (%)	-	92.4 ± 5.2	97.3 ± 7.1	93.1 ± 5.0	88.7 ± 4.9	>90	-

* This table was first published in Quinlan JA, Baumiller K, Gaur A, Chiow W-A, Robey RW, Gottesman MM, and Huang H-C, "Self-Assembled Verteporfin Nanoparticles for Photodynamic and Light-Independent Therapy in Glioblastoma." *Adv NanoBiomed Res.* 2024;2400098. doi: 10.1002/anbr.202400098.

2.3.5 Storage Conditions and Scale-Up of NanoVP Production

Anticipating the use of NanoVP in experimental models and clinical settings, we evaluated the stability of NanoVP in different medias. After NanoVP (Condition 2) was made in water, it was dialyzed into PBS, Instant Ocean, 5% dextrose, or 0.9% NaCl. We found that the diameter of NanoVP was unchanged in PBS, Instant Ocean, and 5% dextrose, but increased with 0.9% NaCl (**Figure 2-10A**). Similarly, the Pdi increased for 0.9% NaCl only (**Figure 2-10B**). DLS revealed that the change in size and Pdi were likely due to a more varied population of nanoaggregates in 0.9% NaCl (**Figure 2-10C**). We probed the pH of each solution. PBS had a pH of 7.41 ± 0.04, Instant Ocean had a pH of 9.57 ± 0.09, 5% dextrose had a pH of 7.40 ± 0.20, and 0.9% NaCl had a pH of 6.42 ± 0.01. When the pH of PBS was changed then mixed with VP, we found that stability was lost at a pH of 4.5 or lower and 10.5 (**Figure 2-10D**, light blue lines indicate the acid dissociation constants (pKas) of VP).

We also evaluated the long-term storage of NanoVP. Stored at 4°C, NanoVP, synthesized using 1-25 mM VP in DMSO and 2-25% DMSO:water ratio, was found stable for over one year in PBS (**Figure 2-11A, 2-11B**) and VP in DMSO concentrations from 1-9 mM VP in DMSO were stable for over one year in water (**Figure 2-11C**). We found that NanoVP was unstable after freezing at -20ºC or -80°C for 90 days, but that it was stable at room temperature and at 4°C for 90 days (**Figure 2-12A, 2-12B**). Interestingly, liposomal VP remained stable after freezing at -20°C for 90 days (**Figure 2-12A, 2-12B).**

Aiming to improve consistency of NanoVP, we affixed a syringe pump and blunt-tip needle to either end of tubing using Luer-lock adapters (**Figure 2-13A**). We

drew VP in DMSO up into the needle using the pump, thus only loading the volume of VP in DMSO needed for a single batch. NanoVP was made under the parameters listed in Condition 2 (**Table 2-1**). To evaluate the impact on droplet rate, we set the pump speed at 0.1, 0.5, or 2 mL/min. We found that changing pump rate did not impact particle diameter, (**Figure 2-13B**), did not result in multipeaked DLS measurements (**Figure 2-13C**), and did not impact Pdi or Zeta potential (**Figure 2-13D**); all values were like that of handmade NanoVP (**Figure 2-13B, 2-13C, 2-13D**). It should be noted that all pump speeds, and the hand-made process, allow the VP in DMSO to accumulate on the tip of the pipette or needle and then fall by the force of gravity. The rate at which the drops fell is summarized in **Table 2-2.**

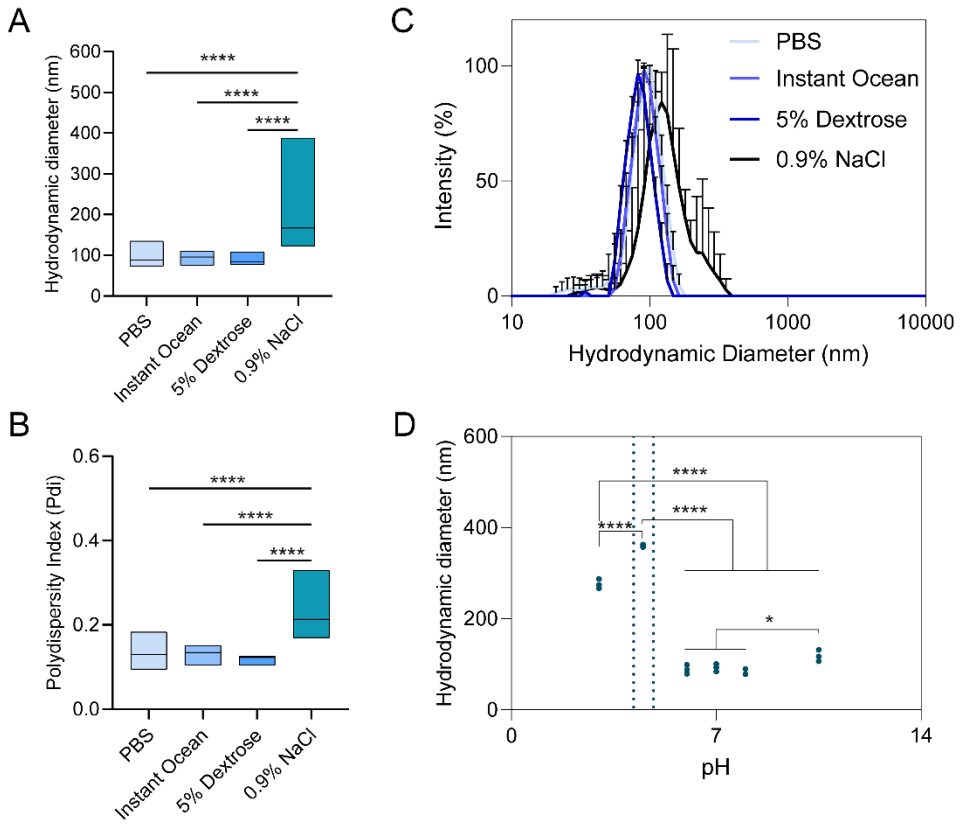

Figure 2-10. NanoVP dialyzed into different media impacts its stability. (A, B) The diameter and Pdi of NanoVP remain constant in PBS, Instant Ocean and 5% dextrose, but are lost in 0.9% NaCl. (C) DLS reveals monodisperse particles in PBS, Instant Ocean, and 5% dextrose, but not 0.9% NaCl. (D) NanoVP, when mixed with solutions of various pHs, remains stable in the pH 6-8 range, but loses stability at a pH of 10.5 and at a pH of 4.5 or 3. Light blue vertical lines in (D) indicate the pKas of VP. For hydrodynamic diameter and Pdi, data are represented as a mean (central bar) with boxes extending to the maximum and minimum. For all groups, $n \geq 3$. Statistics were determined by one-way ANOVA with Tukey's multiple comparisons test. * Indicates $p<0.05$, **** $p<0.0001$.[*]

[*] This figure was first published in Quinlan JA, Baumiller K, Gaur A, Chiow W-A, Robey RW, Gottesman MM, and Huang H-C, "Self-Assembled Verteporfin Nanoparticles for Photodynamic and Light-Independent Therapy in Glioblastoma." *Adv NanoBiomed Res.* 2024;2400098. doi: 10.1002/anbr.202400098.

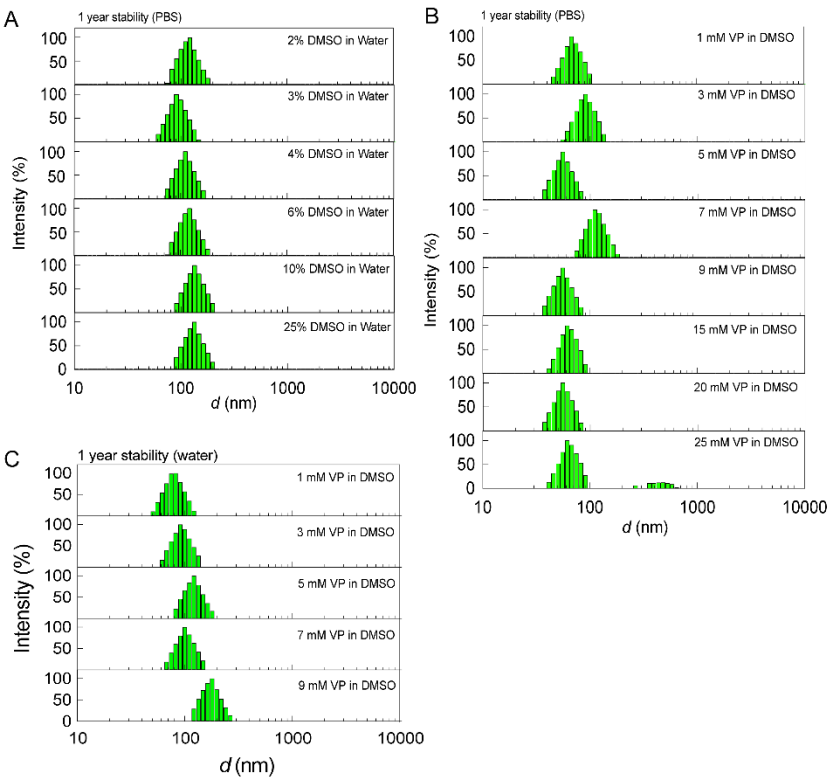

Figure 2-11. The long-term shelf life of NanoVP was formulated under various conditions. Representative intensity plots of (A) varying DMSO:water ratios dialyzed into PBS, (B) varying VP in DMSO concentrations dialyzed into PBS, and (C) varying VP in DMSO concentrations in water.[*]

[*] This figure was first published in Quinlan JA*, Inglut CT*, Srivastava P, Rahman I, Stabile J, Gaitan B, Arnau del Valle C, Baumiller K, Gaur A, Chiou W-A, Karim B, Connoly N, Robey RW, Woodworth GF, Gottesman MM, and Haung H-C, "Carrier-Free, Amorphous Verteporfin Nanodrug for Enhanced Photodynamic Cancer Therapy and Brain Drug Delivery." *Adv Sci (Weinh).* 2024;11(17):e2302872. doi:10.1002/advs.202302872

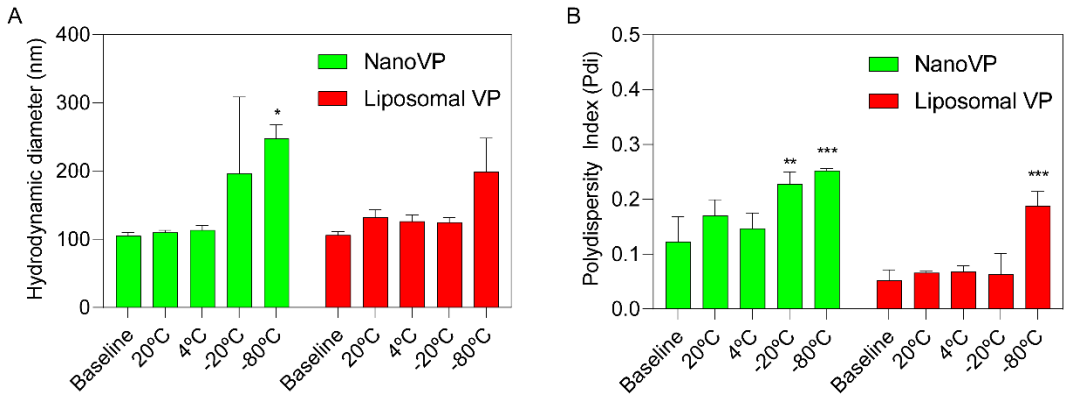

Figure 2-12. NanoVP and liposomal verteporfin shelf life at different storage temperatures. NanoVP made under standard conditions (7 mM VP in DMSO, 2% DMSO:water ratio) were stored for 90 days at room temperature, 4°C, -20°C, and -80°C. (A) Hydrodynamic diameter and (B) Pdi at baseline (immediately after formulation) were compared to values after storage. Two-way ANOVA with multiple comparison test was used to calculate significant differences, where * $P < 0.05$, ** $P < 0.01$, *** $P < 0.001$. Error bars show SEM.[*]

[*] This figure was first published in Quinlan JA*, Inglut CT*, Srivastava P, Rahman I, Stabile J, Gaitan B, Arnau del Valle C, Baumiller K, Gaur A, Chiou W-A, Karim B, Connoly N, Robey RW, Woodworth GF, Gottesman MM, and Haung H-C, "Carrier-Free, Amorphous Verteporfin Nanodrug for Enhanced Photodynamic Cancer Therapy and Brain Drug Delivery." *Adv Sci (Weinh).* 2024;11(17):e2302872. doi:10.1002/advs.202302872

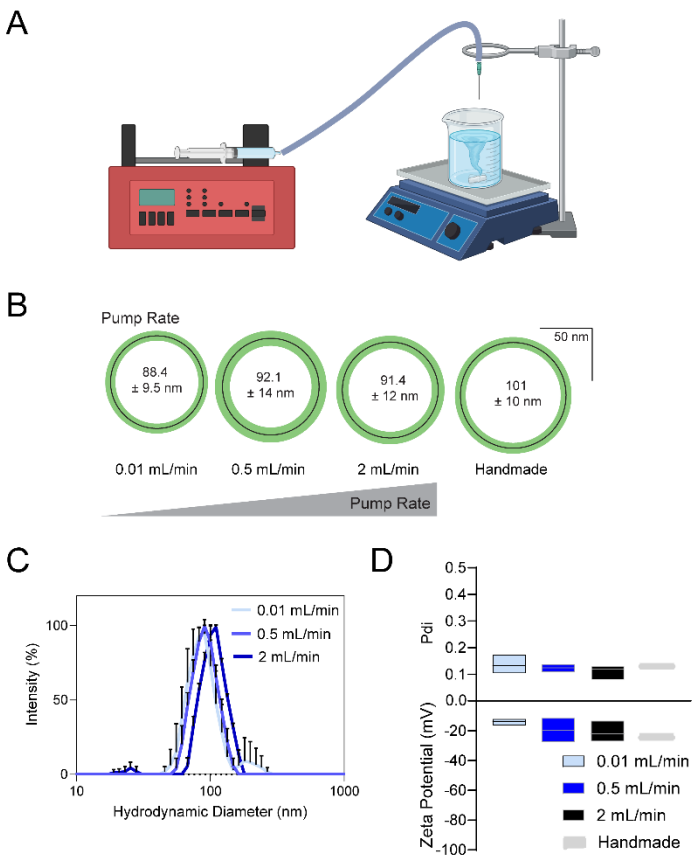

Figure 2-13. Automated production of NanoVP. (A) A syringe-pump system was affixed to tubing connected to a blunt-tip needle, permitting dropwise addition of VP in DMSO to stirred water. (B) With all parameters identified in hand-made NanoVP held constant, altering pump rate had no impact on size compared to hand-made NanoVP. (C) Pump-made NanoVP resulted in single-peaked DLS measures, and (D) had no impact on Pdi or Zeta Potential. For Pdi and Zeta potential, data are represented as a mean (central bar) with boxes extending to the maximum and minimum. For all groups, $n \geq 3$. Statistics were determined by one-way ANOVA. Graphic (A) made with BioRender.[*]

[*] This figure was first published in Quinlan JA, Baumiller K, Gaur A, Chiow W-A, Robey RW, Gottesman MM, and Huang H-C, "Self-Assembled Verteporfin Nanoparticles for Photodynamic and Light-Independent Therapy in Glioblastoma." *Adv NanoBiomed Res.* 2024;2400098. doi: 10.1002/anbr.202400098.

Table 2-2. Drops per 100 µL and estimated drop volume for each pump made NanoVP rate and handmade NanoVP. For both pump-made and handmade samples, NanoVP in DMSO accumulated at the tip of the needle or pipette and fell into the water under the force of gravity. There were no significant differences in the number of droplets per formulation method or the volume of each droplet. Data presented as mean ± SD.[*]

Pump Rate	Drops per 100 µL	Estimated Drop Volume (µL)
2 mL/min	11.0 ± 0.8	9.1 ± 0.7
1 mL/min	11.3 ± 0.5	8.8 ± 0.4
0.5 mL/min	11.0 ± 0.8	9.1 ± 0.7
0.1 mL/min	11.3 ± 0.5	8.8 ± 0.4
0.01 mL/min	11.0 ± 0.8	9.1 ± 0.7
Handmade	12.7 ± 0.5	7.9 ± 0.3

[*] This table was first published in Quinlan JA, Baumiller K, Gaur A, Chiow W-A, Robey RW, Gottesman MM, and Huang H-C, "Self-Assembled Verteporfin Nanoparticles for Photodynamic and Light-Independent Therapy in Glioblastoma." *Adv NanoBiomed Res.* 2024;2400098. doi: 10.1002/anbr.202400098.

2.4 Discussion

We observed that DMSO produced monodisperse nanoaggregates without the need for filtration. Even after filtration with a 0.22 μM syringe, NanoVP produced with DMSO did not have a significant concentration change and peakedness did not change, indicating that samples less than 220 nm in diameter could be sterile filtered – an important step for further clinical translation of the nanosuspension. Acetone produced a slightly more polydisperse population and required filtration to reduce the range of particle sizes. We observed uncontrolled aggregation with clear precipitation of large aggregates when we attempted to make particles with acetonitrile, ethanol, or methanol. While purification *via* filtration did result, in most cases, in clean peaks, the material loss associated with these solvents was too great to warrant further investigation. Others have reported that materials with low water solubility have higher diffusivity within the more polar solvent phase (e.g. VP in DMSO), while higher viscosity of the solvent may limit mixing with aqueous solution [176]. From this, rapid movement of VP within DMSO balanced with slower mixing of DMSO with water may permit a favorable balance of nucleation and growth, resulting in consistently sized particles. Other solvents may have failed to provide a balanced nucleation and growth rate. For example, EtOH and MeOH were near maximal saturation when mixed with water, so there was likely no controlled rate of nucleation or growth, resulting in the formation of primarily large aggregates.

Our initial formulation of NanoVP resulted in a roughly spherical amorphous nanoaggregate of VP using a robust and reproducible synthesis scheme. We maintained the spherical and amorphous structure of these particles as we tuned two parameters to

increase concentration, observing a trend towards increased diameter. From this, we identified factors important to the formulation of NanoVP: three that modulate the diameter of the nanoformulation, three that altered the Pdi, two that altered peakedness of particles, and two that were inconsequential to NanoVP characteristics. In solvent-antisolvent precipitation, particle diameter is a result of a balance between nucleation and growth. Nucleation is the process by which initial aggregates form spontaneously or around contaminants in solution. Growth is the process by which monomers join existing aggregate sites [177, 178]. This process is thought to be dependent on the local concentration of supersaturated particles, permitting nucleation, and the flux of monomers surrounding nucleation sites. Factors that reduced diameter of particles (e.g., increased stirring speed, increased droplet height, decreased VP concentration in DMSO) likely increased flux of monomers around nucleation sites, resulting in smaller diameter particles. Alternatively, the mixing of miscible solvent and antisolvent can be considered in terms of mesomixing (turbulent mixing of the two fluids as a smaller volume of feed fluid enters a bulk fluid) and micromixing (diffusion of one fluid in another). Increasing stirring speed likely increased the rate of micromixing, as stirring increased the rate of diffusion of VP in eddies of DMSO throughout the bulk of the water [179, 180]. As such, nucleation sites were likely dispersed throughout the solution, resulting in more opportunities for *de novo* nucleation site formation rather than growth with high stirring speeds. Droplet height was also found to be inversely proportional to particle diameter. In this instance, increased speed of droplets of VP in DMSO interacting with water likely led to a greater dispersion of VP in DMSO eddies in water, resulting, once again, in a process favoring nucleation over particle growth.

Consistent with this interpretation, increased concentration of VP in DMSO resulted in larger particles, likely because equal mixing provided equal opportunity for nucleation initiation but increased local concentrations of VP in antisolvent without greater dispersion favored growth over additional nucleation. In this case, increased concentration of VP in DMSO likely led to incomplete mixing and ultimately increased nanoparticle size [141].

We observed decreased polydispersity with increased depth of water, and broad peaks on DLS with shallow water and both low and high volumes of water. This may be due to the initiation of nucleation processes. It is thought that nucleation can be either homogenous, where particles spontaneously aggregate with their own species, or heterogeneous, where contaminants, even in the cleanest of systems, initiate nucleation [151]. Practically, nucleation of NanoVP is likely due to heterogenous initiation. In the cases of shallow water and low water volume, the walls of the container may also serve as nucleation sites, resulting in less controlled nucleation and aggregation. Conversely, a large volume of antisolvent may disperse monomers too broadly, again resulting in aberrant nucleation and growth.

By combining parameters, we were able to tune NanoVP diameter from 49.0 ± 4.4 nm to 195 ± 7.1 nm, representing a ~64-fold increase in volume, assuming a spherical particle. Interestingly, increasing the value of a single parameter (stirring speed) reduced the diameter of particles from 195 ± 7.1 nm to 63.8 ± 5.0 nm. This is likely due increased dispersion of monomers, resulting in higher nucleation rates and decreased growth rates, particularly because the largest particles were formulated in still water (0 RPM). The largest particles had a broader distribution on TEM, which

was incongruous with a lower Pdi value from DLS. Under all formulation parameters, particles remained amorphous, likely because the mechanisms of nucleation and growth did not significantly change with the parameters studied.

When increasing the diameter of particles, we observed that the Zeta potential decreased. Upon compiling all data regarding diameter and Zeta potential, we found an indirect relationship between diameter and charge. Zeta potential is an inferred charge on the surface of a particle based on the concentration of ions present on the border between the nanoparticle-associated Stern layer and the bulk phase of the liquid. It is possible that the carboxylic acid groups on VP face the aqueous solution in NanoVP, explaining the more negative charge with increased diameter. This is consistent with the finding that NanoVP loses stability in solutions below its pKa, potentially indicating that, when the carboxylic acid is proton-bound, NanoVP loses its negative surface charge and dissociates. It is likely that the same negative surface charges promote stability for over a year. The lack of stability in pHs below 4.5 partially explains the lack of stability in certain media when considering the same model of outwardly facing carboxylic acid groups. Upon freezing, it is possible that water crystals disrupted the structure of NanoVP, resulting in loss of nanoaggregate structure, increased diameter, and increased Pdi.

To reduce this variability, and foreseeing a need for larger volumes of NanoVP samples, we evaluated automated production of NanoVP. Our aim was to increase consistency between samples by automating the pump system. First, we established that pump rate did not impact size, peakedness, Pdi, or Zeta potential for produced NanoVP. We hypothesize that this is because, under all conditions (manual and pump-

produced), droplets of VP in DMSO accumulated on the tip of the needle and pipette, so the introduction to antisolvent was under approximately the same parameters, influenced primarily by acceleration of the droplet by gravity from a constant height above the surface of the water. We compared the diameter, Pdi, and Zeta potential of four automated pump samples at each pump rate and four random handmade samples. We found no significant changes in diameter, Pdi, or Zeta potential, indicating that the pump system is as consistent as our handmade protocol, but not more so, for Condition 2 NanoVP nanoparticles.

2.5 Limitations

It is worth noting that parameters were explored with hand-made samples, and within these samples, we observed from 8% (Condition 3) to 18% (Condition 1) variability in diameter and between 11% (Conditions 3 and 4) and 114% (Condition 1) variability in concentration with samples made by two well-trained experimenters. The batches produced achieved useful concentration, but the overall volume (a maximum of 5.3 mL) can still be improved. What's more, the current production setup is not sterile, and, while no contamination was noted in cell culture or *in vivo*, and samples did not show growth after over a year with refrigeration, further safety testing will be needed before use in larger animals.

It is notable that most measurements revealed a discrepancy between the hydrodynamic diameter measured *via* DLS and the diameter measured *via* TEM. Our initial goal was to formulate a particle small enough to move through a brain tumor based on previous reports of space between cells in brain tumors. Further characterization is needed to understand the cellular-level movement of NanoVP

particles, as it is currently unclear if the hydrodynamic diameter, the diameter measured by TEM, or the diameter considering a potential protein corona is most relevant for movement in biological systems [181-183]. This evaluation may be complicated by the affinity of VP for serum components [172].

2.6 Conclusions

Here, we identified key parameters in the synthesis and stability of NanoVP. We managed a two-fold increase in diameter and six-fold increase in concentration. We found that our largest particles had a significantly more negative charge than our initial formulation. The utility of the varied diameters in biological contexts warrants further evaluation. The -30-mV threshold is typically thought to confer greater stability to particles in solution due to increased interparticle repulsive forces, so future work may compare biological impacts of large, very negative particles compared to smaller, less negatively charged particles. Future work will expand on the scale-up of the pump-made system, as well as other considerations for clinical application of NanoVP, including endotoxin testing.

Chapter 3: Pharmacokinetics and Biodistribution of NanoVP*

3.1 Introduction

VP has been used clinically as a photosensitizer for over twenty years. Visudyne is delivered to the clinic as a lyophilized powder of VP and lipids, then reconstituted by the clinician with sterile water and infused intravenously within four hours. The initial evaluation of the PK of VP in mice looked at delivery in organic solvent without lipids [170] and delivery in a liposome [171] in tumor-bearing mouse models. It was hypothesized that VP redistributed to plasma lipoproteins in serum [184], which are responsible for antitumor efficacy *in vitro* and *in vivo* [185] potentially due to enhanced low-density lipoprotein (LDL)-mediated uptake of VP in tumor cells [186]. Despite these initial promising results, no LDL-VP complexes have been developed. Recent evidence suggests that VP in Visudyne redistributes quite quickly to serum albumin [172], although this study did not evaluate distribution to LDL.

The most extensive clinical evaluation of VP pharmacokinetics after intravenous infusion indicated a dose-dependent C_{max} occurring at the end of infusion, and a biexponential clearance with distribution in the first 1-3 hours and an elimination

* This chapter was adapted from Quinlan JA*, Inglut CT*, Srivastava P, Rahman I, Stabile J, Gaitan B, Arnau del Valle C, Baumiller K, Gaur A, Chiou W-A, Karim B, Connoly N, Robey RW, Woodworth GF, Gottesman MM, and Haung H-C, "Carrier-Free, Amorphous Verteporfin Nanodrug for Enhanced Photodynamic Cancer Therapy and Brain Drug Delivery." *Adv Sci (Weinh).* 2024;11(17):e2302872. doi:10.1002/advs.202302872 and Quinlan JA, Baumiller K, Gaur A, Chiow W-A, Robey RW, Gottesman MM, and Huang H-C, "Optimization of the Synthesis of Self-Assembled Verteporfin Nanoaggregates for Anticancer Therapy Applications." *Submitted*. Permission was obtained from the publisher to use this material in the current dissertation.

half-life of 5-6 hours [187]. This quick clearance has made VP an attractive agent for PDT as skin photosensitivity is resolved within 24-48 hours after infusion [187].

In the context of brain malignancies, it is unclear if VP crosses the BBB to become bioavailable. In a phase 0 study, VP infused before surgical resection was detectable in the tissue after resection [121], although plasma levels were not analyzed to provide details on the degree to which VP entered the tissue. Fluorescent imaging and fluorescent microscopy have indicated that VP may enter the brain [120], although quantitation remains to be done. A current clinical study relies on brain bioavailability of VP for light-independent management of GBM after infusion (NCT04590664), although the ability of the drug to cross the BBB to reach tumor cells is not known.

Light-independent applications of VP will require long-term, high-concentration dosing of the drug [122], likely several times a week considering the short half-life of VP after infusion. One can imagine that light-independent use of VP would occur in patients post-resection who have not yet developed recurrence and therefore are likely not hospitalized, meaning that maintaining quality of life and providing an administration route that is easy to comply with is quite important. Intravenous delivery at home is difficult and likely not preferable for patients. As such, oral delivery of VP is desirable for its new applications; however, the bioavailability of VP after oral administration has not yet been determined. One study has found decreased rates of liver metastases in colon cancer after oral delivery of VP [188], but it is unclear whether VP acted locally or if it was absorbed and bioavailable systemically.

3.2 Methods

3.2.1 NanoVP Formulation

NanoVP was formulated as described in *Chapter 2*, either using Condition 2 or Condition 4 (**Table 2-1**), as specified in individual experiments.

3.2.2 Animal Work Approvals and Technical Details

Animal work was either completed at the University of Maryland, College Park or collaboratively with the lab of Nadejda Tsankova, MD, PhD, at the Icahn School of Medicine at Mount Sinai (ISMMS). Animal work performed at Mount Sinai was performed by Balagopal Pai, PhD, and Thenzing Silva Hurtado, DVM, PhD.

For work done at the University of Maryland, College Park, animal studies were conducted under animal protocols (R-MAR-22-16, R-MAY-20-19, R-MAY-23-27) that were approved by the University of Maryland, College Park Institutional Animal Care and Use Committee, which has been fully accredited by the Association for Assessment and Accreditation of Laboratory Animal Care International (AAALAC) since 2011 with PHS Assurance Number D16-00172 and USDA Certificate Number 51-R-0095. J:Nu nude mice (male or female, as specified in each specific experiment; 4-5 weeks old, #007850, The Jackson Laboratory, Bar Harbor, ME, USA) were used for experimentation. These mice are homozygous *Foxn1*^{nu}/*Foxn1*^{nu} and lack a thymus, preventing T cell maturation. For injections of cells either subcutaneously or orthotopically, or intravenous injection of drug, mice were anesthetized with 2-5% inhaled isoflurane until respiration slowed and toe and tail pinch were negative. The anesthesia was maintained with 2% inhaled isoflurane. Mice were placed on sterile

paper towels on top of a heating pad while anesthetized, and a heating pad was placed under their recovery cage post-procedure. Because mice were immunocompromised, all handling and procedures were completed in a biosafety cabinet using sterile supplies. For all studies, euthanasia was performed *via* CO_2 asphyxiation followed by cervical dislocation.

For animal studies completed at Mount Sinai, animal studies were performed in accordance with the ethical standards of ISMMS under approved Institutional Animal Care and Use Committee protocols. Patient-derived G-16302 (2×10^5) cells were injected stereotactically into the striatum (2 mm right lateral to bregma and 3 mm deep) of 2-month-old male and female mice with B&T-cell immunodeficiency but retained microglia activity (IcrTac:ICR-PrkdcSCID strain, Taconic).

3.2.3 Serial Subcutaneous Passaging of GBM39 Patient-Derived Xenograft Glioblastoma Cells

GBM39 is a flank-passaged PDX model of GBM that expresses luciferase [189]. GBM39 cells were serially passaged in the flank of female J:NU mice. Once tumors reached 1-2 cm on their longest axis, mice were euthanized, and the subcutaneous tumor was removed. Necrotic and connective tissue was removed, then the tumor was minced with a scalpel in a sterile dish. Tumors were fully dissociated using a gentleMACS tumor dissociation kit (Miltenyi Biotec) according to manufacturer protocols, which includes several rounds of mechanical and enzymatic dissociation. Once dissociated, the cell suspension was filtered through a 70 µm then a 40 µm sterile filter. Living cells were counted using propidium iodide and resuspended at the desired concentration in PBS without calcium and magnesium. The cell

suspension was mixed with Matrigel in a 1:1 cell suspension:Matrigel ratio. Up to 200 µL of suspension containing up to $10x10^6$ cells was injected subcutaneously using a 14-18 gauge needle under the skin over the flank. The skin over the flank was wiped with ethanol wipes prior to injection. A sterile cotton swab was applied to the injection site as the needle was removed to prevent backflow.

3.2.4 Subcutaneous Glioblastoma Tumor Inoculation for Experimentation

Subcutaneous tumor injection was performed for PK and a time course BD study. GBM39 cells were prepared as described in *3.2.3*, with an end volume of 100 µL and a total of $1x10^6$ cells per mouse. Cells were injected into a mixed cohort of male and female J:Nu mice. Tumors grew until the average volume was 50 mm^3. Tumor volumes were longitudinally monitored using calipers and calculated using the standard estimation formula, $V=½\times length\times width^2$, where length equals the maximum tumor diameter in millimeters and width equals the diameter that is perpendicular to the length.

3.2.5 Orthotopic Glioblastoma Tumor Inoculation

GBM39 cells were passaged and dissociated as described in *3.2.4*. Female J:Nu mice were affixed to a stereotactic apparatus after isoflurane anesthesia. Ophthalmic ointment was placed over the eyes of the mice. Mice received subcutaneous carprofen (5 mg/kg; 100 µL) immediately before the procedure and the following morning. The skin was cleaned with Betadine, then cleaned with an ethanol wipe. A scalpel was used to create an incision approximately 0.5-1 cm long along the top of the head, revealing the skull. The bregma was identified and the stereotactic apparatus was used to identify

the point 2 mm right lateral to the bregma, where a drill was used to create a hole in the skull. The site was swabbed with a sterile cotton swab dipped in sterile PBS during drilling to reduce heating and to remove blood. Once the hole was drilled, the Hamilton syringe on the stereotactic apparatus was brought in contact with the top of the brain and slowly lowered 3 mm into the brain. After 1 minute, $5x10^5$ GBM39 cells in 5 µL of PBS without calcium and magnesium were injected at a manual rate of 1 µL per minute (e.g., one minute between each 1 µL push), and the site was observed for backflow. In the event of backflow, the backflow was swabbed using a sterile cotton swab to prevent tumor seeding, and the injections were paused for 2 minutes before the next push. After the injection was complete, the needle was left in place for two minutes before being slowly removed. The site was swabbed with a sterile cotton swab dipped in sterile PBS, then the incision was closed with a Visorb polyglycolic acid suture and veterinary glue. Mice were then removed from the stereotactic device and observed until toe and tail pinch were restored, at which point they were moved to a recovery cage and provided with hydrogel water and high-caloric density wet food.

3.2.6 *In vivo* Live Imaging to Approximate Orthotopic Tumor Burden

GBM39 cells express luciferase, and an IVIS Spectrum (PerkinElmer) was used to capture bioluminescent signal as a proxy for tumor burden. Mice received 150 mg/kg intraperitoneal injection of luciferin (Promega VivoGlo) ten minutes before imaging, then were anesthetized. Anesthetized mice were placed inside a sealed, sterile box affixed to high efficiency particulate air (HEPA) filters with looping tubing, which was removed from the biosafety cabinet, transported to the IVIS machine (PerkinElmer), and reaffixed to flowing oxygen and isoflurane for imaging. Mice were imaged for

bioluminescence. LivingImage software was used to measure bioluminescent signal as total flux (photons/second) within regions of interest that encompassed the head of the mouse.

3.2.7 High-Performance Liquid Chromatography/Tandem Mass Spectrometry

A High-Performance Liquid Chromatography/Tandem Mass Spectrometry (HPLC/MS-MS) protocol was developed to quantify VP levels in various media. A Waters H-Class Ultra-Performance Liquid Chromatography (UPLC)/Xevo Tandem Quadrupole (TQD) mass spectrometer was used for quantification of VP in both serum and tissues. Samples and standards were analyzed using an ACQUITY UPLC Ethylene Bridged Hybrid (BEH) reversed phase C18 column (130Å, 1.7 µm, 2.1 mm x 50 mm, Waters). At a flow rate of 0.4 mL/min, liquid chromatography was performed where A was water with 0.1% formic acid and B was ACN with 0.1% formic acid: 20% A from 0-1 minutes; 20% A to 0% A from 1-3.2 minutes; 0% A to 20% A from 3.2-3.3 minutes; 20% A from 3.3 to 3.5 minutes. VP eluted in two peaks at ~3.02 minutes and ~3.11 minutes. Daughter ions detected were 645.45, 513.37, and 499.93 m/z; the 513.37 ion was used for quantitation. TargetLynx software with curve smoothing was used to quantify the area under the curve.

3.2.8 Time course Pharmacokinetics and Biodistribution

For time course PK and BD, NanoVP formulated under Condition 2 (**Table 2-1**) was used. Mice bearing flank tumors with an average volume of 100 mm^3 received 0.5 mg/kg tail vein injections of NanoVP. After euthanasia at 0.05, 0.25, 1, 3, 6, 24, or 72 hours post-injection, blood was collected in lithium heparin tubes (Sarstedt, Inc.)

and centrifuged at 2000xg. Serum was mixed 1:10 with HPLC-grade ACN, stored at -80ºC for 1 hour, then centrifuged again at 10,000 rpm for 20 minutes at 4°C. Supernatants were collected for HPLC/MS-MS analysis. Tissues were stored at -80°C until processed. Tissues were homogenized with a BeadBug 6 (Benchmark Scientific), and 2.0 mL tubes prefilled with 3.0 mm zirconium homogenizer beads (Stellar Scientific). Tissues were mixed 1:3 w/w with HPLC-grade water (Sigma Aldrich) for homogenization, then mixed 1:8:1 sample:ACN:MeOH v/v. Samples were stored at -80°C for at least 30 minutes before centrifugation at 21.1xg for 20 minutes. Supernatants were transferred to centrifugal polytetrafluoroethylene filters (MilliporeSigma), centrifuged according to manufacturer protocol, and then transferred to HPLC tubes (Waters).

3.2.9 Biodistribution and Brain Penetration

Animal work for biodistribution studies comparing VP in DMSO and NanoVP, as well as oral versus intraperitoneal injection, were performed by Balagopal Pai, PhD, and Thenzing Silva Hurtado, DVM, PhD in the lab of Nadejda Tsankova, MD, PhD, at Icahn School of Medicine at Mount Sinai. For these studies, Condition 4 NanoVP (**Table 2-1**) was used. Four weeks after tumor inoculation, mice received either IP administration of VP in DMSO (50 mg/kg or 500 mg/kg), IP administration of NanoVP (5 mg/kg), or *per os* (PO) oral gavage of NanoVP (10 mg/kg). After euthanasia, tissues were stored at -80°C before HPLC-MS/MS. In some experiments, mice were perfused with saline, and plasma was collected before storage at -80°C for HPLC-MS/MS as described in *3.2.7*. Perfusion was performed to evaluate the concentration of VP in the tissue compared to the concentration in the blood.

For brain penetration studies, animal work was conducted at the University of Maryland, College Park. Mice injected with GBM39 as described in *3.2.5* and monitored until near endpoint as determined by a score sheet that incorporated weight loss and coordination. Mice then received IP NanoVP at 0, 5, 10, or 25 mg/kg. For this study, Condition 4 NanoVP (**Table 2-1**) was used. Two hours later, serum and brain hemispheres were collected and processed as in *3.2.8,* and VP levels were quantified by HPLC/MS-MS as in *3.2.7*.

3.2.10 Statistics

Statistical tests were carried out using GraphPad Prism (GraphPad Software, San Diego, CA, USA) or Microsoft Excel (Microsoft, Redmond, WA, USA). For brain biodistribution, K_p is shown, which is the concentration of VP in the brain divided by the concentration of VP in the plasma. Two-tailed Student's t-tests were used to compare the tumor-bearing and non-tumor bearing values within each treatment group. Each mouse's tumor-bearing and non-tumor-bearing values are connected by a black line.

3.3 Results

3.3.1 Development of a Liquid Chromatography-Tandem Mass Spectrometry Method for Verteporfin Quantitation in Tissues

VP concentration can be estimated *via* fluorescence [190] or absorbance, but both light-dependent methods of concentration measurement are limited by the depth that the light can penetrate as well as the relatively high concentration of VP needed for quantification. They are not particularly amenable to quantification of drug levels

in biological systems. As a result, I developed an HPLC-MS/MS protocol to quantify VP in tissue based on previously reported methods [112]. Daughter ions were detected at 645.45, 513.37, and 499.93 m/z. Liquid chromatography was optimized to elute VP at ~3.02 and ~3.11 minutes (**Figure 3-1**). The signal:noise ratio was approximately 2:1 at 50 ng/mL and increased as concentration of VP increased. The signal magnitude was appropriate in the range of interest (~10 ng/mL to ~1000 ng/mL) ranging from 10^4 to 10^6. The two peaks are likely due to elution of two isomers of VP. The more hydrophobic of the two isomers, which has an outward-facing methyl group where the other isomer has an outward-facing hydroxyl group, likely elutes second due to its greater affinity to the liquid chromatography column.

The area under the curve response was linear with a positive slope and an $R^2 = 0.9983$ on a sample standard curve (**Figure 3-2**). Signal was consistently detected down to 5 ng/mL, and signal was linearly quantifiable to 10-20 ng/mL depending on the run.

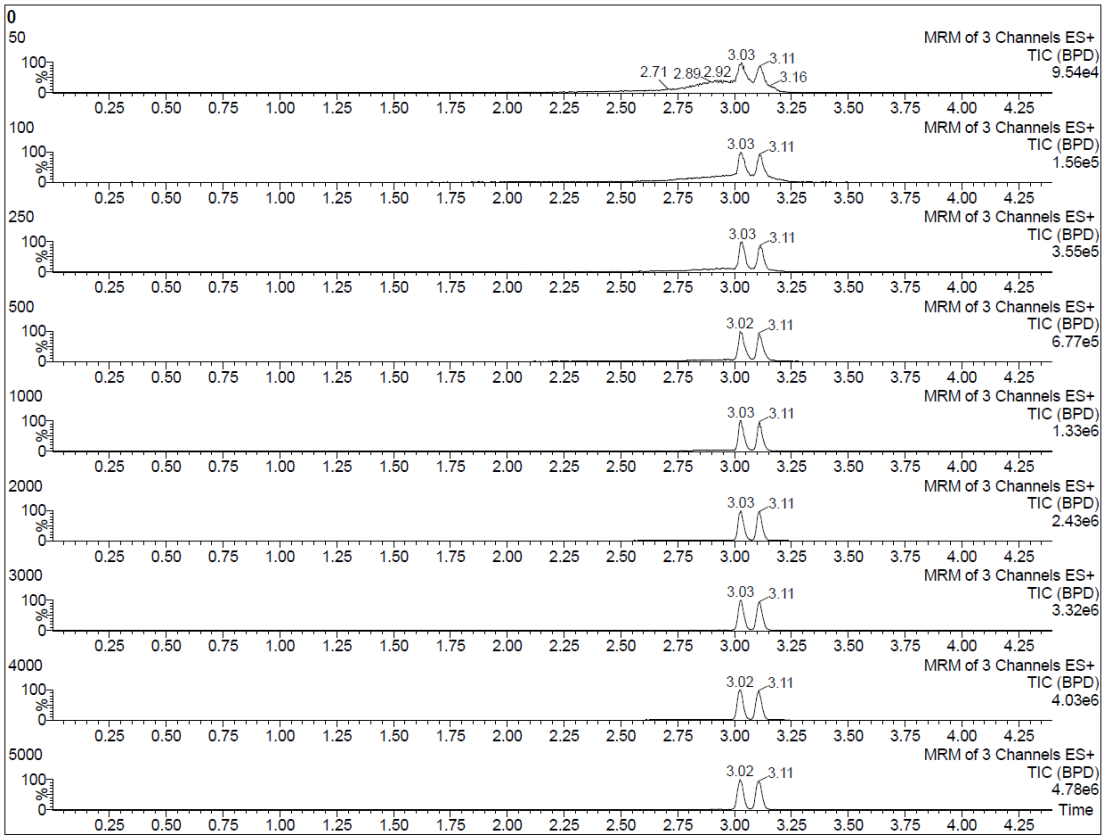

Figure 3-1. Sample multiple reaction monitoring chromatogram for VP. Sample chromatogram for a standard curve (concentration on left hand side, ranging from 50 to 8000 ng/mL of VP) showing the multiple reaction monitoring (MRM) for daughter ions at 645.45, 513.37, and 499.93 m/z. Note increased relative values (right hand side, ranging from 9.54×10^4 to 4.78×10^6 with peak elution times of ~3.02 and 3.11 minutes for VP.

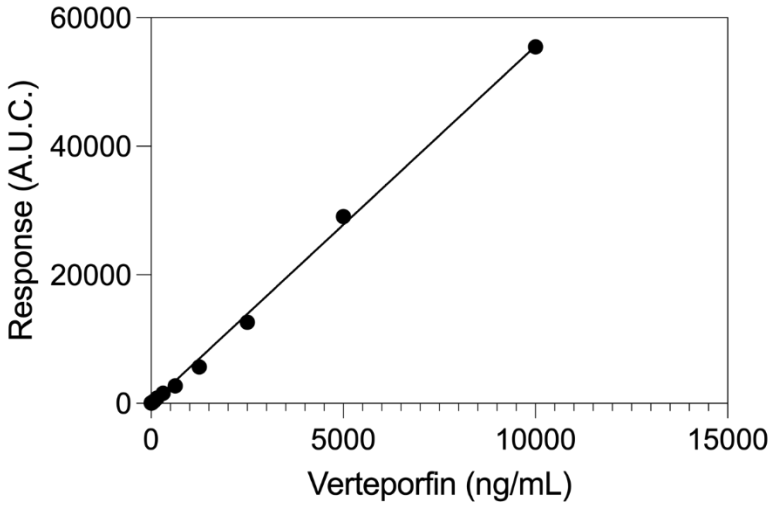

Figure 3-2. Representative liquid chromatography-tandem mass spectroscopy standard curve for verteporfin. Graph shows known VP concentration as measured by absorbance versus area under the curve (AUC) measured from HPLC-MS/MS chromatograms. By nonlinear fit to y=mx with forced intercept at (0,0), m = 5.560 and $R^2 = 0.9983$.

3.3.2 Pharmacokinetics of NanoVP

Pharmacokinetics of NanoVP were determined after intravenous injection, reflecting the typical delivery route in the clinic and in preclinical models for PDT. C_{max}, or the highest concentration in the blood, was observed immediately after injection, then distribution was observed by 15 minutes and clearance was observed by 24 hours. There was no detectable VP in the serum of injected mice after 72 hours (**Figure 3-3**). The observed pharmacokinetics were like historically reported pharmacokinetic values of VP in DMSO and liposomal VP (**Table 3-1**) [170, 191], with the notable difference that the second clearance half-life may be extended for NanoVP, potentially indicating longer stability in the serum.

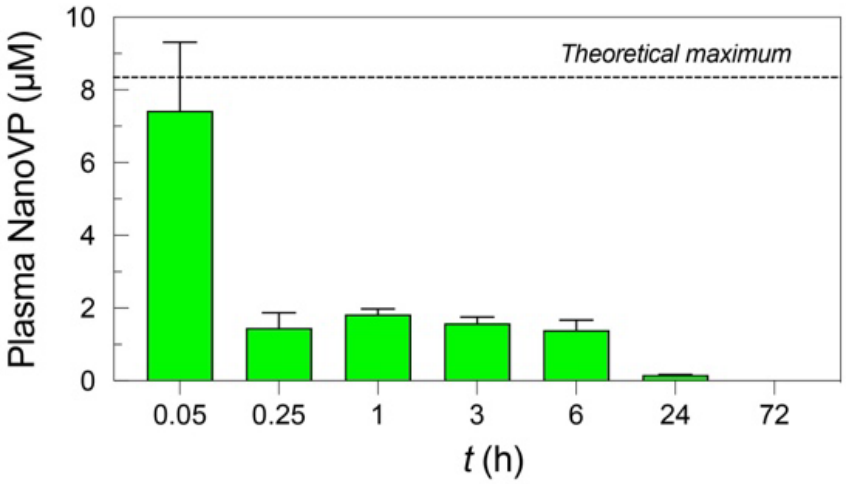

Figure 3-3. Pharmacokinetics of NanoVP after 0.5 mg/kg intravenous administration in mice. NanoVP PK was evaluated in mice. Animals received 0.5 mg/kg NanoVP *via* tail vein injection. We observed an initial spike in <5 minutes, followed by a plateau in plasma levels from 15 minutes post-injection to 6 hours post-injection. Complete clearance was observed at 72 hours. Data shows mean + SEM, n≥3 in all groups.[*]

[*] This figure was first published in Quinlan JA*, Inglut CT*, Srivastava P, Rahman I, Stabile J, Gaitan B, Arnau del Valle C, Baumiller K, Gaur A, Chiou W-A, Karim B, Connoly N, Robey RW, Woodworth GF, Gottesman MM, and Haung H-C, "Carrier-Free, Amorphous Verteporfin Nanodrug for Enhanced Photodynamic Cancer Therapy and Brain Drug Delivery." *Adv Sci (Weinh).* 2024;11(17):e2302872. doi:10.1002/advs.202302872

Table 3-1. Reported pharmacokinetics of verteporfin formulations. NanoVP exhibits biphasic clearance, with initial clearance within 15 minutes and secondary clearance within approximately 15 hours. Liposomal VP and VP in DMSO have initial clearance within the first 30 minutes.

	Initial $t_{1/2}$	**Second $t_{1/2}$**	**Clearance**
NanoVP	~10 mins	~15 h	24 h
VP in DMSO [170]	10-30 mins	~8 h	24 h
Liposomal VP [191]	<30 mins	~6 h	24 h

3.3.3 Biodistribution of NanoVP

Organs were collected from mice after the PK study. The mice had flank GBM39 tumors and undisrupted BBBs. Mice received a single IV infusion of 0.5 mg/kg NanoVP. Quantification revealed persistently high levels in highly vascularized tissues (e.g. heart, lung, kidneys, liver, spleen), and tumor-to-normal tissue (skin) ratios of 0.3-1.8 around the time of intended treatment (1-3 hours post-injection) (**Figure 3-4, Table 3-2**). Clearance was observed by 72 hours, consistent with PK data. Moderate intratumoral accumulation was observed, as anticipated with a non-targeted nanoparticle. Interestingly, the brain-to-skin ratios around the intended time to treat (1-3 hours post-injection) were 0.1-8.4, indicating potentially high bioavailability in the brain.

We also evaluated biodistribution after long-term dosing *via* IP injection. Starting four weeks after tumor inoculation, mice bearing orthotopic G16302 tumors received IP injections of VP in DMSO (50 mg/kg/day) daily for two weeks, and a final IP dose two hours before euthanasia. HPLC/MS-MS indicated high levels in abdominal tissues (**Figure 3-5**) likely due to direct absorption, and relatively high levels in the kidneys, likely due to direct absorption or relatively high blood levels. In non-abdominal tissues, levels were the highest in highly vascularized tissues like the heart and lung, and lowest in light-sensitive tissues like the eye and ear (**Figure 3-6**). For brain biodistribution, a third group receiving 5 mg/kg NanoVP *via* IP injection for the same timeline was added. Similar levels of VP accumulation were observed in both the tumor-bearing and non-tumor bearing hemispheres despite five times greater doses of IP injected VP. There was greater variability in the hemispheres of NanoVP-injected

mice. There was more accumulation in the cerebellum of VP-injected mice than NanoVP-injected mice (**Figure 3-7**).

New applications of VP would benefit from oral delivery of the drug to enhance patient compliance. To evaluate oral bioavailability, mice were inoculated with orthotopic G16302 tumors. Four weeks after inoculation, mice received IP NanoVP (5 mg/kg) or PO NanoVP (10 mg/kg). Dosing was limited by volumes of delivery for each respective route and the achievable concentration of NanoVP produced. Administration was performed daily for two weeks, with final administration two hours before euthanasia. Plasma levels were comparable for the IP and PO treated mice despite the difference in dosing (**Figure 3-8**). More VP was observed in the liver of PO treated mice, likely because intestinally absorbed material first passes through the liver, and VP is cleared in the bile without chemical modifications. VP may have been undetectable in brain tissues because mice were perfused before tissues were quantified, and the amount of VP in the brain tissues may have been below the limits of detection for the HPLC/MS-MS method used here.

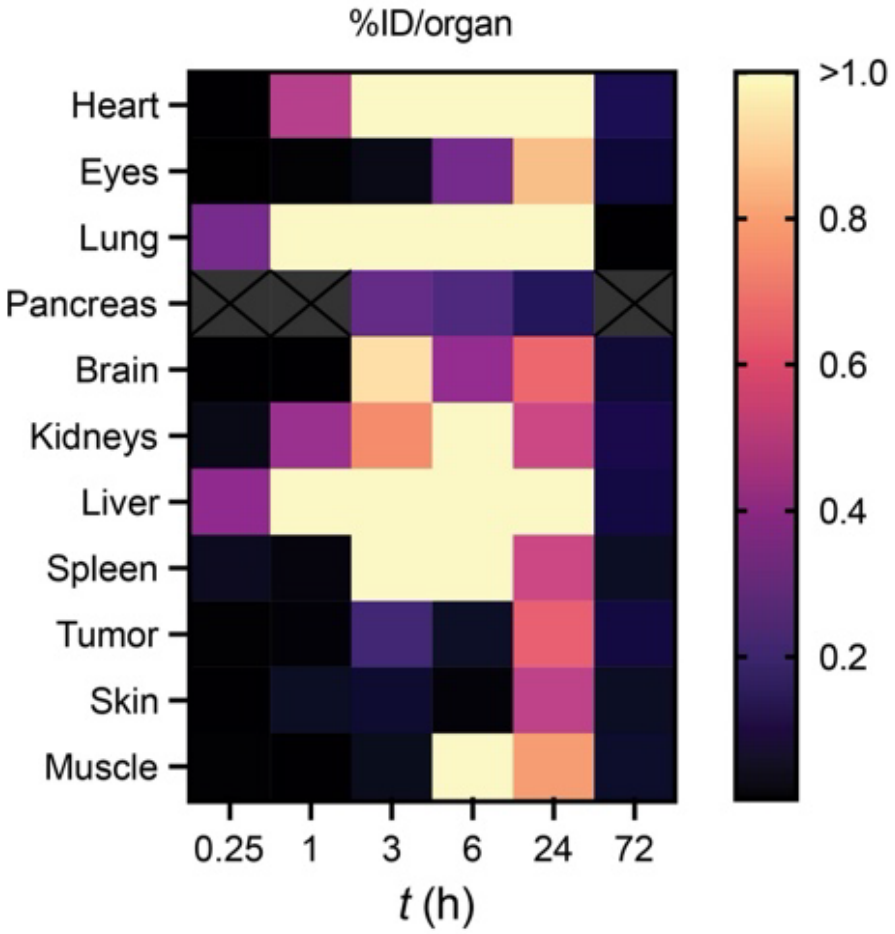

Figure 3-4. NanoVP biodistribution after intravenous injection in mice bearing flank GBM39 tumors as measured *via* HPLC-MS/MS. Data expressed as percent injected dose per organ (%ID/organ). Grey boxes with an "X" indicate no data.[*]

[*] This figure was first published in Quinlan JA*, Inglut CT*, Srivastava P, Rahman I, Stabile J, Gaitan B, Arnau del Valle C, Baumiller K, Gaur A, Chiou W-A, Karim B, Connoly N, Robey RW, Woodworth GF, Gottesman MM, and Haung H-C, "Carrier-Free, Amorphous Verteporfin Nanodrug for Enhanced Photodynamic Cancer Therapy and Brain Drug Delivery." *Adv Sci (Weinh).* 2024;11(17):e2302872. doi:10.1002/advs.202302872

Table 3-2. Quantified biodistribution of NanoVP after intravenous injection in mice bearing flank GBM39 tumors. Mice received IV injection of NanoVP (0.5 mg/kg), and tissues were homogenized before quantification of VP in each tissue by HPLC-MS/MS. Values shown are percent injected dose per organ (%ID/organ) ± SEM.[*]

	0.25 h	**1 h**	**3 h**	**6 h**	**24 h**	**72 h**
Heart	0.01 ± 0.01	0.47 ± 0.33	3.65 ± 2.10	16.9 ± 7.43	2.07 ± 0.83	0.14 ± 0.08
Eyes	0.00 ± 0.00	0.03 ± 0.02	0.06 ± 0.02	0.31 ± 0.11	0.84 ± 0.34	0.12 ± 0.06
Lung	0.31 ± 0.25	14.7 ± 12.1	21.8 ± 12.2	15.6 ± 7.71	1.91 ± 1.15	0.00 ± 0.00
Pancreas	N.D.	N.D.	0.27 ± 0.12	0.22 ± 0.11	0.15 ± 0.08	N.D.
Brain	0.01 ± 0.00	0.01 ± 0.00	0.92 ± 0.48	0.38 ± 0.21	0.64 ± 0.27	0.12 ± 0.06
Kidneys	0.07 ± 0.04	0.40 ± 0.20	0.73 ± 0.19	35.5 ± 25.5	0.52 ± 0.14	0.14 ± 0.07
Liver	0.37 ± 0.21	71.0 ± 39.8	3.36 ± 0.92	4.34 ± 2.58	2.66 ± 1.37	0.13 ± 0.07
Spleen	0.09 ± 0.05	0.04 ± 0.02	5.44 ± 2.04	11.0 ± 6.09	0.53 ± 0.13	0.09 ± 0.05
Tumor	0.02 ± 0.01	0.03 ± 0.02	0.20 ± 0.06	0.10 ± 0.05	0.62 ± 0.16	0.13 ± 0.07
Skin	0.01 ± 0.01	0.09 ± 0.07	0.11 ± 0.04	0.03 ± 0.01	0.49 ± 0.17	0.09 ± 0.06
Muscle	0.02 ± 0.01	0.01 ± 0.01	0.08 ± 0.02	3.23 ± 1.85	0.77 ± 0.30	0.11 ± 0.06

[*] This table was first published in Quinlan JA*, Inglut CT*, Srivastava P, Rahman I, Stabile J, Gaitan B, Arnau del Valle C, Baumiller K, Gaur A, Chiou W-A, Karim B, Connoly N, Robey RW, Woodworth GF, Gottesman MM, and Haung H-C, "Carrier-Free, Amorphous Verteporfin Nanodrug for Enhanced Photodynamic Cancer Therapy and Brain Drug Delivery." *Adv Sci (Weinh).* 2024;11(17):e2302872. doi:10.1002/advs.202302872

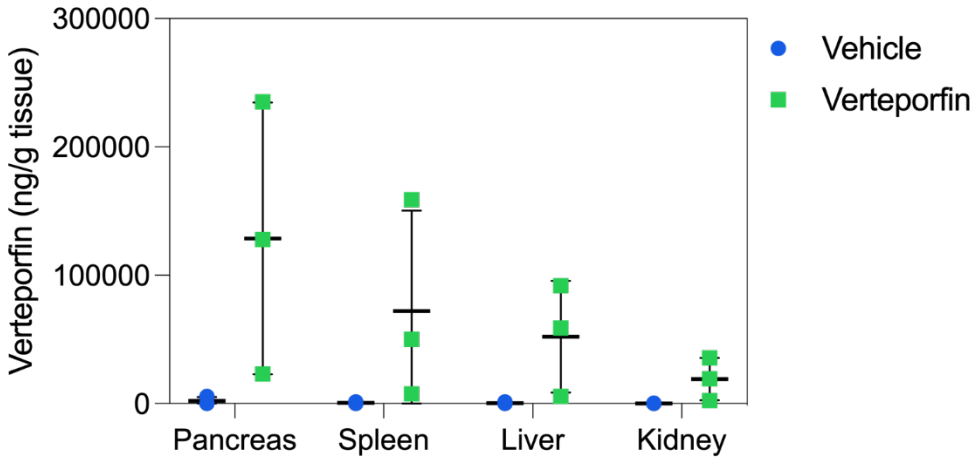

Figure 3-5. Biodistribution of verteporfin in abdominal organs after intraperitoneal injection. VP (50 mg/kg in DMSO) was injected daily into the peritoneal cavity of female ICRSC bred mice bearing G16302 orthotopic patient-derived tumors. Starting 4 weeks after tumor implantation, mice were dosed with VP daily for 2 weeks, and received a final dose 2 hours before euthanasia. Tumors were homogenized and VP levels were measured *via* HPLC/MS-MS. Central bar shows mean ± SD; individual points represent values from individual animals.

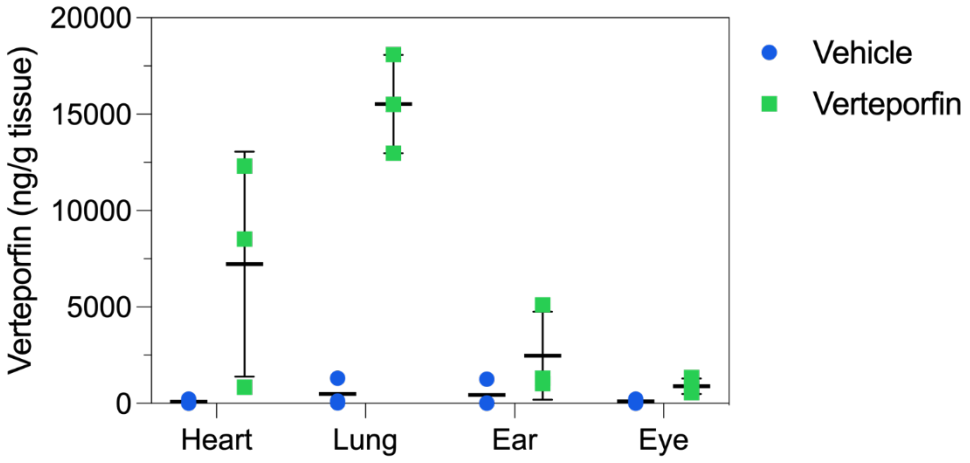

Figure 3-6. Biodistribution of verteporfin in non-abdominal organs after intraperitoneal injection. VP (50 mg/kg in DMSO) was injected daily into the peritoneal cavity of female ICRSC bred mice bearing G16302 orthotopic patient-derived tumors. Starting 4 weeks after tumor implantation, mice were dosed with VP daily for 2 weeks, and received a final dose 2 hours before euthanasia. Tumors were homogenized and VP levels were measured *via* HPLC/MS-MS. Central bar shows mean ± SD; individual points represent values from individual animals.

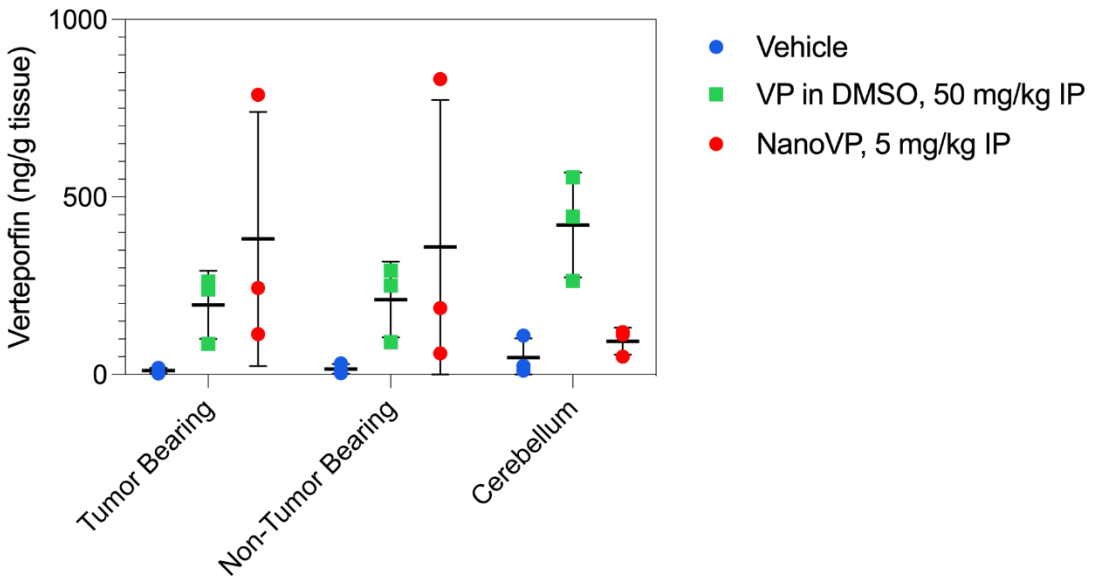

Figure 3-7. Biodistribution of verteporfin in the brain after intraperitoneal injection. VP (50 mg/kg in DMSO or 5 mg/kg NanoVP) was injected daily into the peritoneal cavity of female ICRSC bred mice bearing G16302 orthotopic patient-derived tumors. Starting 4 weeks after tumor implantation, mice were dosed with VP daily for 2 weeks, and received a final dose 2 hours before euthanasia. Tumors were homogenized and VP levels were measured *via* HPLC/MS-MS. Central bar shows mean ± SD; individual points represent values from individual animals.

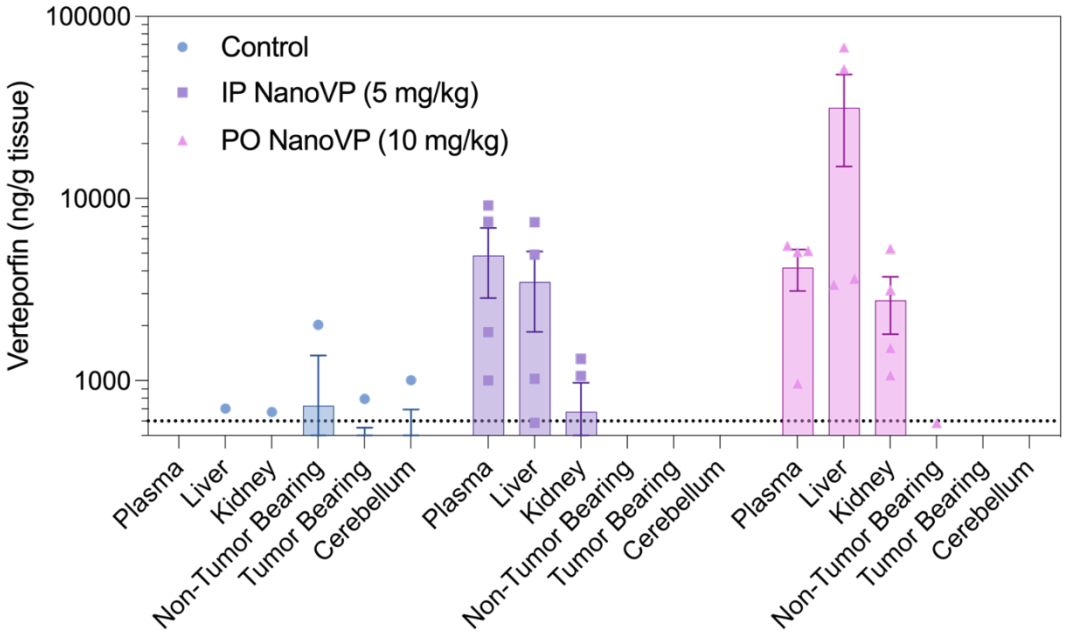

Figure 3-8. Bioavailability of NanoVP after intraperitoneal or oral delivery. NanoVP was administered *via* intraperitoneal injection (IP, 5 mg/kg) or by oral gavage (PO, 10 mg/kg) daily to female ICRSC bred mice bearing G16302 orthotopic patient-derived tumors. Starting 4 weeks after tumor implantation, mice were dosed with NanoVP daily for 2 weeks, and received a final dose 2 hours before euthanasia. Serum was collected and mice were perfused with saline. Tissues were homogenized and VP levels were measured *via* HPLC/MS-MS. Bars show mean ± SEM. Individual points represent values from individual animals. Dotted line indicates limit of quantitation at 600 ng/mL.

3.3.4 Bioavailability of NanoVP in the Brain

VP has recently returned to experimental clinical use for its potential to manage cancer, particularly GBM, in a light-independent manner [122]. As such, we evaluated both the bioavailability and activity of NanoVP in the context of GBM. First, mice with near-endpoint orthotopic GBM39 tumors received 5, 10, or 25 mg/kg *via* IP injection (**Figure 3-9A**). Two hours post-injection, the mice were euthanized before plasma and both brain hemispheres were collected. VP levels were quantified *via* HPLC-MS/MS. At this point, tumors were quite large and right-sided (**Figure 3-9B**). After quantification, the levels of VP in the plasma and hemispheres were summarized as K_p, which is the ratio between brain concentrations and plasma concentrations of the drug [192]. The ratios were similar among all injected doses, with a higher ratio in the tumor-bearing hemisphere (**Figure 3-9C**). Raw serum and brain values are provided in **Table 3-3**.

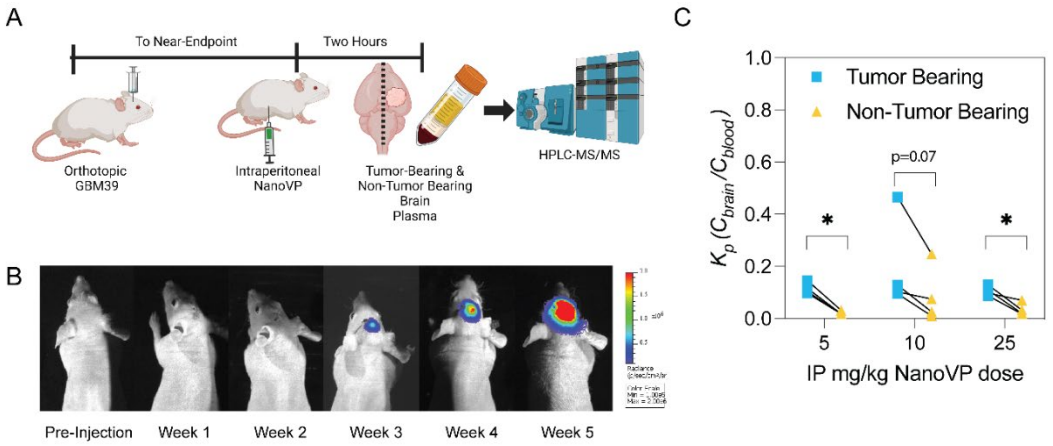

Figure 3-9. Bioavailability of NanoVP in the context of glioblastoma. (A) To evaluate bioavailability of NanoVP, mice bearing near-endpoint orthotopic GBM39 tumors received 5, 10, or 25 mg/kg intraperitoneal (IP) injections of NanoVP. Two hours later, mice were euthanized, and brains and plasma were collected for HPLC-MS/MS analysis. (B) IVIS images demonstrate relative size and sidedness of the GBM39 tumors over time. (C) The K_p value, or the concentration of VP in each hemisphere of the brain divided by the plasma concentration, reveals higher accumulation of VP in the tumor-bearing hemisphere compared to the non-tumor-bearing hemisphere.[*]

[*] This figure was first published in Quinlan JA, Baumiller K, Gaur A, Chiow W-A, Robey RW, Gottesman MM, and Huang H-C, "Self-Assembled Verteporfin Nanoparticles for Photodynamic and Light-Independent Therapy in Glioblastoma." *Adv NanoBiomed Res.* 2024;2400098. doi: 10.1002/anbr.202400098.

Table 3-3. Verteporfin levels (μg/mL) in the serum and tumor-bearing brain of mice with large, orthotopic GBM39 tumors in the right hemisphere two hours after intraperitoneal administration of NanoVP (0-25 mg/kg) as determined by HPLC-MS/MS. ^^ indicates below the quantifiable limit of detection.*

mg/kg NanoVP Dose, IP	Serum	Tumor-Bearing Hemisphere	Non-Tumor-Bearing Hemisphere
0	^^	^^	^^
5	3.0 ± 1.1	0.88 ± 0.25	0.13 ± 0.031
10	2.7 ± 1.1	0.71 ± 0.52	0.15 ± 0.15
25	5.6 ± 1.3	1.5 ± 0.36	0.33 ± 0.18

*This table was first published in Quinlan JA, Baumiller K, Gaur A, Chiow W-A, Robey RW, Gottesman MM, and Huang H-C, "Self-Assembled Verteporfin Nanoparticles for Photodynamic and Light-Independent Therapy in Glioblastoma." *Adv NanoBiomed Res.* 2024;2400098. doi: 10.1002/anbr.202400098.

3.3.5 Behavior of NanoVP in Serum

The behavior of nanodrugs in biological systems can vary greatly. Some may remain stable on the order of weeks to months, while others may dissociate nearly instantaneously. Through TEM, we probed interactions between NanoVP and human serum. Compared to PBS (0% human serum) (**Figure 3-10A**), the size of NanoVP as measured from TEM images using ImageJ remains intact after 2 hours of 1% human serum incubation (**Figure 3-10B)**, and a protein corona may form around the NanoVP. In contrast, NanoVP in 10% human serum has a 49% decrease in diameter in the same time, but evidence of particles is still visible *via* TEM (**Figure 3-10C, 3-10D**).

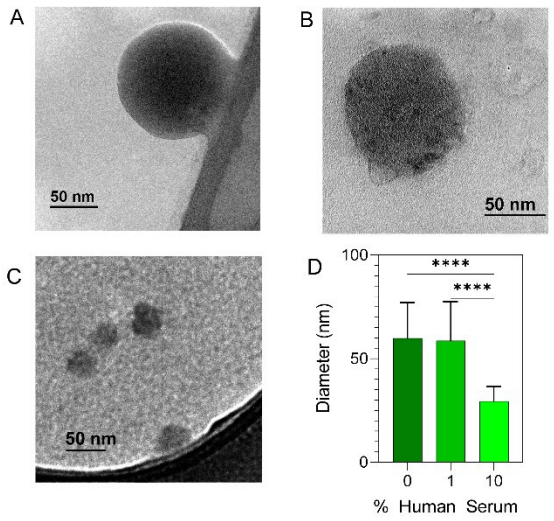

Figure 3-10. NanoVP dissociation in human serum. (A) TEM images of NanoVP in 0% human serum, (B) 1% human serum, and (C) 10% human serum. (D) The size of NanoVP in 0-10% human serum as quantified from TEM images using ImageJ. One-way ANOVA with Tukey's multiple comparison test was used to calculate significant differences, where * $P < 0.05$, ** $P < 0.01$, *** $P < 0.001$. $n \geq 3$. The error bars show the SEM.[*]

[*] This figure was first published in Quinlan JA*, Inglut CT*, Srivastava P, Rahman I, Stabile J, Gaitan B, Arnau del Valle C, Baumiller K, Gaur A, Chiou W-A, Karim B, Connoly N, Robey RW, Woodworth GF, Gottesman MM, and Haung H-C, "Carrier-Free, Amorphous Verteporfin Nanodrug for Enhanced Photodynamic Cancer Therapy and Brain Drug Delivery." *Adv Sci (Weinh).* 2024;11(17):e2302872. doi:10.1002/advs.202302872.

3.4 Discussion

The HPLC/MS-MS method developed here provides an initial method to quantify VP levels in tissues. Through this method, we found that NanoVP's pharmacokinetics are quite like those of other commonly used formulations of VP in mice. Similarly, the biodistribution was relatively nonspecific, and indicates that a large portion of injected NanoVP remains in the blood before clearance or in highly vascularized organs. This is to be expected with an untargeted nanoparticle.

In this study, biodistribution studies were performed with IP, PO, and IV delivery of NanoVP. This was largely dictated by limitations on infusible volumes for each compartment. In the mice used in this study, which generally weight 20-25 grams, IV injection volumes are generally limited to <0.2 mL, IP injection volumes are generally limited to <1.0 mL, and PO delivery is generally limited to <0.2 mL [193]. These limitations make it such that the concentrations achieved in Chapter 2 were still too low for preferred clinical routes of delivery (IV or PO) for all dosing situations, although they do make it feasible for IV delivery in larger mammals like dogs and humans at desirable doses. In this study, initial PK and BD were evaluated at 0.5 mg/kg after IV delivery because this is similar to the dosing and delivery route for PDT with NanoVP in the clinic. IP delivery was performed in order to achieve doses required for light-independent effects, as most literature, to date, has used IP dosing for light-independent applications of VP [120]. Others have used intrathecal delivery in mice and IV delivery in humans [121]. PO delivery was explored here because VP must be delivered at high concentrations over long period of time for light-independent applications, and orally available VP may improve patient compliance.

NanoVP injected IP appears to penetrate the brain at least as well as, if not better than, IP-injected VP delivered in DMSO. Additionally, good plasma availability of PO NanoVP is promising considering the new light-independent applications of the blood. The ability of NanoVP to be absorbed through the gut was not previously known.

We utilized an *in vitro* flank-passaged patient-derived orthotopic xenograft of GBM, GBM39 [189], to evaluate bioavailability of VP in the brain after large-dose intraperitoneal administration of NanoVP. VP doses in the 5-100 mg/kg range in mice have been used to observe anti-cancer light-independent effects of the drug [120, 121]. We waited until near-endpoint to dose mice with intraperitoneal NanoVP in an attempt to recapitulate a potentially leaky BBB in the tumor-bearing hemisphere, but to also be able to quantify VP penetration in the non-tumor bearing hemisphere, which presumably should have an intact BBB [67]. We reported K_p, a ratio of total brain concentration to total plasma concentration. This measure provides a high-level overview of the impact of drug protein binding in the blood, drug binding to brain cells and proteins, and transport (both active and passive) across the BBB [192]. The difference in K_p between the tumor-bearing and non-tumor bearing hemisphere indicates a difference in one of these processes, most likely in either drug binding to brain cells and proteins or transport across the BBB as binding to plasma proteins should be consistent between hemispheres within the same mouse.

Drugs that cross the BBB generally have a molecular weight less than 500 Da, are lipophilic but not so much so that partitioning into the aqueous brain stroma is prohibited, and are not actively effluxed from the brain stroma to the blood the brain [139]. VP has a molecular weight of 718.8 Da, is lipophilic, and is a substrate of ABC

transporters at the BBB [113, 132], meaning that it is unlikely that the drug crosses an intact BBB. Generally, a drug with a $K_p < 0.3$ is considered to be poorly bioavailable in the brain [194]. In this study, we found K_p values in both the tumor-bearing and non-tumor-bearing hemispheres below 0.3 in all mice but one. Consistent with theory, it appears that VP poorly enters the central nervous system. Still, enough enters the brain to see efficacy in mice [120] and measurable levels in humans [121]. In this study, intraperitoneal injection was selected due to limitations on bolus injectable intravenous volume. The similarity in concentrations between doses may be attributable to saturation of absorption and transportation from the peritoneal cavity to the blood and ultimately to the brain.

Still, we observed an increase in K_p in the tumor-bearing hemisphere compared to the non-tumor bearing hemisphere in the 5 mg/kg (5.7-fold increase in K_p, p=0.001), 10 mg/kg (4.6-fold increase, p=0.07), and 25 mg/kg (4.0-fold, p=0.02) treatment groups. This may be attributable to the disruption of brain tissue from the injection of tumor cells to the tumor's impact on the vasculature, or to the interaction between VP and tumor cells. The large tumor used in this study may exhibit enhanced permeability and retention, where irregular neovascularization, elevated inflammatory cytokines, and poor lymphatic drainage may lead to enhanced accumulation of VP at the tumor site [195]. In the context of GBM, this blood-tumor barrier (BTB) has unique properties distinct from the BBB [196] and may explain the observed increase in VP in the tumor-bearing hemisphere. There is also a possibility that the increased accumulation in the tumor-bearing hemisphere is attributable to improved accumulation within tumor cells. Previous work has shown that VP in the blood interacts with various blood

biomolecules, which may have preferential uptake by tumor cells [184]. While this uptake may not translate directly, factoring in the additional absorption from the peritoneal cavity to the blood, considering the partitioning of VP in the blood as a potential driver of accumulation within the tumor-bearing hemisphere may be worthwhile.

Finally, we found that NanoVP mixed with serum dissociates in a time- and concentration-dependent manner. This informs PDT strategy, as VP is likely bioavailable for light activation soon after infusion. This may also be favorable for intracellular accumulation as NanoVP dissociated into monomers can passively diffusion through the cell membrane [115, 197], while liposomes must be endocytosed [198].

3.5 Limitations

The HPLC/MS-MS method developed here is useful in providing some information about biodistribution and pharmacokinetics, but it does have certain limitations. While the response is good and detection is reasonable, extraction of VP from tissues requires several steps of dilution. As such, a more sensitive method is desirable, likely requiring a more sensitive mass spectrometer. Secondly, the current method does not incorporate an internal control, which accounts for drift in the mass spectrometer's signal over time as samples are run. For more definitive values, an internal control is required both as a positive control and to help normalize data.

The pharmacokinetics studies give a good understanding of NanoVP's pharmacokinetics. Further studies are required to understand pharmacokinetics after

oral delivery. For biodistribution, the main item of interest with regards to this thesis is brain penetrance of the drug. K_p is a widely reported but ultimately crude measure of BBB penetration as it does not evaluate the concentration of drug at useful sites. Further investigation into the brain-to-unbound plasma partition coefficient ($K_{p,u}$) and unbound brain-to-plasma partition coefficient ($K_{p,uu,brain}$) which gives a more direct measure of how the passive and active components of the BBB limit drug perfusion into the brain [192, 194].

The models used here to understand brain penetration in the context of a tumor are also useful but not ideal. The process of drilling a hole and then injecting cells disrupts the BBB [199]. Because the true extent of BBB disruption in GBM is unclear [67], and because the invasive cells that drive recurrence reside behind an intact BBB, perhaps a non-tumor bearing brain is the best model to evaluate the potential for NanoVP to enter the brain. Additionally, in this study, the hemisphere of the brain that had a tumor was approximately half tumor and half normal tissue. Should the BBB be corrupted within the tumor but normal in the healthy brain, homogenization and analysis of both the tumor and the healthy tissue would underestimate the K_p value within a tumor. It may be helpful to dissect out the tumor from the rest of the healthy brain, or to use fluorescent imaging of histological slides to visualize where in the brain relative to the tumor NanoVP penetrates.

Finally, studying NanoVP kinetics in serum is challenging. DLS and NTA failed due to high levels of fluorescence from dissociated NanoVP monomers. Mixing NanoVP with whole blood then fractioned centrifugation followed by HPLC/MS-MS to identify which fraction of the blood NanoVP ends up in may be an interesting

approach. Recovering NanoVP from whole blood to evaluate particle diameter has proven difficult and potentially futile due to the relatively quick dissociation of NanoVP in serum.

3.6 Conclusions

This chapter establishes the kinetic profile of NanoVP in the blood, quantifies the biodistribution of VP in the body after injection, establishes that oral NanoVP is bioavailable, and indicates that VP may poorly cross the BBB. This understanding of NanoVP's pharmacokinetics and biodistribution informs how it may be used in PDT and in light-independent applications. NanoVP clears the body quickly, indicating that it may be desirable for PDT, but would require frequent dosing for its light-independent effects. NanoVP dissociates quickly in the blood to become photoactive, but the presence of particles with reduced diameter may allow longer stability in the blood. The oral bioavailability of VP was not previously known. The option to orally ingest a solution of NanoVP may be attractive for long-term treatment to avoid intravenous infusion for patients who may take NanoVP to prevent tumor spread long-term. Finally, the poor penetration of VP into the brain is not surprising but is concerning for light-independent applications of the drug. While VP can act on the vasculature during PDT, it does not have any known helpful activity in the vasculature in a light-independent manner. This raises concerns about the ability of VP to enter the intact BBB where residual cells may lie, undercutting its therapeutic potential. As a result, higher light-independent doses of NanoVP may be desirable for light-independent tumor control.

Chapter 4: Efficacy of NanoVP in Photodynamic and Light-Independent Therapy against Glioblastoma*

4.1 Introduction

The INDYGO clinical trial demonstrated that PDT performed with the drug 5-ALA delivered systemically and light administered within the surgical resection cavity only adds 35 minutes to surgery [65], but, unfortunately, improvements in survival remain to be seen [65]. Drawbacks of 5-ALA include its low singlet oxygen production, required conversion to PpIX, and limited ability to cross an intact BBB. VP is delivered as an active photosensitizer, meaning it can act in vasculature. It can also be activated deeper in the brain than PpIX [104-108]. VP was used once in a small Phase I trial (NCT00002647), resulting in no systemic or neurological side effects, but no other results were published. Further evaluation of VP as a PDT agent for GBM is warranted.

Considering recent clinical interest in the light-independent application of VP in GBM (NCT04590664), a logical step is the combination of light-dependent and light-independent applications of VP. In this chapter, I explore NanoVP as a therapeutic

* This chapter was adapted from Quinlan JA*, Inglut CT*, Srivastava P, Rahman I, Stabile J, Gaitan B, Arnau del Valle C, Baumiller K, Gaur A, Chiou W-A, Karim B, Connoly N, Robey RW, Woodworth GF, Gottesman MM, and Haung H-C, "Carrier-Free, Amorphous Verteporfin Nanodrug for Enhanced Photodynamic Cancer Therapy and Brain Drug Delivery." *Adv Sci (Weinh).* 2024;11(17):e2302872. doi:10.1002/advs.202302872 and Quinlan JA, Baumiller K, Gaur A, Chiow W-A, Robey RW, Gottesman MM, and Huang H-C, "Self-Assembled Verteporfin Nanoparticles for Photodynamic and Light-Independent Therapy in Glioblastoma." *Adv NanoBiomed Res.* 2024;2400098. doi: 10.1002/anbr.202400098. Permission was obtained from the publisher to use this material in the current dissertation.

option, evaluating its efficacy for PDT in GBM *in vivo* and its light-independent effects *in vitro*.

The screen that identified VP as a modulator of Hippo pathway signaling also identified PpIX and HPD as modulators of Hippo pathway signaling [118]. The authors did not pursue PpIX as a substrate due to its lower binding affinity for YAP, however, 5-ALA's oral bioavailability may be favorable for patient treatment if PpIX appears to also have the potential to operate in a light-independent manner. For this reason, we evaluated the ability of PpIX, 5-ALA, and HPD to modulate the activity of GBM cells in the absence of light.

4.2 Methods

4.2.1 NanoVP Synthesis

NanoVP was formulated as described in *Chapter 2*, either using Condition 1 or Condition 4 (**Table 2-1**), as specified in individual experiments.

4.2.2 Cell Cultures

The human GBM cell lines U87 and U251 were obtained from ATCC and cultured per the vendor's instructions. Both cell lines were cultured in Eagle's Minimum Essential Medium (EMEM; Cellgro, Lincoln, NE, USA) with 10% v/v fetal bovine serum (FBS; Gibco), 100 U/mL penicillin, and 100 µL/mL streptomycin. Cells were maintained in 5% CO_2 at 37°C and were regularly monitored for mycoplasma according to manufacturer protocols (MycoAlert, Lonza, Basel, CH).

GBM39 cells expressing luciferase were serially passaged in the flank of female J:NU mice (4-5 weeks old, #007850, Jackson Laboratory) as described in ***3.2.3***. Tumors were dissociated using a gentleMACS tumor dissociation kit (Miltenyi Biotec) before *in vitro* culturing. Cells were cultured as recommended by the Mayo Clinic Brain Tumor Patient-Derived Xenograft National Resource using the FBS cell culture protocol. Briefly, cells were cultured in DMEM containing 2.5% FBS, 100 U/mL penicillin, and 100 µg/mL streptomycin for 48 hours, then medium was exchanged to DMEM containing 10% FBS and antibiotics for at least 24 hours before experimentation. Cells were dissociated and used in experiments, but not passaged serially. Assays were performed within 14 days of tumor dissociation.

4.2.3 Preparation of Tris-Buffered Tween-20 Verteporfin

VP was dissolved in chloroform at a concentration of 250 µM and chloroform was evaporated under reduced pressure with a rotary evaporator. Tris-buffered tween-20 (TBST, 0.5%) was prepared by diluting a stock solution (ThermoScientific) with PBS (diluted to 1X from Calbiochem OmniPur 10X PBS (Millipore, 6507)). 1 mL of surfactant solution was added to a tube containing VP film and the samples were placed in a shaker at 37 °C at 100 rpm for 24 h. Samples were filtered using sterile syringe filters with 0.22 µm pore size (Millipore-Sigma).

4.2.4 Evaluation of Photosensitizer Uptake

GBM39 cells were cultured overnight in a 35-mm Petri dish (1-3.3×104 cells/cm^2) and then incubated with photosensitizer (i.e., NanoVP, free VP in DMSO, TBST VP, or liposomal VP at 1 µM; 5-ALA at 5 mM) for 1.5 hours. photosensitizer

uptake in cells was determined using extraction methods followed by VP fluorescence measurements (Excitation/Emission: 435/690±20 nm, Synergy Neo2, BioTek). Protein content was quantified *via* Bradford assay (MilliporeSigma).

4.2.5 Photodynamic Therapy Responses *in vitro*

For PDT studies, cells were plated in black-walled, clear bottom plates or 35-mm Petri dishes (1-3.3 x 104 cells/cm2) and allowed to adhere for 24 hours before incubation with NanoVP (0.25 μM) for 90 minutes. Cells were washed with PBS twice immediately before light irradiation (0-7.5 J/cm2, 10 mW/cm2, bottom illumination; ML6600, Modulight Corporation, Tampere, FIN). Cell viability was assessed 24 hours after treatment with CellTiter Glo (Promega).

4.2.6 *In vivo* Photodynamic Therapy

GBM39 cells were passaged and implanted as described in ***3.2.3*** and ***3.2.5.***

Fourteen days post-implantation, PDT was performed. The mice were randomly divided into NanoVP-PDT, liposomal VP-PDT, 5-ALA-PDT, TBST VP-PDT, and no treatment groups. Mice received 0.5 mg/kg tail vein injections of NanoVP, TBST VP, or liposomal VP and, after 2 hours, received 12 J/cm of 690 nm light (40 mW/cm) interstitially through the burr hole used to implant tumor cells (RD10 laser fiber, ML6600 laser, Modulight). Mice treated with 5-ALA PDT received 20 mg/kg 5-ALA IV four hours before laser irradiation with 635 nm light (100 mW/cm, 60 J/cm). Power level was measured using the Modulight MLACAL external calibration unit. All but 5mm from the tip of the RD10 fiber, matching the depth that the fiber penetrated the mouse brain, was covered with black masking tape (Thor Labs) before measuring

power according to manufacturer instructions. For maximum tolerable dose studies, power and irradiance were kept constant. Time was adjusted to increase the total delivered dose. For temperature measurement, a forward-looking infrared (FLIR) camera was aimed at the site where the laser fiber intersected with the brain and at a site on the laser fiber just above where the fiber intersected with the brain.

4.2.7 IVIS Imaging and Quantitation

IVIS imaging and quantification was performed as described in ***3.2.6***.

4.2.8 Light-Independent Cell Viability Studies

For light-independent VP viability studies, cells were incubated with NanoVP, Visudyne-like VP, 5-ALA, PpIX, or HPD for 72 hours before viability was measured *via* CellTiter Glo (Promega, Madison, WI, USA) or MTT assay (Sigma-Aldrich, St. Louis, MO, USA) according to manufacturer's protocols. Luminescence (CellTiter Glo) or absorbance at 580 nm (MTT) were measured *via* plate reader (Synergy Neo2, BioTek Instruments, Winooski, Vermont, USA).

4.2.9 Clonogenic Assay

U251 cells were seeded at a density of 45 cells/cm^2 (160 cells/well) in a 12-well dish. Cells were allowed to adhere for 24 hours. Cells were incubated with NanoVP, HPD, 5-ALA, or PpIX for 6 days. Cells were fixed with 10% formalin for 20 minutes, then stained with 0.1% crystal violet for 20 minutes and rinsed three times with PBS. Wells were imaged on a LionHeart plate imager (BioTek Instruments, Winooski, Vermont, USA) and colonies were manually counted in ImageJ. For clonogenic assays

after PDT, viable cells were counted using propidium iodide staining, and 45 cells/cm^2 of viable cells were plated in 12-well dishes for clonogenic development.

4.2.10 Gap Closure Assay

U251 cells were seeded in two-well silicone culture inserts (ibidi USA, Inc., Fitchburg, Wisconsin, USA) at a density of 50,000 cells/cm^2 (10,000 cells per well) and allowed to adhere for 24 hours. Before removal of the insert, cells were treated with mitomycin C (AdooQ Bioscience, Irvine, CA, USA) at a concentration of 10 µg/mL for one hour. Inserts were removed and cells were treated with 0-2.5 µM NanoVP. Gaps were imaged on a LionHeart imager at 0- and 24-hours post-insert removal. Gap area was quantified using ImageJ.

4.2.11 Histology, Immunohistochemistry, and Quantitation

Immunohistochemistry (IHC) staining on LeicaBiosystems' BondRX autostainer was performed with the following conditions: Epitope Retrieval 1 (Citrate) for nuclear mitotic apparatus protein 1 (NUMA1) and Fibrinogen, Epitope Retrieval 2 (EDTA) for MDR1/ABCB1, ZO-1, and C219. Sections were stained for NUMA1 (Lifespan #LS-B11047, 1:75 30'), Fibrinogen (Thermo #PA5-21968, 1:2000 30'), and MDR1/ABCB1 (Cell Signaling Technology #13978, 1:200 30') using the Bond Polymer Refine Detection Kit (LeicaBiosystems #DS9800) without the PostPrimary Reagent.

Sections stained for ZO-1 (Invitrogen #33-9100, 1:200 30') and C219 (non-commercial source, 1:200 30') required the M.O.M. ImmPRESS HRP Polymer Kit

(Vector Labs #MP-2400) and the Bond Polymer Refine Detection Kit (LeicaBiosystems #DS9800) without the PostPrimary and Polymer Reagents.

Isotype control reagents were used in place of primary antibodies for the negative controls. Slides were removed from the Bond autostainer, dehydrated through ethanols, cleared with xylenes, and coverslipped.

Slides for imaging native fluorescence were deparaffinized, rehydrated, and stained with 4',6-diamidino-2-phenylindole (DAPI) for 1 hour, rinsed, and coverslipped with ProLong™ Gold antifade reagent (Invitrogen #P36930).

Slides were scanned at 20X magnification using a Leica Aperio AT2 scanner (Leica Biosystems, Buffalo Grove, Illinois) to generate whole slide images. Quantification of the stained IHC slides was performed using HALO image analysis software version 3.6 (Indica Labs, Albuquerque, NM, USA). The Object Colocalization v1.3 algorithm was employed to measure the optical density for CD19, ZO-1, and MDR1, as well as the percent positive fibrinogen area. The tumor area was measured by manually annotating the tumor region in H&E slides using HALO software.

4.2.12 Statistics

Statistical tests were carried out using GraphPad Prism (GraphPad Software, San Diego, CA, USA) or Microsoft Excel (Microsoft, Redmond, WA, USA). Survival is displayed as a Kaplan-Meier plot with significance determined by Log-rank test between specific groups as indicated. IVIS signal and heat generation was compared with two-way ANOVA with Tukey's multiple comparisons test within each group. For

other biological assays, data is presented as mean ± standard deviation, and significance was determined by one-way ANOVA with Tukey's multiple comparisons against the control group, or a two-tailed Student's t-test. Comparison of signal from histology was only compared when n=3 for each group, and a two-tailed Student's t-test was used. All data presented is representative of at least three replicates.

4.3 Results

4.3.1 *In vitro* Photodynamic Therapy and Cellular Uptake of NanoVP

To support *in vivo* orthotopic tumor studies using the PDX GBM39, we evaluated the efficacy of NanoVP in GBM39 cells, which is a flank-passaged PDX model [189]. We first evaluated the efficacy of NanoVP-PDT in GBM39 cells cultured *in vitro*. Based on our pharmacokinetics results and the apparent dissociation of NanoVP in the blood, we hypothesized that NanoVP may functionally be a molecularly dispersed formulation of VP. We identified tris-buffered tween-20 (TBST) as a solubilizing aqueous solution for VP and added this molecularly dispersed formulation of the drug as a control (**Figure 4-1A, 4-1B**). We also compared NanoVP-PDT, free VP (in DMSO)-PDT, TBST VP-PDT, and liposomal VP-PDT to 5-ALA-PDT, which is currently in clinical trials for GBM (NCT04391062, NCT04469699, NCT03897491). In GBM39 cells, we found that NanoVP-PDT has the lowest IC_{25} of ~0.38 μM×J/cm^2, outperforming free VP-PDT (IC_{25} ≅ 0.62 μM×J/cm^2), TBST VP-PDT (IC_{25} ≅ 0.86 μM×J/cm^2), liposomal VP-PDT (IC_{25} ≅ 1 μM×J/cm^2), and 5-ALA-PDT (IC_{25} ≅ 110 mM×J/cm^2) (**Figure 4-2**). This may be partially attributable to

increased photosensitizer uptake with NanoVP over liposomal VP, TBST VP, and 5-ALA (PpIX) (**Figure 4-3**).

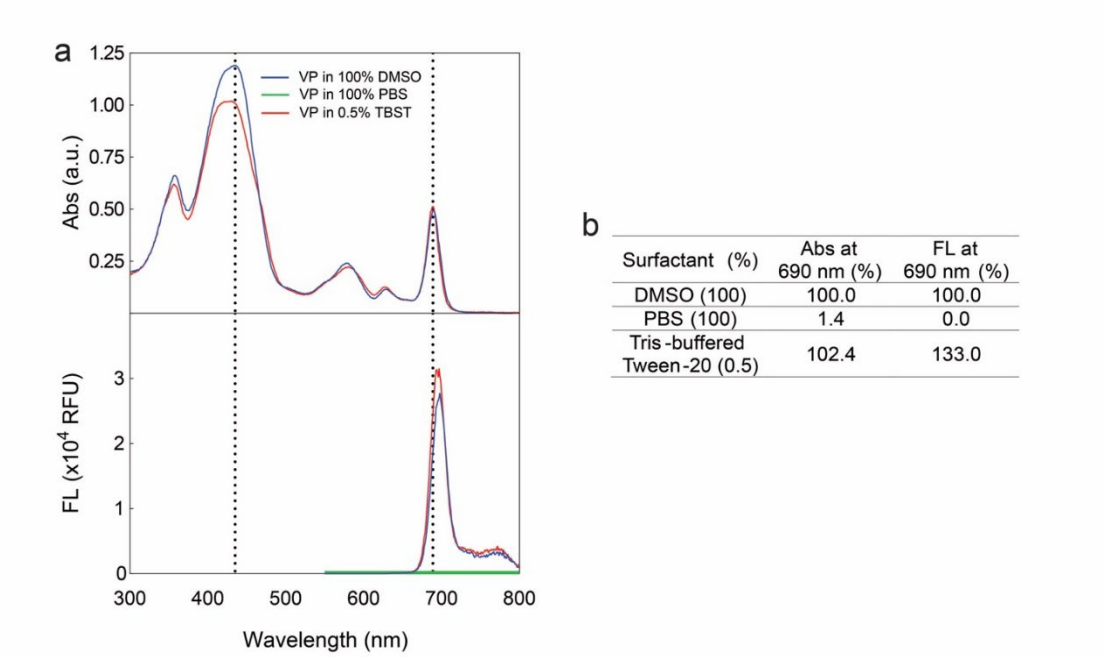

b

Surfactant (%)	Abs at 690 nm (%)	FL at 690 nm (%)
DMSO (100)	100.0	100.0
PBS (100)	1.4	0.0
Tris-buffered Tween-20 (0.5)	102.4	133.0

Figure 4-1. Formulation of tris-buffered tween-20 verteporfin, a molecularly dispersed VP control. VP is fully soluble in DMSO but not soluble in PBS; as such, absorbance and fluorescence are at a maximum in DMSO and minimum in PBS. (A) Absorption and fluorescence spectra (excitation: 435 nm) reveal that VP in 0.5% tris-buffered tween-20 (TBST) is fully unquenched and molecularly dispersed, as quantified in (B). No particles were observed on DLS, and the resulting mixture had VP dispersed throughout.*

* This figure was first published in Quinlan JA*, Inglut CT*, Srivastava P, Rahman I, Stabile J, Gaitan B, Arnau del Valle C, Baumiller K, Gaur A, Chiou W-A, Karim B, Connoly N, Robey RW, Woodworth GF, Gottesman MM, and Haung H-C, "Carrier-Free, Amorphous Verteporfin Nanodrug for Enhanced Photodynamic Cancer Therapy and Brain Drug Delivery." *Adv Sci (Weinh).* 2024;11(17):e2302872. doi:10.1002/advs.202302872.

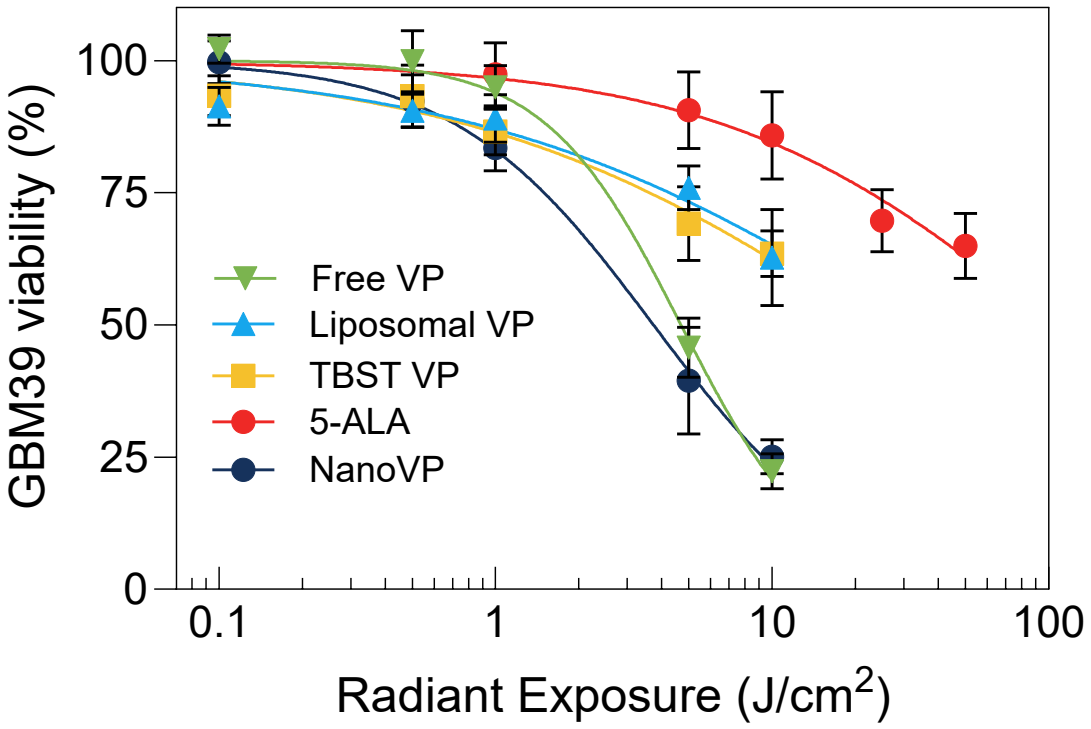

Figure 4-2. *In vitro* photodynamic therapy efficacy in GBM39 cells. GBM39 cells were explanted from the flank of mice and cultured for less than two passages to perform *in vitro* experiments. GBM39 cell viability measured *via* CellTiter Glo 24 hours after PDT treatment (VP formulations: 0.25 µM VP, 690 nm, 20 mW/cm^2, 0-10 J/cm^2; 5-ALA: 5 or 10 mM 5-ALA, 635 nm, 50 mW/cm^2, 0-50 J/cm^2). Error bars show SEM.[*]

[*] This figure was first published in Quinlan JA*, Inglut CT*, Srivastava P, Rahman I, Stabile J, Gaitan B, Arnau del Valle C, Baumiller K, Gaur A, Chiou W-A, Karim B, Connoly N, Robey RW, Woodworth GF, Gottesman MM, and Haung H-C, "Carrier-Free, Amorphous Verteporfin Nanodrug for Enhanced Photodynamic Cancer Therapy and Brain Drug Delivery." *Adv Sci (Weinh).* 2024;11(17):e2302872. doi:10.1002/advs.202302872.

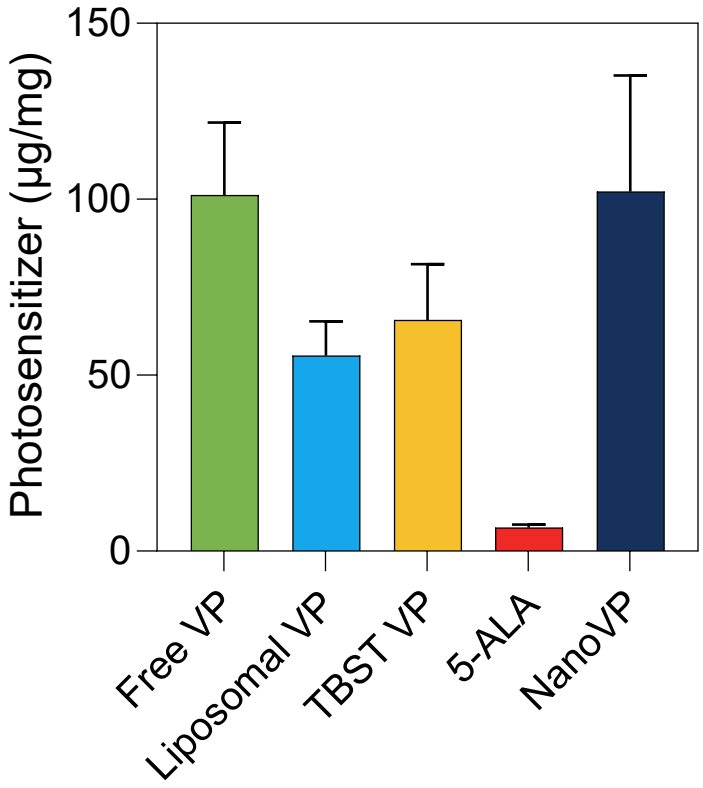

Figure 4-3. *In vitro* photosensitizer uptake in GBM39 cells. The uptake of photosensitizer in GBM39 cells *in vitro* was measured *via* extraction after 24 hours of incubation with 1 µM free VP, liposomal VP, TBST-VP, NanoVP, or 5 or 10 mM 5-ALA. In the case of 5-ALA-treated cells, PpIX was quantified. Error bars show SEM.[*]

[*] This figure was first published in Quinlan JA*, Inglut CT*, Srivastava P, Rahman I, Stabile J, Gaitan B, Arnau del Valle C, Baumiller K, Gaur A, Chiou W-A, Karim B, Connoly N, Robey RW, Woodworth GF, Gottesman MM, and Haung H-C, "Carrier-Free, Amorphous Verteporfin Nanodrug for Enhanced Photodynamic Cancer Therapy and Brain Drug Delivery." *Adv Sci (Weinh).* 2024;11(17):e2302872. doi:10.1002/advs.202302872.

4.3.2 Maximum Tolerable Photodynamic Therapy Dose in Orthotopic Glioblastoma

Interstitial PDT with VP has not been reported in the literature. As such, establishment of a maximum tolerable dose study was performed to identify an appropriate light dose. The NanoVP dose was maintained at 0.5 mg/kg dose based on dose conversion from human applications of VP. The main adverse event observed was brain edema leading to death, which was observed in the first 12-24 hours. For this reason, a 3+3 dose escalation study was performed, and mice were monitored for 72 hours before the next cohort received a higher dose. Findings were summarized in **Table 4-1**. A dose of 12 J/cm was found to be the maximum tolerable dose. One mouse died in the dose escalation study, but no mice died because of PDT during the survival study at the 12 J/cm dose.

Table 4-1. Maximum tolerable dose study for interstitial photodynamic therapy in an orthotopic model of glioblastoma. Two weeks post-implantation, mice bearing orthotopic GBM39 tumors received 0.5 mg/kg NanoVP *via* IV injection, then received interstitial PDT (690 nm, 40 mW/cm). Mice were observed for 72 hours according to a pain score sheet to identify a tolerable dose.

Dose (J/cm)	**n treated**	**n died within 72 hours**	**% Survival**
Control (tumor only)	5	0	100%
0	6	0	100%
4	5	0	100%
8	3	0	100%
10	3	0	100%
12	4	1	75%
14	3	3	0%
40	2	2	0%

4.3.3 Photodynamic Therapy in an Orthotopic Patient-Derived Xenograft of Glioblastoma

To evaluate the potential of NanoVP to control orthotopic GBM and improve animal survival, we injected $5x10^5$ GBM39 PDX cells expressing luciferase into the right striatum of nude mice. We utilized the GBM39 PDX, which is serially passaged in mice rather than cultured in dishes, to better recapitulate the tumor biology observed in patients. Fourteen days post-injection, when IVIS signal was robust and when mortality was first observed, we performed interstitial PDT (0.5 mg/kg NanoVP, TBST VP, or liposomal VP *via* tail vein injection; 12 J/cm, 40 mW/cm, 690 nm) by inserting a laser fiber (MedLight RD10 fiber, Modulight ML6600 laser) through the burr hole initially used to inject cells. Tolerable conditions for VP-PDT were established *via* a dose-escalation study and 5-ALA-PDT conditions were established based on current clinical trial parameters. 5-ALA is dosed at 20 mg/kg with a 4-hour drug-light interval in the clinic, with approximately 10 minutes added to surgical time and irradiances and fluences exceeding those explored in this study (**Table 1-1**). Sham mice received surgery to insert laser fiber but did not receive light or drug.

Body weight (**Figure 4-4**) as part of a body condition score was used to monitor animal health over the course of the study. We observed no increase in temperature at the site of PDT as measured by a FLIR infrared camera under conditions used to perform VP-PDT (690 nm, 40 mW/cm), but we did observe an increase in temperature at the site of PDT with 5-ALA-PDT treated mice (**Figure 4-5A**). Upon examination of the laser fiber itself, we identified a significant increase in temperature during and immediately after 5-ALA-PDT using 635 nm laser (**Figure 4-5B**). Ultimately, we

observed a potential zone of necrosis surrounding the laser insertion site in 5-ALA PDT-treated mice, while the neuropil recovered after PDT in control and NanoVP-PDT mice (**Figure 4-5C, 4-5D, 4-5E**).

We observed a 7-day median survival benefit in mice treated with NanoVP over untreated mice (28 days vs 21 days, $P < 0.05$, **Figure 4-6**) and a 10-day median survival benefit over mice treated with liposomal VP-PDT (28 days vs 18 days, $P < 0.05$, **Figure 4-6**). This significant survival benefit was likely due to the superior acute control of tumor growth: when normalized to pre-treatment bioluminescent signal. The bioluminescent signal one week post-treatment had the smallest increase in signal in the NanoVP-PDT group (mean 369% increase), while liposomal VP-PDT (mean 1590% increase), control (mean 1270% increase), TBST VP (mean 2030% increase), and 5-ALA PDT (mean 1680% increase) groups had significant increases in the bioluminescent signal (**Figure 4-7A, 4-7B**). The sham group had a 1233% increase in signal which did not reach significance, although this group had fewer animals than the other groups. While orthotopic interstitial PDT with NanoVP provided a significant median survival benefit and significant reduction of tumor burden, these results point out challenges in achieving long-term improvements in treatment response for GBM, highlighting the need for developing combination strategies to provide durable tumoricidal control in the future.

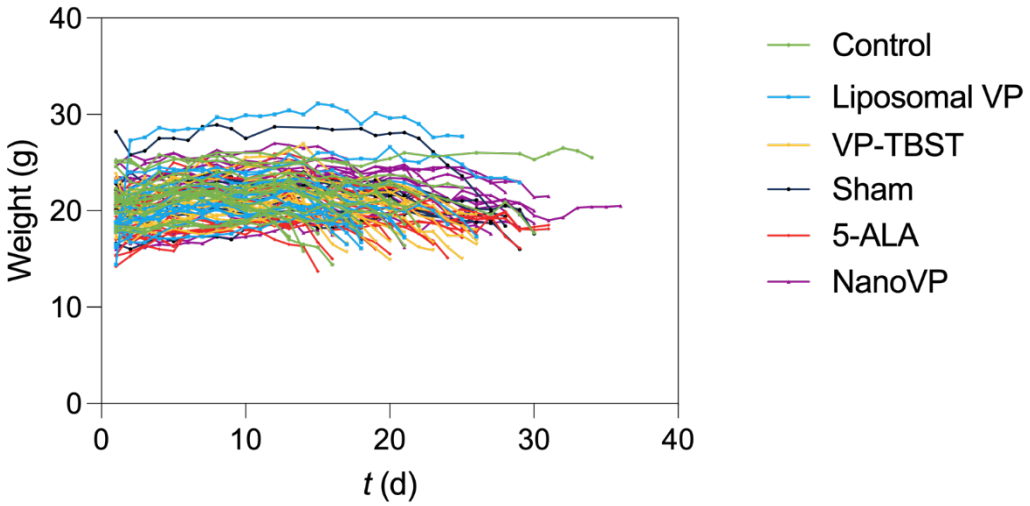

Figure 4-4. Mouse weight with intracranial tumor injection and interstitial PDT. Tumors were implanted on day 0 and PDT was performed on day 14. Mouse weight was minimally impacted by either procedure, although weight did decline as tumor burden increased.*

* This figure was first published in Quinlan JA*, Inglut CT*, Srivastava P, Rahman I, Stabile J, Gaitan B, Arnau del Valle C, Baumiller K, Gaur A, Chiou W-A, Karim B, Connoly N, Robey RW, Woodworth GF, Gottesman MM, and Haung H-C, "Carrier-Free, Amorphous Verteporfin Nanodrug for Enhanced Photodynamic Cancer Therapy and Brain Drug Delivery." *Adv Sci (Weinh).* 2024;11(17):e2302872. doi:10.1002/advs.202302872.

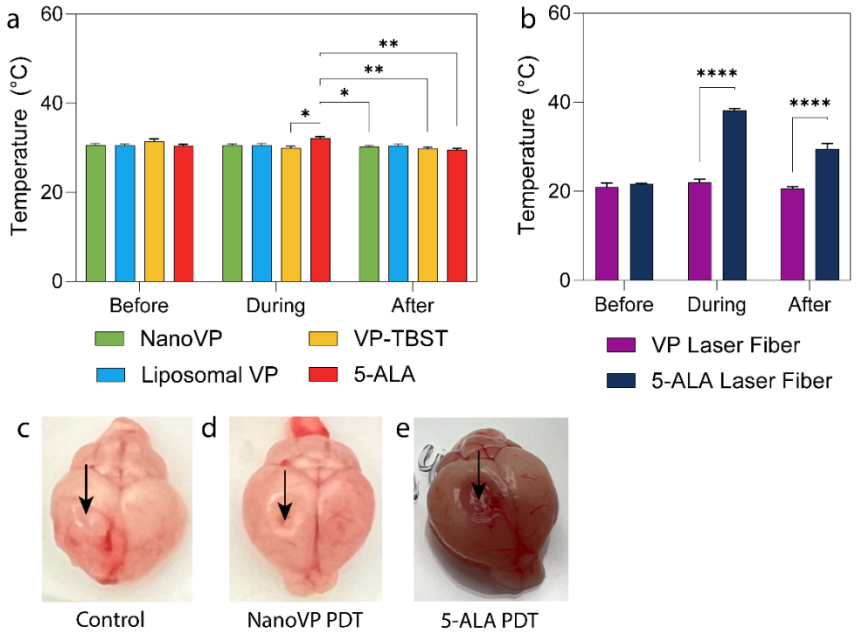

Figure 4-5. Photodynamic therapy with liposomal verteporfin, tris-buffered tween-20 verteporfin, or NanoVP does not generate heat *in vivo*, but the fiber used for 5-ALA PDT does generate heat. (**A**) A FLIR infrared camera was used to record temperature at the site of PDT as well as (**B**) the laser fiber before, halfway through, and immediately after PDT. A black arrow indicates the site of tumor cell injection and laser fiber insertion in (**C**) Control brains, (**D**) NanoVP-PDT treated brains, and (**E**) 5-ALA PDT treated brains, with an apparent ablation zone around fiber insertion site only in 5-ALA PDT treated brains at endpoint (approximately two weeks post-PDT). $N \geq 3$ for all groups. By two-way ANOVA with Tukey's multiple comparison test, * $P < 0.05$, ** $P < 0.01$, **** $P < 0.001$. Data presented as mean ± SEM.[*]

[*] This figure was first published in Quinlan JA*, Inglut CT*, Srivastava P, Rahman I, Stabile J, Gaitan B, Arnau del Valle C, Baumiller K, Gaur A, Chiou W-A, Karim B, Connoly N, Robey RW, Woodworth GF, Gottesman MM, and Haung H-C, "Carrier-Free, Amorphous Verteporfin Nanodrug for Enhanced Photodynamic Cancer Therapy and Brain Drug Delivery." *Adv Sci (Weinh).* 2024;11(17):e2302872. doi:10.1002/advs.202302872.

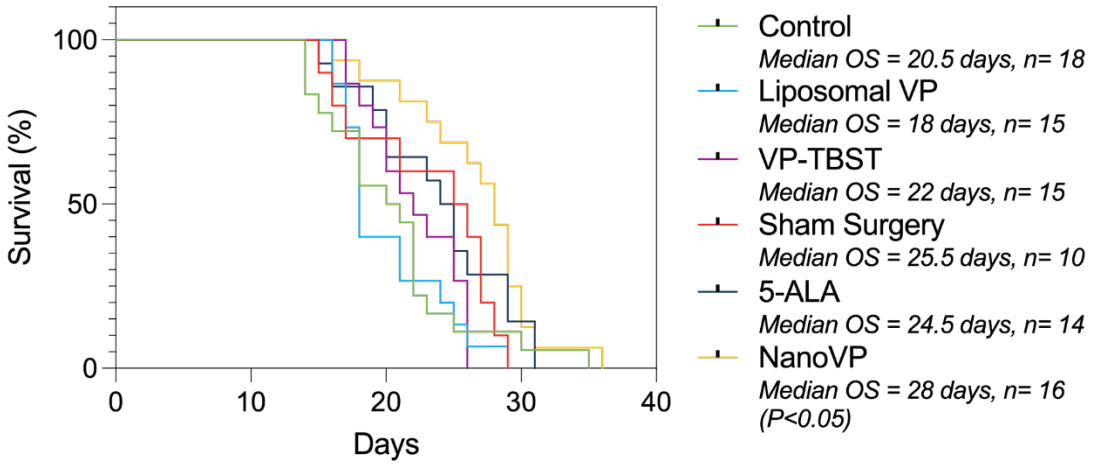

Figure 4-6. Efficacy of photodynamic therapy in an orthotopic model of glioblastoma. Kaplan-Meier plot for survival after treatment with PDT with liposomal-PDT or NanoVP-PDT; $P < 0.05$ by Log-rank test. For *in vivo* experiments, $5x10^5$ GBM39 cells were implanted intracranially. After two weeks, interstitial PDT with liposomal VP, NanoVP, or TBST VP (0.5 mg/kg IV, 2-hour drug-light interval, 12 J/cm, 40 mW/cm) or 5-ALA (20 mg/kg IV, 4-hour drug-light interval, 60 J/cm, 100 mW/cm) was performed.[*]

[*] This figure was first published in Quinlan JA*, Inglut CT*, Srivastava P, Rahman I, Stabile J, Gaitan B, Arnau del Valle C, Baumiller K, Gaur A, Chiou W-A, Karim B, Connoly N, Robey RW, Woodworth GF, Gottesman MM, and Haung H-C, "Carrier-Free, Amorphous Verteporfin Nanodrug for Enhanced Photodynamic Cancer Therapy and Brain Drug Delivery." *Adv Sci (Weinh).* 2024;11(17):e2302872. doi:10.1002/advs.202302872.

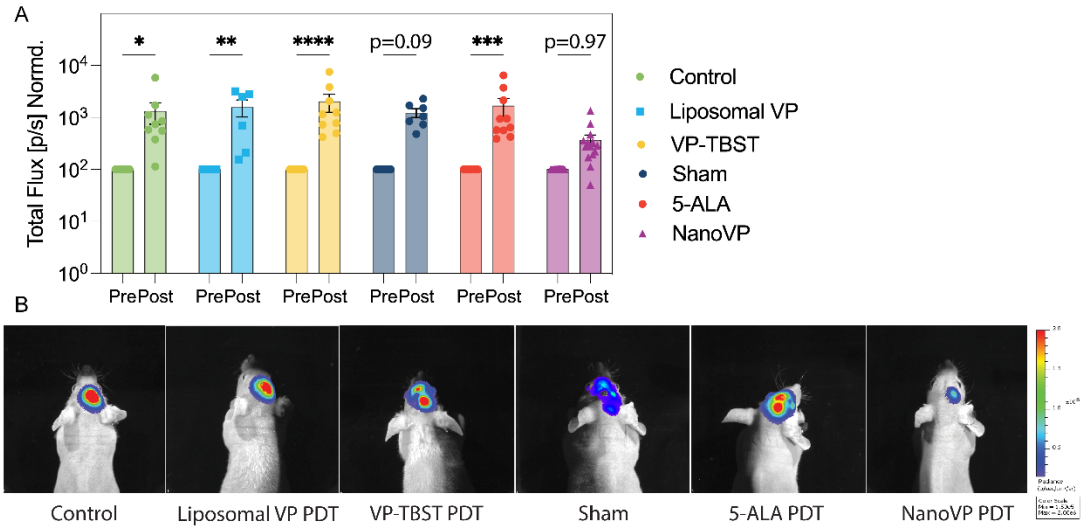

Figure 4-7. IVIS bioluminescent tumor burden in photodynamic therapy-treated mice. (**A)** GBM39 cells express luciferase; total bioluminescence was used as a proxy for tumor size at 1-week post-treatment (day 21) and normalized to pretreatment values (day 14) (N=8 for Control, N=6 for liposomes, N=7 for Sham, N=9 for TBST VP, N=10 for 5-ALA, N=14 for NanoVP). Two-way ANOVA with multiple comparison test was used to calculate significant differences, where * $P < 0.05$, ** $P < 0.01$, **** $P < 0.0001$. Error bar shows the SEM, individual dots indicate individual animals. (**B**) Representative images showing better tumor control with NanoVP at day 21, 1-week post-treatment.*

* This figure was first published in Quinlan JA*, Inglut CT*, Srivastava P, Rahman I, Stabile J, Gaitan B, Arnau del Valle C, Baumiller K, Gaur A, Chiou W-A, Karim B, Connoly N, Robey RW, Woodworth GF, Gottesman MM, and Haung H-C, "Carrier-Free, Amorphous Verteporfin Nanodrug for Enhanced Photodynamic Cancer Therapy and Brain Drug Delivery." *Adv Sci (Weinh).* 2024;11(17):e2302872. doi:10.1002/advs.202302872.

4.3.4 Light-Independent Activity of NanoVP

Next, we evaluated the potential of NanoVP to inhibit growth and migration of GBM cells *in vitro* in the absence of light. First, we treated cells with Visudyne-like VP (**Figure 2-3**) and NanoVP for 72 hours, then assessed viability *via* CellTiter Glo (**Figure 4-8A, 4-8B**). In U87s and U251s, the Visudyne-like formulation and NanoVP performed similarly. For U87 cells, the IC_{50}s were 13 ± 3.5 μM for NanoVP and 9.8 ± 0.62 for Visudyne-like VP ($p=0.16$ by two-tailed Student's t-test). For U251 cells, the IC_{50}s were 9.1 ± 1.87 for NanoVP and 7.4 ± 0.80 for Visudyne-like VP ($p=0.22$ by two-tailed Student's t-test).

Next, we evaluated the ability of NanoVP to inhibit the clonogenic capacity of U251 cells by plating U251 cells at a low density and treating them with NanoVP for 6 days (**Figure 4-9A**). Normalized colony count indicated a decrease in clonogenic capacity at concentrations higher than 0.25 μM (**Figure 4-9B**), which is a concentration that is efficacious for PDT [111]. We also evaluated the ability of NanoVP to inhibit gap closure in U251 cells, where cells were seeded on either side of a silicone insert, then allowed to migrate for 24 hours in the presence of NanoVP (**Figure 4-10A, 4-10B**). We observed a decrease in gap closure at concentrations above the dose that is efficacious for PDT, which is 0.25 μM.

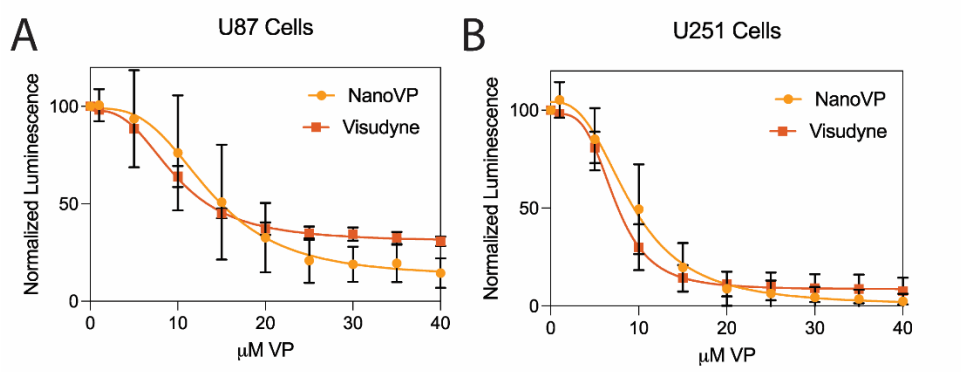

Figure 4-8. Light-independent killing of U87 and U251 cells by NanoVP and Visudyne-like VP. To evaluate light-independent efficacy of VP, CellTiter Glo was used to estimate viability in (A) U87 and (B) U251 cells was assessed after 72 hours of incubation with either NanoVP or a Visudyne-like formulation of liposomal VP. NanoVP and Visudyne-like formulation of liposomal VP. NanoVP and Visudyne-like VP performed similarly. Points show mean of at least 3 replicates, error bars show SD.[*]

[*] This figure was first published in Quinlan JA, Baumiller K, Gaur A, Chiow W-A, Robey RW, Gottesman MM, and Huang H-C, "Self-Assembled Verteporfin Nanoparticles for Photodynamic and Light-Independent Therapy in Glioblastoma." *Adv NanoBiomed Res.* 2024;2400098. doi: 10.1002/anbr.202400098.

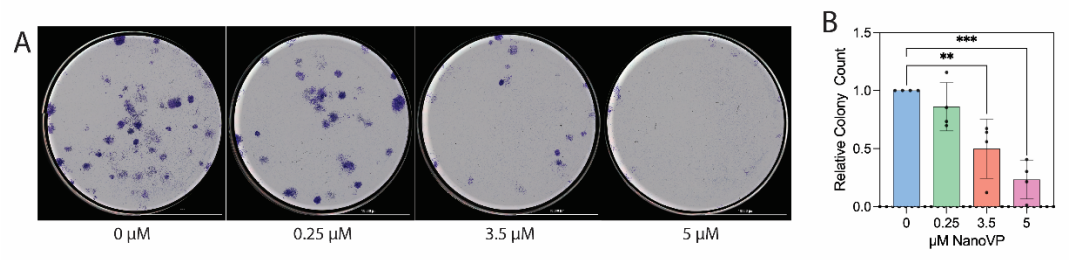

Figure 4-9. NanoVP inhibits clonogenic capacity of U251 cells. (A) Clonogenic assays (160 cells/well) and (B) quantification revealed a dose-dependent decrease in clonogenic capacity in U251 cells after 8 days of incubation. Significance was determined *via* one-way ANOVA with Tukey's multiple comparisons against the control. * indicates $p<0.05$, ** $p<0.01$, and *** $p<0.001$. Graph shows mean ± SD with individual points indicating individual replicates.[*]

[*] This figure was first published in Quinlan JA, Baumiller K, Gaur A, Chiow W-A, Robey RW, Gottesman MM, and Huang H-C, "Self-Assembled Verteporfin Nanoparticles for Photodynamic and Light-Independent Therapy in Glioblastoma." *Adv NanoBiomed Res.* 2024;2400098. doi: 10.1002/anbr.202400098.

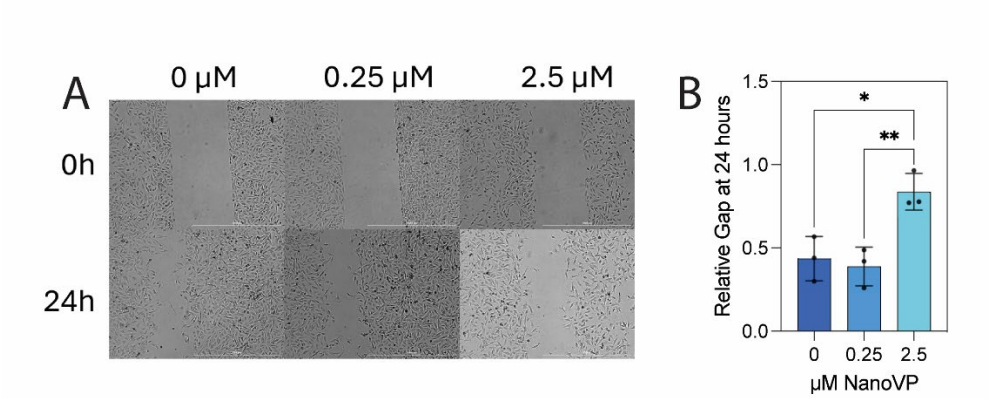

Figure 4-10. NanoVP decreases the migratory capacity of U251 cells. (A) A gap closure assay and (B) quantification revealed decreased movement of U251 cells after 24 hours of incubation with drug. Significance was determined *via* one-way ANOVA with Tukey's multiple comparisons against the control. * indicates $p<0.05$, ** $p<0.01$, and *** $p<0.001$. Graph shows mean ± SD with individual points indicating individual replicates.[*]

[*] This figure was first published in Quinlan JA, Baumiller K, Gaur A, Chiow W-A, Robey RW, Gottesman MM, and Huang H-C, "Self-Assembled Verteporfin Nanoparticles for Photodynamic and Light-Independent Therapy in Glioblastoma." *Adv NanoBiomed Res.* 2024;2400098. doi: 10.1002/anbr.202400098.

4.3.5 Combining Photodynamic Therapy and Light-Independent Activity of NanoVP

Because VP has been used in the clinic for over 20 years as a PDT agent [165], we evaluated the impact of combined PDT and light-independent application of NanoVP. First, we performed PDT on cells, then plated only viable cells for clonogenic evaluation. After adhering for 24 hours, cells were treated with 0.25 or 3.5 μM NanoVP in the dark for 6 days. In U251 cell, we found that there was a significant decrease in clonogenic capacity after PDT at levels greater than the PDT-dose light-independent control (**Figure 4-11A, 4-11B, 4-11C, 4-11D**). Even with low PDT doses of 0.1 J/cm^2, there was decreased clonogenic capacity in the group treated with 3.5 μM NanoVP in the absence of light. We also evaluated the combination of PDT and dark effects of VP in U87 cells. In this assay, cells were plated, PDT was performed, and then cells were treated with the light-independent IC_{25}, IC_{50}, or IC_{75} for NanoVP on U87 cells [111]. *Via* MTT assay, we found no combinatorial effect between PDT and the light-independent application of NanoVP in U87 cells (**Figure 4-12A, 4-12B, 4-12C**), with cell viability being driven, apparently, by either PDT or light-independent effects of VP.

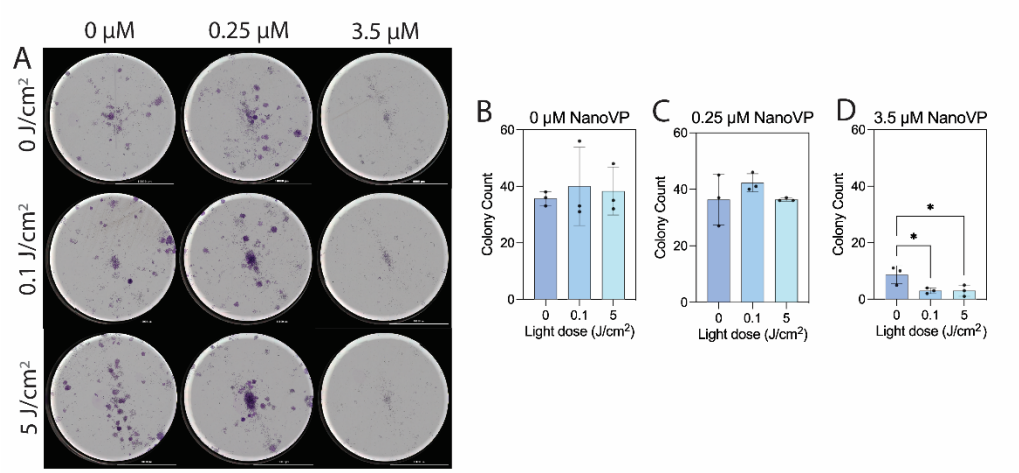

Figure 4-11. The combination of NanoVP-photodynamic therapy and light-independent NanoVP in clonogenic assays. To combine NanoVP-PDT with light-independent effects of NanoVP, a clonogenic assay (A) on U251 cells was performed where cells received NanoVP PDT (0.25 µM NanoVP for 90 minutes, washed twice with PBS before light irradiation (690 nm, 10 mW/cm^2, 0-5 J/cm^2)). The next day, 160 viable cells/well were seeded and allowed to adhere for 24 hours. Cells were then incubated with NanoVP in the dark (0-3.5 µM) for 6 days. When quantified, no combinatorial effect was observed with (B) 0 µM or (C) 0.25 µM light-independent NanoVP, but a significant decrease in colony count was observed with (D) 3.5 µM light-independent NanoVP in groups that also received PDT. Significance was determined *via* one-way ANOVA with Tukey's multiple comparisons against the control. * indicates $p<0.05$, ** $p<0.01$, and *** $p<0.001$. Graph shows mean ± SD with individual points indicating individual replicates.[*]

[*] This figure was first published in Quinlan JA, Baumiller K, Gaur A, Chiow W-A, Robey RW, Gottesman MM, and Huang H-C, "Self-Assembled Verteporfin Nanoparticles for Photodynamic and Light-Independent Therapy in Glioblastoma." *Adv NanoBiomed Res.* 2024;2400098. doi: 10.1002/anbr.202400098.

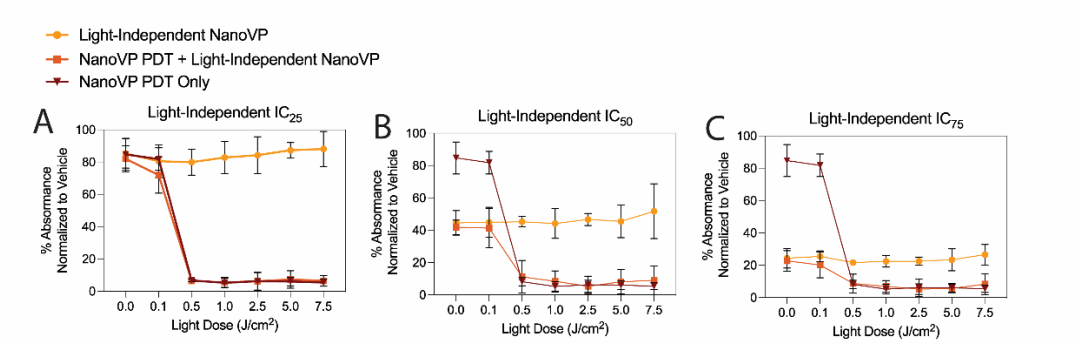

Figure 4-12. Combination of NanoVP-photodynamic therapy with light-independent NanoVP in cell viability assays. When U87 cells received PDT (0.25 µM NanoVP for 90 minutes, washed twice with PBS before light irradiation (690 nm, 10 mW/cm^2, 0-7.5 J/cm^2)) then light-independent NanoVP at their (A) IC_{25}, (B) IC_{50}, or (C) IC_{75} for 72 hours before MTT assay, no combinatorial effect was observed, and cell killing was dictated by either the light-independent NanoVP or the NanoVP-PDT. Graph shows mean ± SD with individual points indicating individual replicates.[*]

[*] This figure was first published in Quinlan JA, Baumiller K, Gaur A, Chiow W-A, Robey RW, Gottesman MM, and Huang H-C, "Self-Assembled Verteporfin Nanoparticles for Photodynamic and Light-Independent Therapy in Glioblastoma." *Adv NanoBiomed Res.* 2024;2400098. doi: 10.1002/anbr.202400098.

4.3.6 Evaluation of Chemotherapeutic Potential of Other Porphyrin-Based Photosensitizers

The initial screen that identified VP as a disruptor of YAP-TAZ interaction also identified PpIX and HPD as YAP-TAZ disruptors [118]. We hypothesized that PpIX and its prodrug 5-ALA as well as HPD may have antitumor efficacy in the absence of light. We first confirmed that 5-ALA (**Figure 4-13A**), PpIX (**Figure 4-13B**), and HPD (**Figure 4-13C**) exhibited *in vitro* GBM cell killing in both U87 and U251 cells in the absence of light. Their IC_{50}s are summarized in **Table 4-2**. Next, we found that 5-ALA (**Figure 4-14A, 4-14D**), PpIX (**Figure 4-14B, 4-14E**), and HPD (**Figure 4-14C, 4-14F**) decreased clonogenic capacity of U251 cells in the absence of light at concentrations below their light-independent IC_{50}s.

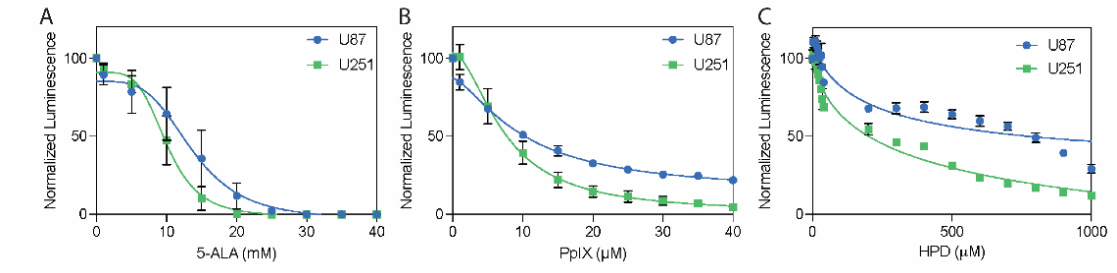

Figure 4-13. Light-independent toxicity of porphyrin-based photosensitizers on glioblastoma cells *in vitro*. To evaluate light-independent efficacy of (A) 5-ALA, (B) PpIX, and (C) HPD, CellTiter Glo was used to estimate viability in U87 and U251 cells after 72 hours of incubation with the drug of interest. Points show mean value from at least 3 replicates, error bars show SD.

Table 4-2. Light-independent IC_{50}s of several photosensitizers in glioblastoma cell lines. U87 or U251 cells were incubated with the photosensitizer of interest for 72 hours, then CellTiter Glo assay was used to quantify viable cells. For all groups, n≥3 biological replicates.

Photosensitizer	**U87 Cells**	**U251 Cells**
NanoVP (μM)	13 ± 3.5	9.1 ± 1.8
Visudyne-Like VP (μM)	9.8 ± 0.62	7.4 ± 0.80
5-ALA (mM)	13 ± 5.2	10 ± 2.6
PpIX (μM)	9.7 ± 2.2	10 ± 2.6
HPD (μM)	310 ± 200	310 ± 160

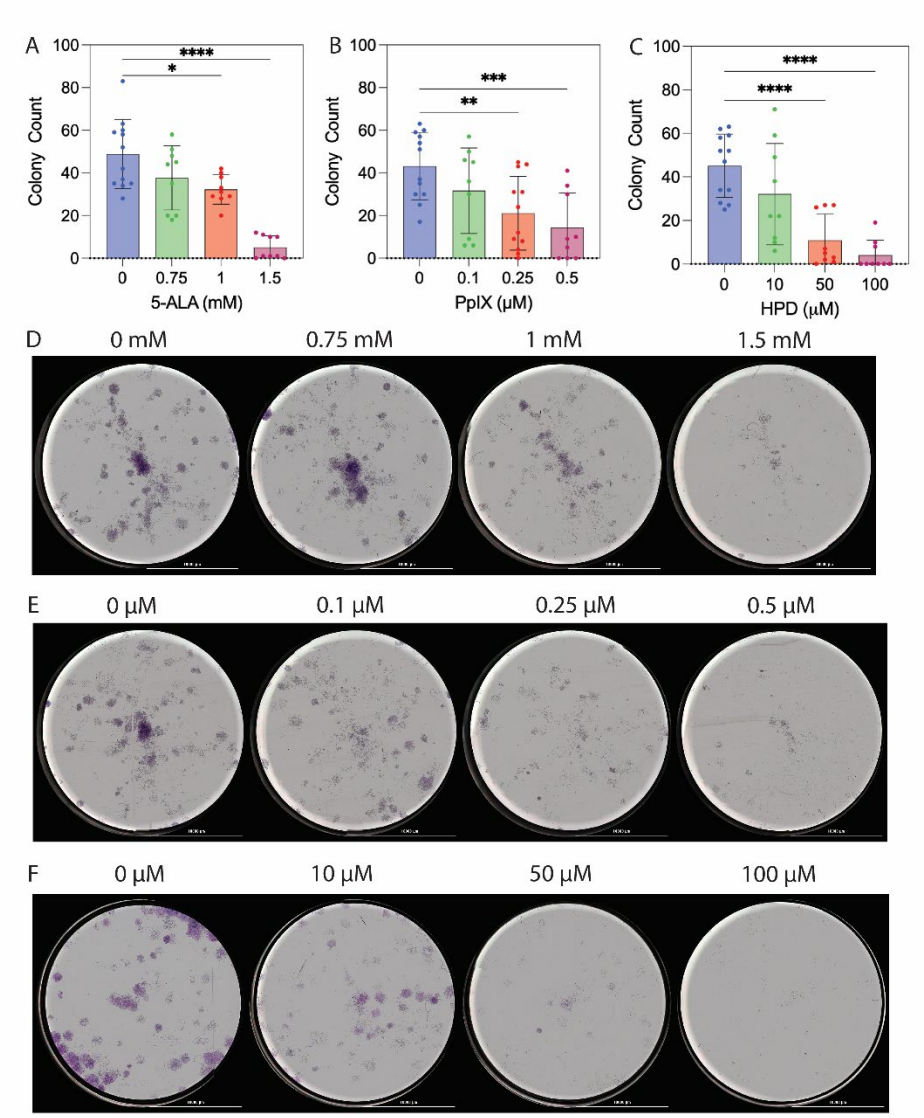

Figure 4-14. Porphyrin-based photosensitizers inhibit clonogenic capacity in the absence of light. U251 cells (160 cells/well) were treated with (A, D) 5-ALA, (B, E) PpIX, and (C, F) HPD for 8 days, then cells were fixed (D, E, F) and raw colony counts were quantified (A, B, C). Significance was determined *via* one-way ANOVA with Tukey's multiple comparisons against the control. * indicates $p<0.05$, ** $p<0.01$, *** $p<0.001$, and **** $p<0.0001$. Graph shows mean ± SD with individual points indicating individual replicates. Scale bar is 1000 μm.

4.3.7 Towards Combination of NanoVP Therapy with Glioblastoma Standards of Care Therapies

As most GBM patients receive surgical resection, radiation therapy, and temozolomide chemotherapy, we initiated investigation into the combinatorial effects of light-independent NanoVP and temozolomide. We found that NanoVP did not significantly impact the IC_{50} of temozolomide in U87 cells (**Figure 4-15A, 4-15B**) or U251 cells (**Figure 4-15C, 4-15D**).

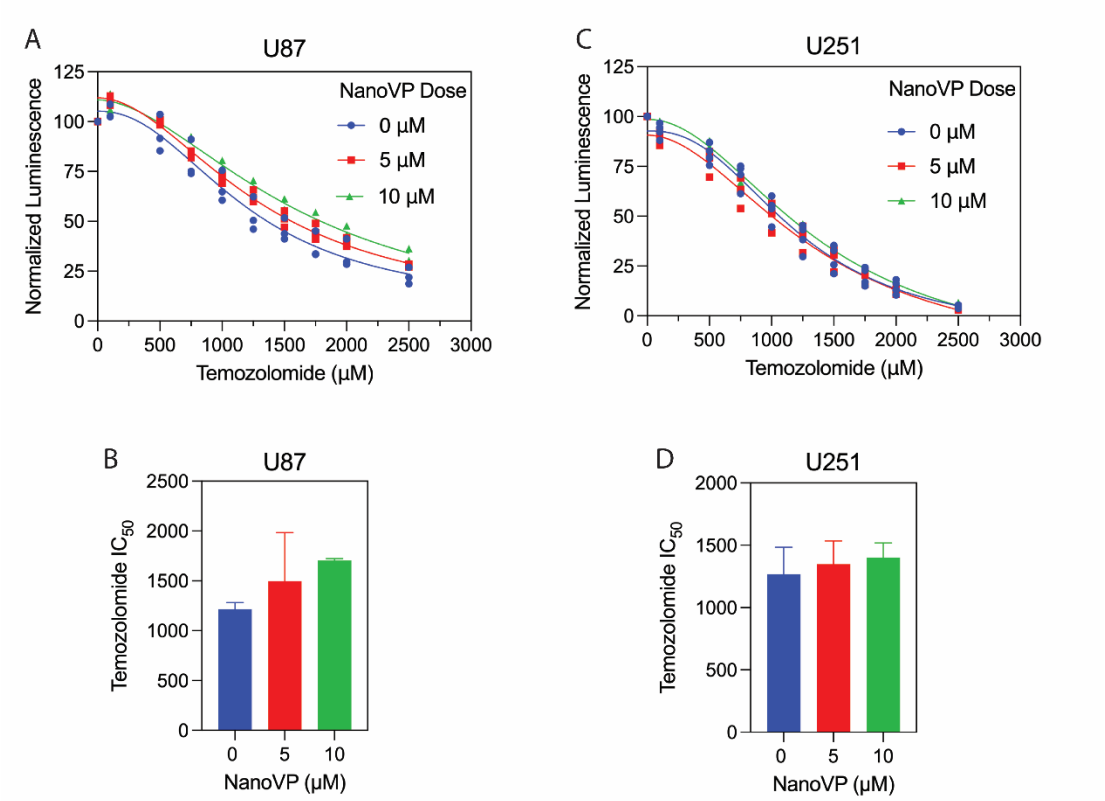

Figure 4-15. Response of glioblastoma cell lines to treatment with NanoVP and temozolomide. (A, B) U87 cells and (C, D) U251 cells did not show a change in IC_{50} when cotreated with NanoVP and TMZ. For 0 and 5 µM, n≥3; for 10 µM, n=2. For (B, D), no significance was detected by one-way ANOVA. Graph shows mean value in (A) and (C) and mean ± SD in (B) and (D). Experiments performed with Kaitlyn Moore.

4.3.8 Towards *in vivo* Evaluation of Blood-Brain Barrier Modification by Photodynamic Therapy

Brain tissues from the dose escalation study (**Table 4-1**) were collected and stained for tumor markers and markers of BBB integrity. Hematoxylin and eosin (H&E) (**Figure 4-16A**) staining as well as human nuclear mitotic apparatus protein 1 (NUMA1) (**Figure 4-16B**) revelated tumor cores at the site of injection and in some more distal areas, potentially due to cell seeding or invasion. Fibrinogen staining, when quantified in the vicinity of blood vessels on the tumor-bearing and PDT-treated side compared to the control side, revealed elevated levels of fibrinogen significantly in appropriately powered groups, indicating serum exudate around blood vessels and potential BBB permeabilization (quantified, **Figure 4-16C;** untreated, **4-16D;** 12 J/cm treated, **4-16E**). ABCB1 levels, visualized using the MDR1 (quantified, **Figure 4-16F;** untreated, **4-16G;** 12 J/cm treated, **4-16H**) and the C219 antibody (quantified, **Figure 4-16I;** untreated, **4-16J;** 12 J/cm treated, **4-16K**) and quantified as colocalization around blood vessels in the treated and untreated hemispheres, was significantly decreased in appropriately powered groups. ZO-1 staining, a marker of tight junction formation, revealed no significant decrease in zonulin-1 levels between the treated and untreated hemispheres as quantified by colocalization with blood vessels (quantified, **Figure 4-16L;** untreated, **4-16M;** 12 J/cm treated, **4-16N**).

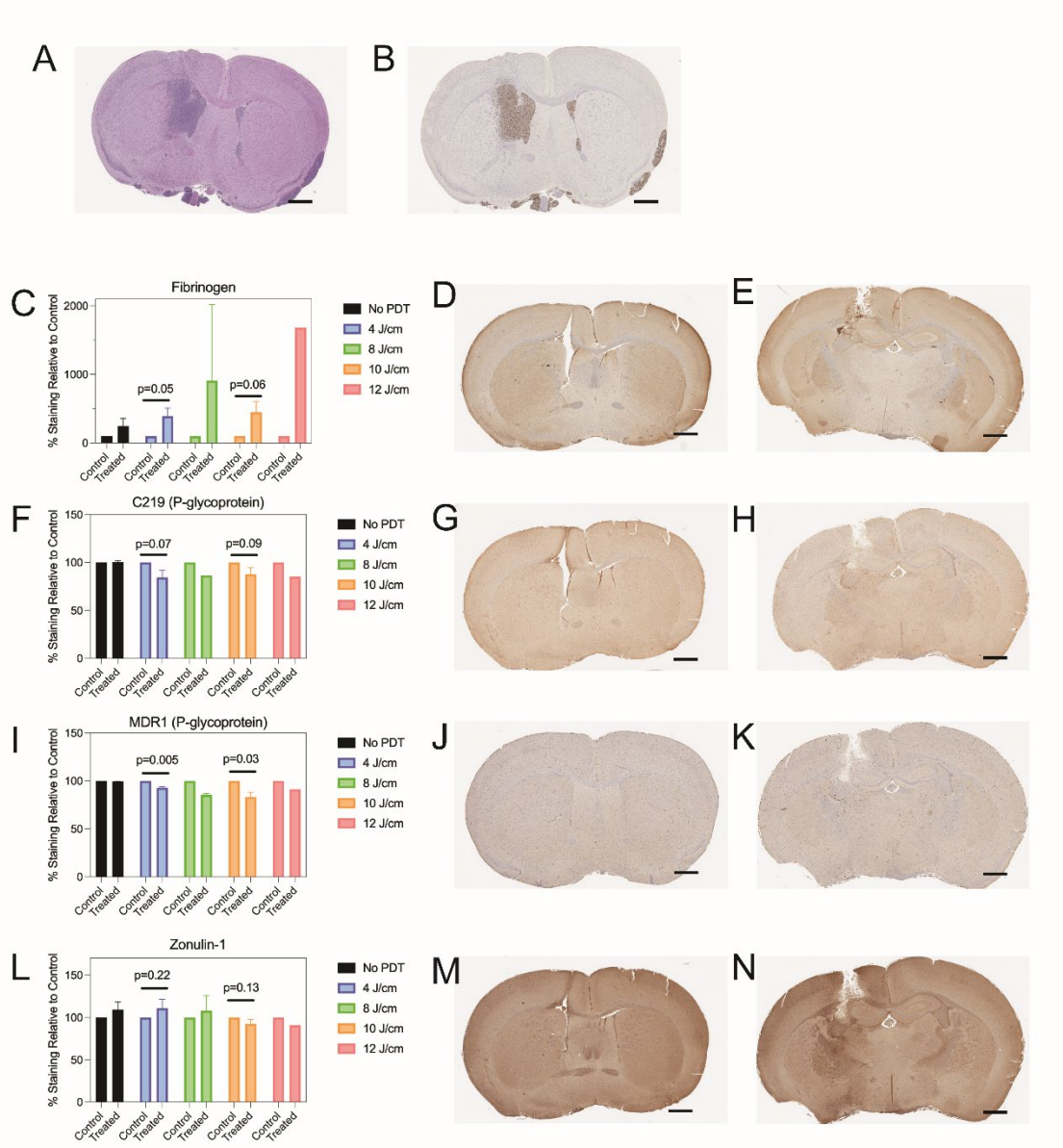

Figure 4-16. Histology of mouse brains post-photodynamic therapy for blood-brain barrier integrity markers. Mice bearing GBM39 tumors and treated with PDT as part of the dose-escalation study were sacrificed 72 hours after PDT and their brains were stained for markers of BBB integrity. (A) H&E and (B) human NUMA1 revealed GBM39 tumor burden near the site of implantation in most mice. (C) Fibrinogen levels around blood vessels were significantly increased in the treated and tumor-bearing hemisphere compared to the untreated hemisphere. Representative images of (D) untreated and (E) 12 J/cm treated brains stained for fibrinogen. (F) ABCB1 levels as visualized by C219 antibody stains around blood vessels were significantly decreased in the treated and tumor-bearing hemisphere compared to the untreated hemisphere. Representative images of (G) untreated and (H) 12 J/cm treated brains stained with C219. (I) ABCB1 levels as visualized by the MDR1 antibody around blood vessels were significantly decreased in the treated and tumor-bearing hemisphere compared to

the untreated hemisphere. Representative images of (J) untreated and (K) 12 J/cm treated brains stained with MDR1. (L) ZO-1 levels around blood vessels were not significantly changed in the treated and tumor-bearing hemisphere compared to the untreated hemisphere. Representative images of (D) untreated and (E) 12 J/cm treated brains stained for zonulin-1. Data should be regarded as preliminary as group numbers are not fully powered (No PDT, n=2; 4 J/cm, n=3; 8 J/cm, n=2; 10 J/cm, n=3; 12 J/cm, n=1). Statistics are only shown for groups where n=3 and represent a two-tailed Student's t-test. Graphs show mean ± SD. Scale bar is 1 mm.

4.4 Discussion

The main goal of this chapter was to evaluate the potential for NanoVP to perform as a PDT agent, in a light-independent manner, and when these two different mechanisms are combined. To evaluate this, we performed *in vivo* experiments using a PDX implanted orthotopically, and used this PDX and two commonly used GBM cell lines, U87 and U251, for *in vitro* experimentation.

We found that NanoVP kills GBM39 cells with efficacy similar to VP delivered in DMSO, potentially indicating that carriers (e.g. liposomes and TBST) inhibit intracellular accumulation. Quantification of intracellular photosensitizer supported this concept. 5-ALA did not perform well as a PDT agent, potentially due to low PpIX conversion or due to low singlet oxygen production.

Intraoperative NanoVP-PDT has a high translational potential. Surgery followed by PDT of GBM has been studied in the clinic (NCT03048240, NCT03897491, NCT00003788) [61, 200]. After establishing safe dosing parameters, we found that NanoVP-PDT outperformed all other photosensitizer formulations. Interestingly, we found that our sham surgery group fared better than controls and had a nonsignificant increase in bioluminescence one-week post-treatment. The insertion of the fiber may have mechanically killed some tumor cells, potentially inducing antitumor immunity. The core region may have been necrotic in the PDT-treated group, which may have impeded the ability of remaining immune cells in the mice to reach the antigen-rich region. Further work is warranted to understand the immune response to PDT in GBM.

In our study, we compared survival and tumor burden after interstitial PDT using liposomal VP, TBST-VP, 5-ALA, and NanoVP, with a sham surgery control group and an untreated control group. We found that survival with NanoVP PDT was significantly longer than survival after no treatment or after liposomal VP PDT. Sham surgery, TBST-VP PDT, and 5-ALA PDT all fell between the two groups, and survival was not significantly different from untreated, liposomal VP PDT treated, or NanoVP PDT treated groups. This may be a reflection of BD. NanoVP may have dissociated in the blood to become bioavailable in the brain interstitum around the tumor as well as in the vasculature, permitting immediate cell death and longer-term nutrient starvation. We included 5-ALA-PDT, which is currently under investigation in the clinic, to benchmark NanoVP-PDT against a clinically relevant PDT approach. Improved efficacy of NanoVP-PDT over 5-ALA-PDT may be attributable to greater intracellular accumulation of the photosensitizer, as observed *in vitro*. Additionally, VP-PDT will impact the vasculature, while 5-ALA is not converted to PpIX at considerable levels in the vasculature. 5-ALA PDT may have stalled tumor growth to some extent, but the heating from the laser fiber is confounding as thermal cell ablation may have also played a role. We also compared NanoVP to TBST VP, a molecularly dispersed formulation that was identified as an appropriate control. The improved performance of NanoVP-PDT over TBST VP-PDT may be attributable to changes in the association of VP with plasma molecules, resulting in differing biodistribution and ultimately differing efficacy of VP-PDT, as has been observed historically with liposomal VP [170, 171, 184, 185]. The kinetics of TBST-VP are not well understood, and the association of VP with other molecules in TBST-VP is unclear. Further research into

how TBST-VP performs may be useful, especially in understanding if it remains primarily in the vasculature or if it extravasates into the stroma. Liposomal VP may have remained primarily in liposomes, permitting only vascular shutdown, although, even then, oxidation may have only occurred directly towards lipids in the liposome. Future work will investigate the behavior of NanoVP in the blood and its subsequent anticancer performance, as this behavior may be important for the differences in performance of the studied VP formulations.

Also of note was the increase in survival and tumor debulking observed in the sham surgery group. It is possible that the blunt trauma of the surgery to the tumor (i.e. direct mechanical action of the laser fiber onto tumor cells or vasculature) may be responsible for some change in tumor growth. Previous studies have shown that incisions alone induce inflammation that results in some antitumor immunity, which has no effect on the acute cytotoxicity of PDT [201]. This observed effect was primarily through Cluster of Differentiation (CD) 8+ T cells. The mice used in this study, *Foxn1*^{nu}*/Foxn1*^{nu} or J:Nu mice, are athymic, meaning that they cannot mature T cells and have no cytotoxic T cells. They do still have microglia [202], which can induce antitumor immunity post-surgery [203]. Additionally, PDT in particular has been shown to activate the complement system, which is intact in J:Nu mice, as well as T cells to induce anti-tumor immunity in glioma specifically [204]. This may warrant further investigation into anti-glioma immunity induced in a syngeneic model [205], either in rats [206] or mice [207].

Despite promising results, the side effects of PDT remain a major concern [208-212]. For example, we noted the generation of heat in the laser fiber used for 635 nm

activation of 5-ALA. The photothermal effect may provide additional ablative power but may also present a serious complication for patients. On the other hand, we observed no heat generation for 690 nm activation of NanoVP formulations, which is notable considering the advancement of 5-ALA-PDT in the clinic.

We evaluated the ability of NanoVP to impact cell proliferation, clonogenic capacity, and motility, and examined the interaction between sequential PDT and light-independent activity of the NanoVP. We found that NanoVP performed similarly in killing cells to a Visudyne-like formulation of VP. As the two formulations performed similarly, and considering shortages of Visudyne [173], we proceeded to evaluate the capacity of NanoVP alone as others have outlined the capacity of Visudyne to perform in a light-independent manner [121]. We observed a reduction of clonogenic capacity and motility in U251 GBM cells at sub-IC_{50} concentrations of the drug. While further work is needed to confirm that these changes to cellular behavior are YAP-dependent, these robust and promising functional findings are consistent with expanding literature that indicates light-independent VP may be a good therapeutic option. An important control in these studies was the inclusion of light-independent VP at a concentration of 0.25 μM, a low concentration of the drug that is efficacious for PDT. We observed no light-independent treatment effect in the 0.25 μM, indicating that current PDT practices with VP may not induce any light-independent effects, and a separate dosing regimen may be required. We then evaluated the combination of PDT with NanoVP treatment in a light-independent manner. In a clonogenic assay, where only viable U251 cells were replated post-PDT, we observed a significant decrease in clonogenic capacity in all groups that received PDT treatment. We did not observe a combinatorial effect in

U87 cells treated with a similar combination as measured *via* MTT assay, potentially because the mitochondrial activity of the PDT-treated cells [213] may have recovered by the time the assay was performed [214].

Others have commented on the potential to combine VP-PDT with light-independent effects of the drug [215] and have characterized the PDT response of GBM cells to complement studies on light-independent effects [216]. Some work has been done to evaluate the combinatorial effect of these two mechanisms [217], although it is missing the high daily dosing present in other studies evaluating the light-independent effects of VP [120, 121]. To our knowledge, this study presents the first combination of VP-PDT with light-independent VP with appropriate dosing to elicit both effects.

In the initial screen that found that VP interfered with YAP-TEAD interactions [118], PpIX and HPD were also reported disruptors. Due to the clinical interest in 5-ALA-induced PpIX for GBM [16] and historic applications of HPD as Photofrin, the first clinically used [218], we screened the ability of 5-ALA, PpIX, and HPD to modify GBM cell viability and clonogenic capacity. We found that all three formulations modified the activity of GBM cells. While further work is required to confirm that this is through YAP-TAZ/TEAD signaling, these initial results suggest that these other photosensitizers may have potential as light-independent agents.

Initial histological findings are consistent with reports the VP-PDT can permeabilize the BBB [111] through ABC transporter inhibition [113, 132, 214] and changes to gap junctions [110]. While preliminary, these exciting findings reveal the

first *in vivo* indication of functional permeabilization (fibrinogen delivery) with mechanistic explanations (ABC transporter and gap junction modifications).

4.5 Limitations

The PDT light dose selected for survival studies was based on a dose escalation study that did not evaluate damage to the neuropil. It is possible that, upon histological assessment, the light dose delivered to activate VP damages healthy brain stroma. Further studies characterizing safety are needed. Previous work found no damage to the neuropil using top-down illumination [111].

The orthotopic model used here better represents an inoperable primary or recurrent tumor, where the tumor is not resected before PDT. A resection model, as well as a better understanding of dosing requirements for eradication of infiltrative GBM cells, is needed.

For light-independent applications of VP, the YAP-TAZ dependence for U87 and U251 cells remains to be established. While this mechanism of the drug is well-established, effects may be more pronounced in a cell line that is dependent on YAP-TAZ-mediated signaling for migration and proliferation.

While the clonogenic data is promising, this combinatorial study was limited by the order in which VP-PDT and light-independent VP were applied and by the system and assays used. The concentrations of VP for light-independent effects were an order of magnitude higher than for PDT. We only performed PDT before providing enough VP for light-independent effects to avoid over-sensitizing cells to light. As such, we were unable to assess the potential of light-independent application of VP to sensitize cells to PDT. Further combinatorial studies, including expanded duration of

light-independent VP exposure and order of VP-PDT and light independent VP exposure (e.g., light-independent effects then PDT, or light-independent then PDT then light-independent again) are worth exploring. Results in this study also indicated the VP poorly penetrates the brain. It is worth considering that PDT-mediated BBB permeabilization [111] may enhance delivery of VP to the brain to enable enhanced light-independent effects. As such, biodistribution studies after BBB permeabilization as well as transwell assay models of permeabilization [110] may also inform combination of PDT and light-independent applications of VP.

The histological study performed here, while exciting, is preliminary. Most groups are underpowered and some important controls (e.g. non-tumor bearing intact brain and PDT but no tumor) need to be included to reach sound conclusions from the data.

4.6 Conclusions

This chapter demonstrates that NanoVP-PDT provides some survival benefit, likely through tumor debulking, and is more efficacious than other photosensitizer formulations, likely due to increased intracellular accumulation of the drug.

These results surrounding the light-independent application of NanoVP are consistent with other reports that VP is cytotoxic and inhibits cell motility [120, 122]. The combination of PDT with NanoVP and the light-independent effects of NanoVP shows some slight combinatorial effect; however, combining PDT *in vivo* for BBB or BTB permeabilization [111] to enhance VP delivery to the brain and subsequently enhance light-independent effects may hold promise. Additionally, evaluation of cell lines dependent on YAP-mediated signaling, particularly glioma stem-like cells [119],

may show greater efficacy than the studies shown here. In all, NanoVP represents an attractive option for clinical delivery of a hydrophobic drug, especially considering current interest in repurposing VP for light-independent applications.

Chapter 5: Towards Application of NanoVP Photodynamic Therapy Blood-Brain Barrier Permeabilization in a Zebrafish Model[*]

5.1 Introduction

The most difficult to treat cells in GBM are the cells that have invaded beyond the tumor boundary. These are impossible to track in patients or in experimental rodents even with bioluminescent reporting systems (**Figure 4-7**), and require histological evaluation, which is time consuming and does not show kinetic growth of the tumor. Zebrafish (*Danio rerio*), on the other hand, are an attractive experimental model for cancer [219, 220] due to their size and the ability to image implanted tumor cells through the organism to track tumor growth in real-time and even in high-throughput manners [221-223]. Injection of GBM cells into the brains of zebrafish would permit visualization of both modifications to GBM cell behavior after light-independent treatment with NanoVP (**Figure 4-8, Figure 4-9, Figure 4-10**) as well as higher-throughput evaluation of BBB permeabilization [111]. This analysis is enabled by high levels of homology between the human and zebrafish BBB.

BBB endothelial cells express ABC transporters on the luminal membrane that redirect toxins and therapeutics back into the bloodstream [83]. ABC transporters

[*] This chapter was adapted from Quinlan JA**,** Sabbeneni S, Robey RW, Lipsey CC, Inglut CT, Thomas JR, Walker JR, Zhou W, Huang HC, Gottesman MM. Identification of NanoLuciferase substrates transported by human ABCB1 and ABCG2 and their zebrafish homologs at the blood-brain barrier. *Molecular Pharmacology.* 2024. doi: 10.1124/molpharm.123.000811.Permission was obtained from the publisher to use this material in the current dissertation.

transport a wide range of substances against their concentration gradient *via* ATP hydrolysis [83]. Two of the highly expressed ABC transporters at the human BBB are ABCB1 and ABCG2. The BBB is thus a major hurdle when delivering therapeutics to the brain [85].

The role of P-gp and ABCG2 in limiting drug penetration to the brain has been repeatedly demonstrated in mouse models. Deletion of the *Abcb1a* gene in mice resulted in a 20-fold increase in brain vincristine levels compared to wild-type mice [224]. Deletion of murine *Abcb1a* and *Abcb1b*, *Abcg2*, or all genes at the same time has suggested cooperativity between the two transporters in keeping substrates out of the brain [225, 226]. While several *in vitro* models have been used to model the role of transporters at the BBB, they are often incomplete, lacking components of the NVU, while murine and large *in vivo* models are expensive to maintain and are not amenable to high-throughput screening [87]. Thus, improved model systems to identify strategies to increase drug delivery to the brain are needed.

The zebrafish has emerged as a comparable model to rodents for elucidating the role of transporters at the BBB [89, 90]. Like humans, zebrafish have a functioning BBB comprised of endothelial cells that form tight junction complexes *via* claudin-5 and ZO-1 that physically limit drug entry into the brain [91]. Our group has recently characterized the different zebrafish homologs of human ABCB1 and ABCG2 and demonstrated that Abcb4 [95] and Abcg2a [94] have a substrate and inhibitor profile similar to those of their respective human equivalents and are expressed at the zebrafish BBB. With these functional similarities to the human BBB, and considering the

potential for high throughput assays using zebrafish, they are a logical choice for a high-throughput model of the BBB [96].

We previously utilized a mouse model in which firefly luciferase, under the control of the GFAP promoter, was expressed exclusively in astrocytes protected by the BBB, permitting examination of ABC transporter activity [227]. Because the firefly luciferase substrate D-luciferin is transported by ABCG2, bioluminescent signal is increased only when ABCG2 is inhibited or the physical BBB is disrupted, allowing examination of ABCG2 function at the BBB [227]. Given the similarity in BBB characteristics, we are developing an analogous model in the zebrafish which has some practical advantages. Recent advances in luminescence assays have resulted in the development of NanoLuc, a brighter alternative to firefly luciferase [228, 229] The native substrate, coelenterazine, has been modified to yield substrates with even brighter light intensity [230-232]. To evaluate the feasibility of a zebrafish-based BBB integrity model with a bioluminescent read-out, we evaluated whether human and zebrafish transporters expressed at the BBB can transport NanoLuc substrates using a cell-based model. Previous work had shown that coelenterazine was transported by both ABCB1 and ABCG2 [233], but it was not known whether furimazine or other coelenterazine analogs could be transported by human or zebrafish transporters. Here, we transfect human *ABCB1* and *ABCG2*, and the zebrafish homologs *abcb4* and *abcg2a*, as well as NanoLuciferase into HEK293 cells in an exploratory effort to determine which NanoLuc substrates are transported. The development of this cell-based model and potential zebrafish model could lead to the discovery of compounds that increase the permeability of the BBB *via* novel mechanisms.

To characterize NanoLuc substrate specificity with human ABCB1 and ABCG2, and their zebrafish homologs, Abcb4 and Abcg2a, HEK293 cells expressing these transporters were also transfected with NanoLuc (**Figure 5-1**). In this system, inhibition of a given transporter results in increased intracellular accumulation of the NanoLuc substrate of interest. This increased NanoLuc concentration leads to increased luminescence, which is quantifiable *via* plate reader.

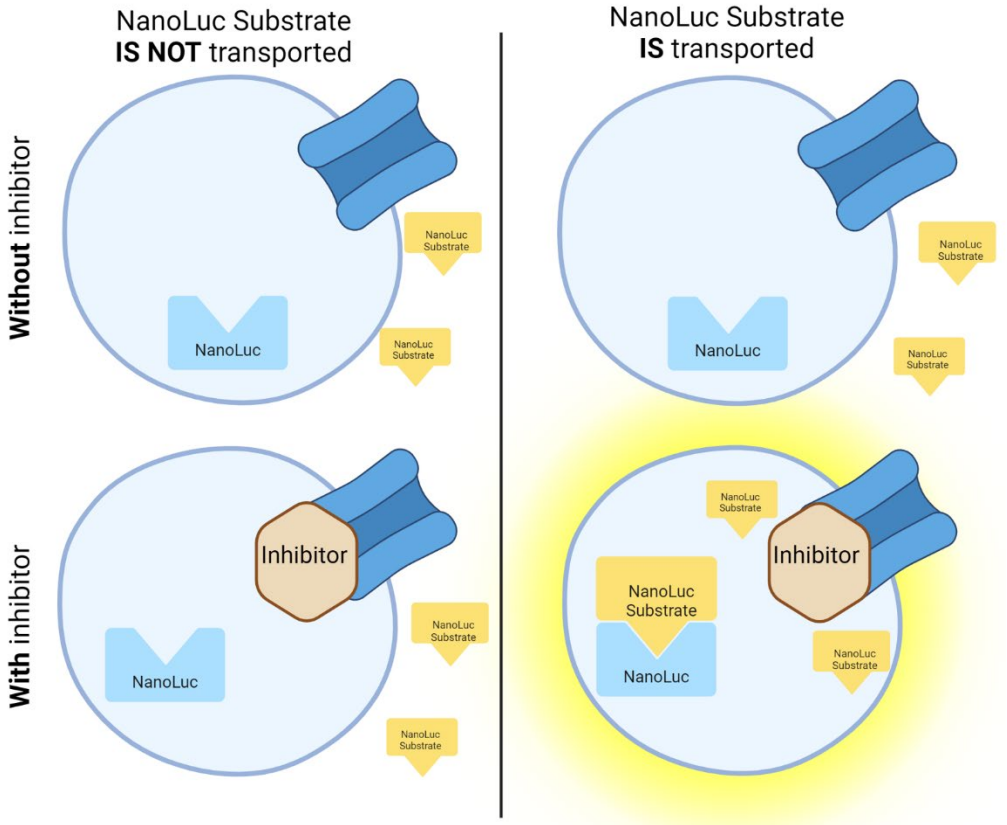

Figure 5-1. Schematic of bioluminescent readout for NanoLuc substrate transport status. If a NanoLuc substrate is not a transporter substrate (left), the molecule remains within the cell and the bioluminescent signal is the same with and without a transporter inhibitor. If the NanoLuc substrate is a transporter substrate (right), bioluminescent signal is increased in the presence of a transporter inhibitor. Made with Biorender.com.

5.2 Methods

5.2.1 Chemicals

Doxorubicin was purchased from Sigma-Aldrich (St. Louis, MO). THZ1 ((E)-N-(3-((5-chloro-4-(1H-indol-3-yl)pyrimidin-2-yl)amino)phenyl)-4-(4-(dimethylamino)but-2-enamido)benzamide) and Ko143 (tert-butyl 3-((3R,6S,12aR)-6-isobutyl-9-methoxy-1,4-dioxo-1,2,3,4,6,7,12,12a-octahydropyrazino[1',2':1,6]pyrido[3,4-b]indol-3-yl)propanoate) were obtained from Cayman Chemical (Ann Arbor, MI). Elacridar was purchased from Selleck chemicals (Houston, TX). Furimazine was purchased from Aobious (Gloucester, MA), coelenterazine and coelenterazine analogues) were purchased from Biotium (Fremont, CA). Polyethyleneimine (PEI) was purchased from Polysciences, Inc (Warrington, PA). Flourofurimazine, cephalofurimazine, 6400, 6403, 8122, and 8129 were provided by Promega (Madison, WI). Furimazine was resuspended in dimethyl sulfoxide and all other substrates were resuspended in methanol. All suspensions were then stored in single-use aliquots in the dark at -20°C.

5.2.2 Cell Culture

HEK293 cells (ATCC, Manassas, VA, Research Resource Identifier (RRID): CVCL_0045) were transfected with empty pcDNA3.1 vector or with vector containing full-length *abcb4* or *abcg2a* (Genscript, Piscataway, NJ) flanked by a FLAG tag, as previously reported [94, 95]. The MDR-19 and R5 cell lines were generated from HEK293 cells transfected with full-length human *ABCB1* or *ABCG2* and have been previously characterized [234]. Cells expressing the transporters were additionally

transfected with a plasmid coding for NanoLuc (N1411, Promega, Madison, WI) and selected with 40 μg/ml hygromycin B (InvivoGen, San Diego, CA). Empty vector-transfected (EV) cells served as a negative control. Transfected cells were grown in EMEM medium (Mediatech, Manassas, VA) and were maintained in 2 mg/ml G418 (Mediatech) and 40 μg/ml hygromycin B. Clones expressing similar levels of NanoLuc were selected based on expression as detected by immunoblot. Cells were routinely monitored for potential mycoplasma contamination using Lonza MycoAlet PLUS Mycoplasma Detection Kit (cat. # LT07-710). Mycoplasma testing was performed 72 hours after cells were split and allowed to grow to 70-80% confluence in a 37°C 5% CO_2 incubator.

5.2.3 Substrate Screening

Opaque white 96-well plates were coated with PEI (0.025 mg/mL) for 20 minutes at room temperature to aid in cell adhesion. Transfected HEK293 cells were plated at a density of 31,250 cells/cm^2. The next day, one of the ABC inhibitors (3 μM elacridar for ABCB1 & Abcb4; 5 μM Ko143 for ABCG2 & Abcg2a) or complete media was added to wells in quintuplicate and incubated for 30 minutes at 37 °C. Furimazine and its analogs, coelenterazine, or coelenterazine analogs, were subsequently added to the cells at a working solution of 470 nM for 1 minute at room temperature. Medium containing ABC transporter inhibitors and NanoLuc substrates was removed and replaced with fresh cell culture medium. After a 1-minute stabilization period, luminescence was measured on a microplate reader, every minute, for a total of 5 measurements. The brightness of the NanoLuc substrates was measured in EV cells in a similar manner, without the removal of the substrates.

5.2.3 Zebrafish Embryo Incubation with NanoVP

All zebrafish experimentation were performed under NCI-Bethesda Animal Care and Use committee-approved protocol LCB-033-2-F. Four days post fertilization (dpf) TAB5 zebrafish embryos were incubated with 0-10 μM NanoVP in Instant Ocean for 90 minutes or 24 hours. At 0, 1.5, 24, 48, and 72 hours, embryo viability as confirmed by response to eyelash touch and/or visible heartbeat. Developmental abnormalities were noted when appropriate. For imaging, embryos were anesthetized with 0.1% tricaine and imaged on a brightfield microscope.

5.2.5 Statistics

This study was not designed to test a prespecified statistical null hypothesis and should be considered exploratory. As such, P-values should be interpreted as descriptive. AUC was calculated by taking the brightness values (counts per second) recorded every minute for five minutes and time (0-5 minutes at 1-minute intervals) input into GraphPad Prism. GraphPad Prism 10 was used to determine AUC values, median growth inhibitory (GI_{50}) values, and visualization. Microsoft Excel was used to determine p-values from one-way Students' t-tests, as well as median and confidence intervals from GI_{50} values. A one-tailed t-test was selected to analyze differences in area under the curve as we hypothesized that inhibition of signal should result in only an increase in signal. Specific tests, number of repeats, and significance thresholds are indicated in the figure captions.

5.3 Results

5.3.1 Brightness of Coelenterazine and Furimazine Analogs

The zebrafish larval brain at 5 days post fertilization is only 700 μm in length and 500 μm in thickness [235, 236]. To identify NanoLuc substrates that may provide maximal sensitivity in the zebrafish model, we evaluated the brightness of a panel of NanoLuc substrates in EV cells. Briefly, cells were treated with the substrate of interest (470 nM) for one minute, then bioluminescence was read every minute for five minutes without removing the substrate of interest from cell culture. The area under the curve (AUC) was calculated using the resulting bioluminescence versus time data. Furimazine, the substrate specifically developed to react with NanoLuc, produced a signal 22 times that of native coelenterazine (**Figure 5-2**). Eleven substrates (furimazine, cephalofurimazine, 8122, 8129, flourofurimazine, coelenterazine-f, coelenterazine-h, 6403, coelenterazine-fcp, coelenterazine-hcp, and coelenterazine-n) produced bioluminescence signals higher than that of native coelenterazine, while four substrates (coelenterazine-i, coelenterazine-cp, 6400, and coelenterazine-ip) produced signal dimmer than native coelenterazine.

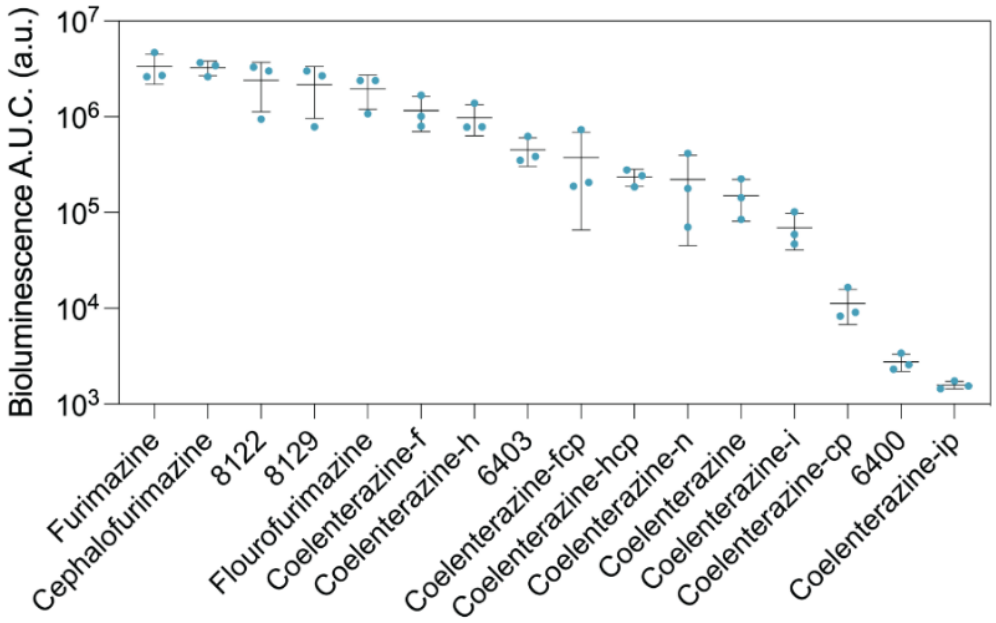

Figure 5-2. Bioluminescent signal from NanoLuc substrates in empty vector cells. AUC was calculated using bioluminescent signal versus time (minutes) read every minute for five minutes while cells were incubated with the NanoLuc substrate of interest. Data presented as mean ± SD with 3 biological replicates per group.[*]

[*] This figure was first published in Quinlan JA**,** Sabbeneni S, Robey RW, Lipsey CC, Inglut CT, Thomas JR, Walker JR, Zhou W, Huang HC, Gottesman MM. Identification of NanoLuciferase substrates transported by human ABCB1 and ABCG2 and their zebrafish homologs at the blood-brain barrier. *Molecular Pharmacology.* 2024. doi: 10.1124/molpharm.123.000811.

5.3.2 Transporter Status of NanoLuc Substrates by Area Under the Curve

Next, we determined whether NanoLuc substrates are also substrates for ABC transporters, screening all available substrates for transport status (**Figure 5-2**). Cells were incubated with inhibitor for 30 minutes (3 μM elacridar for ABCB1 and Abcb4; 5 μM Ko143 for ABCG2 and Abcg2a), then NanoLuc substrate (470 nM) for one minute before media was refreshed and bioluminescent signal was read. The bioluminescence signal was measured every minute over a 5-minute period and the area under the curve (AUC) was calculated (**Figure 5-3**). By one-tailed Student's t-test, there was a significant increase in AUC for ABCB1-expressing cells treated with flourofurimazine, coelenterazine-f, coelenterazine-h, coelenterazine-fcp, coelenterazine-n, native coelenterazine, coelenterazine-i, and coelenterazine-cp (**Figure 5-3E, 5-3F, 5-3G, 5-3I, 5-3K, 5-3L, 5-3M, 5-3N**). For Abcb4-expressing cells, we observed a significant increase in AUC for coelenterazine-h, coelenterazine-fcp, coelenterazine-n, native coelenterazine, coelenterazine-i, and coelenterazine-cp (**Figure 5-3G, 5-3I, 5-3K, 5-3L, 5-3M, 5-3N**). There was a significant increase in AUC from ABCG2-expressing cells treated with furimazine, 8122, 6403, coelenterazine-n, native coelenterazine, coelenterazine-cp, and 6400 (**Figure 5-3A, 5-3C, 5-3H, 5-3K, 5-3L, 5-3N, 5-3O**). There were significant increases in AUC from Abcg2a-expressing cells treated with 8122, 6403, coelenterazine-n, coelenterazine-i, coelenterazine-cp, 6400, and coelenterazine-ip (**Figure 5-3C, 5-3H, 5-3K, 5-3M, 5-3N, 5-3O, 5-3P).**

Native coelenterazine was previously determined to be a substrate for both human ABCG2 and ABCB1 [233] and we found that it was transported by both

ABCB1, ABCG2, and Abcb4 (**Figure 5-3L**), as the bioluminescent signal was significantly higher in the presence of an ABC transporter inhibitor compared to the absence of inhibitor. Furimazine, which produced the highest bioluminescence signal in EV cells, was determined to be a substrate of ABCG2 (**Figure 5-3A)**. The relative AUC and residual luminescence are summarized in **Figure 5-5**.

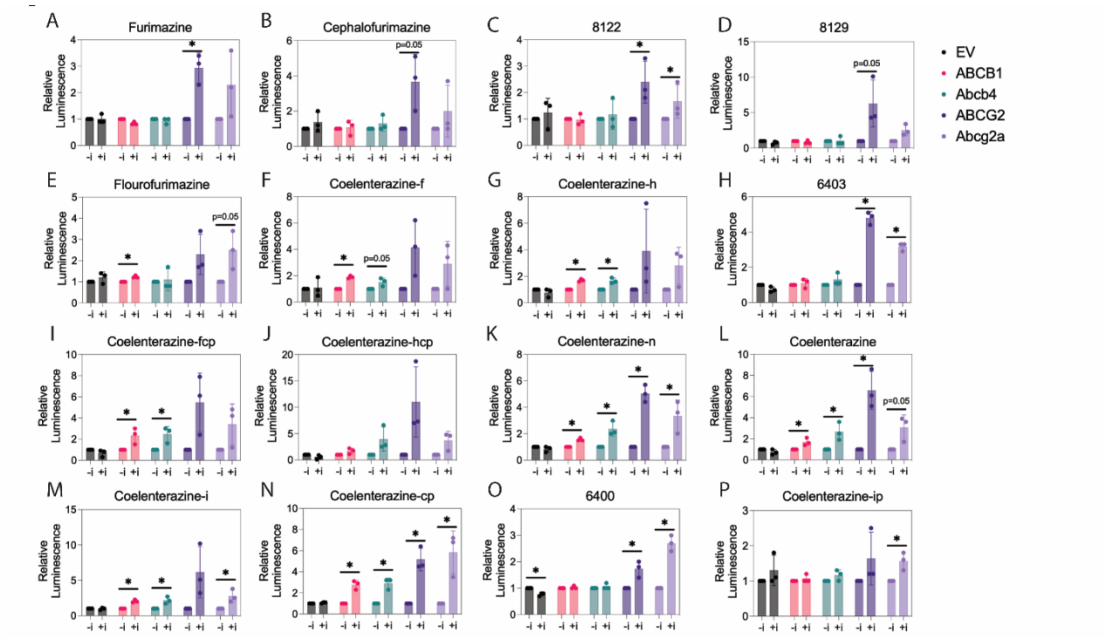

Figure 5-3. Area under the curve values from bioluminescence versus time with (+ i) and without (- i) ABC transporter inhibitors permit identification of ABC transporter substrates. HEK293 cells transfected with the transporter of interest and NanoLuciferase were incubated with inhibitor (elacridar (3 µM) for ABCB1 and Abcb4; Ko143 (5 µM) for ABCG2 and Abcg2a) for 30 minutes before introduction of the NanoLuc substrate (470 nM) for 1 minute. Bioluminescence was measured every minute for five minutes after the media were refreshed. AUC of bioluminescence versus time graphs are shown for uninhibited (- i) and inhibited (+i) (**A**) furimazine, (**B**) cephalofurimazine, (**C**) 8122, (**D**) 8129, (**E**) flourofurimazine, (**F**) coelenterazine-f, (**G**) coelenterazine-h, (**H**) 6403, (**I**) coelenterazine-fcp, (**J**) coelenterazine-hcp, (**K**) coelenterazine-n, (**L**) coelenterazine, (**M**) coelenterazine-i, (**N**) coelenterazine-cp, (**O**) 6400, and (**P**) coelenterazine-ip in a panel of transfected HEK293 cells. Graphs show mean ± SD of bioluminescent AUC normalized to each replicate's uninhibited condition. Inhibited values are normalized to each replicate's uninhibited control. Data represents three biological replicates of all substrates. By one-tailed Student's t-test, * indicates $p<0.05$.[*]

[*] This figure was first published in Quinlan JA**,** Sabbeneni S, Robey RW, Lipsey CC, Inglut CT, Thomas JR, Walker JR, Zhou W, Huang HC, Gottesman MM. Identification of NanoLuciferase substrates transported by human ABCB1 and ABCG2 and their zebrafish homologs at the blood-brain barrier. *Molecular Pharmacology.* 2024. doi: 10.1124/molpharm.123.000811.

5.3.3 Degree of Efflux of NanoLuc Substrates

Foreseeing potential sensitivity issues with our zebrafish model of the BBB, we also aimed to determine the degree to which various NanoLuc substrates were effluxed. A substrate that is a good NanoLuc substrate (i.e., produces a large bioluminescent signal) but a poor ABC transporter substrate (i.e., is not effluxed to a high degree) may lower the specificity of the *in vivo* model. To evaluate this possibility, we looked at the luminescence ratio between cells with inhibited transporters and cells with uninhibited transporters after five minutes of efflux. We set a threshold of 1.5-fold increase in residual luminescent signal as detectable efflux as this was above the mean residual luminescence ratio observed in any EV cells (**Figure 5-4**). By this measure, poor substrates have a low ratio (<1.5), while substrates that are highly effluxed will have a larger ratio (>1.5) (**Figure 5-4**). In ABCB1-expressing cells, we saw endpoint luminescence ratios above the threshold with coelenterazine-f, coelenterazine-h, coelenterazine-fcp, coelenterazine-i, and coelenterazine-cp (**Figure 5-4F, 5-4G, 5-4I, 5-4M, 5-4N**). In Abcb4-expressing cells, we saw endpoint luminescence ratios above the threshold with coelenterazine-h, coelenterazine-fcp, coelenterazine-hcp, coelenterazine-n, native coelenterazine, coelenterazine-i, and coelenterazine-cp (**Figure 5-4G, 5-4I, 5-4J, 5-4K, 5-4L, 5-4M, 5-4N**). In ABCG2 expressing cells, endpoint luminescence was above threshold for all substrates (**Figure 5-4**). In Abcg2a-expressing cells, endpoint luminescence was above the threshold for all substrates except coelenterazine-ip (**Figure 5-4P**).

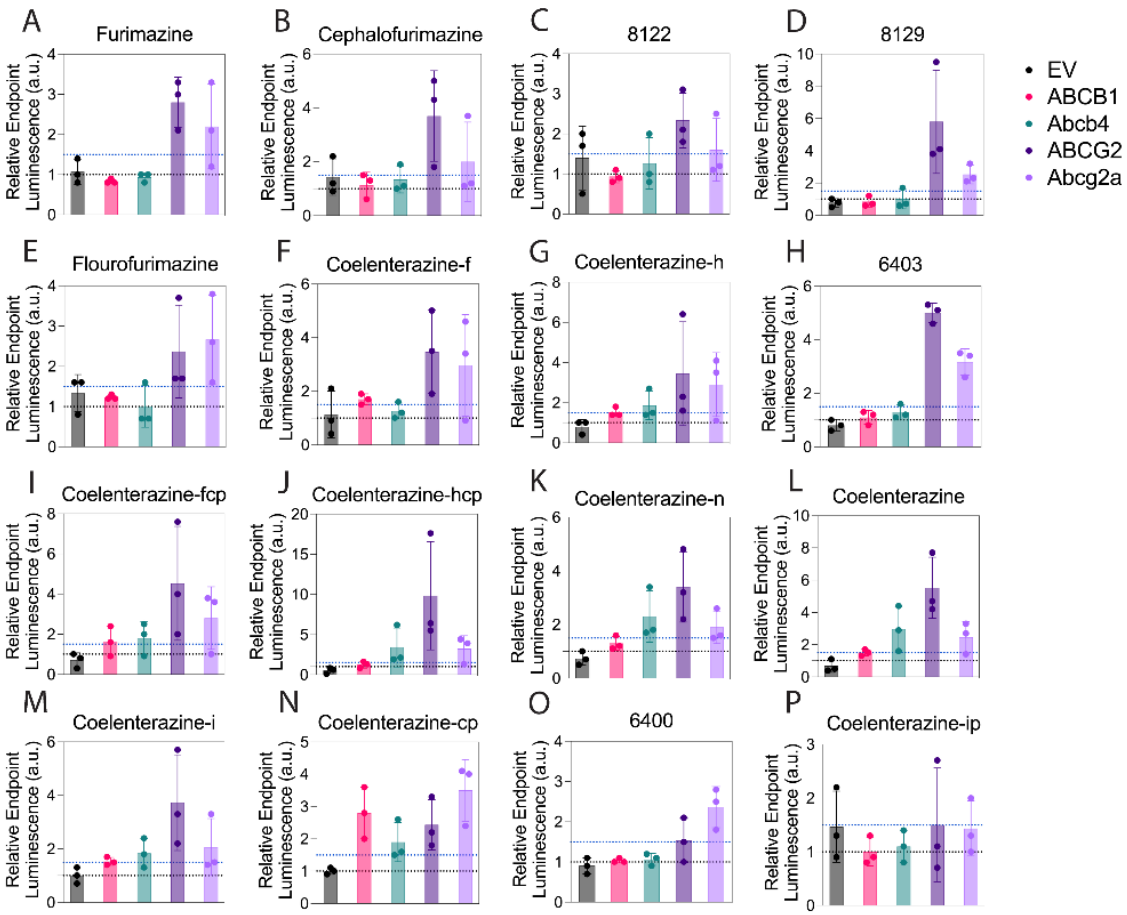

Figure 5-4. Percent increase in residual luminescence. Measurements taken after five minutes of efflux for cells treated or not treated with ABC transporter inhibitors (for ABCG2 and Abcg2a, Ko143, 5 µM; for ABCB1 and Abcb4, elacridar, 3 µM; 470 nM NanoLuc substrate of interest) for (**A**) furimazine, (**B**) cephalofurimazine, (**C**) 8122, (**D**) 8129, (**E**) flourofurimazine, (**F**) coelenterazine-f, (**G**) coelenterazine-h, (**H**) 6403, (**I**) coelenterazine-fcp, (**J**) coelenterazine-hcp, (**K**) coelenterazine-n, (**L**) coelenterazine, (**M**) coelenterazine-i, (**N**) coelenterazine-cp, (**O**) 6400, and (**P**) coelenterazine-ip. Larger values indicate a more strongly effluxed substrate. Data presented as mean ± SD of luminescence at 5 minutes in the inhibited condition divided by luminescence at 5 minutes in the uninhibited condition. Data represents 3 biological replicates of all substrates. The black dashed line at 1 indicates the level at which luminescence from inhibited and uninhibited samples were equal. The line at 1.5 indicates the threshold set to indicate a detectable difference in future experiments.[*]

[*] This figure was first published in Quinlan JA**,** Sabbeneni S, Robey RW, Lipsey CC, Inglut CT, Thomas JR, Walker JR, Zhou W, Huang HC, Gottesman MM. Identification of NanoLuciferase substrates transported by human ABCB1 and ABCG2 and their zebrafish homologs at the blood-brain barrier. *Molecular Pharmacology.* 2024. doi: 10.1124/molpharm.123.000811.

5.3.4 Summary of Substrate Efflux

The individual measures in **Figure 5-3** and **Figure 5-4** provide some insights into the efflux of NanoLuciferase substrates by human and zebrafish ABC transporters, but the kinetics of efflux are complex. The suitability of a particular transporter to efflux a particular substrate may be best understood by comparing these two measures. When fold-changes in luminescence and in endpoint luminescence are combined in a heat map, we see clear trends, where certain substrates are highly effluxed by multiple transporters in both assays (for example, coelenterazine-hcp and coelenterazine-cp, **Figure 5-5A, 5-5B**). It also becomes clear that ABCG2 effluxes the most substrates to a very high degree, and that zebrafish homolog Abcg2a follows this trend (**Figure 5-5A, 5-5B**). In some cases, we see that high AUC luminescence may still be coupled with efficient transport over a 5-minute period. In the case of coelenterazine-i in Abcb4 and coelenterazine-n in Abcg2a, we see high fold-increases for luminescent AUC (**Figure 5-5A**), but minimal change for endpoint luminescence (**Figure 5-5B**). This may indicate that the inhibitor competitively blocks efflux to an appreciable degree, but that the substrate is still effluxed. Alternatively, this may highlight a lack of stability of the given substrate over a 5-minute period.

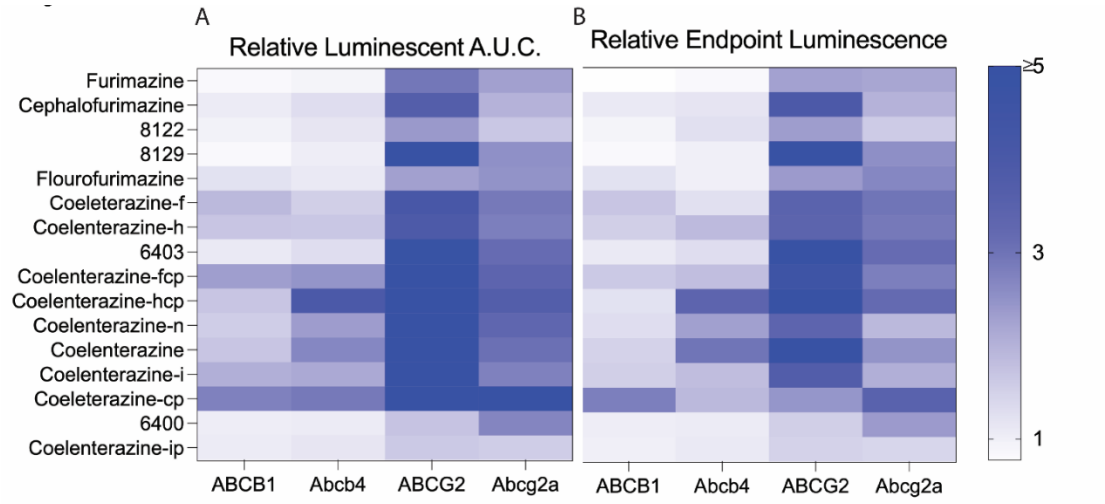

Figure 5-5. Summary of efflux transporter status of various NanoLuciferase substrates, shown as fold-change. Heat maps show (A) relative A.U.C. on a time versus luminescence curve for inhibited conditions versus uninhibited conditions and (B) relative residual luminescence after five minutes of efflux in inhibited cells versus uninhibited cells, revealing 1-fold to 11-fold greater luminescence for some substrate-transporter pairs. Data is representative of 3 biological replicates.[*]

[*] This figure was first published in Quinlan JA**,** Sabbeneni S, Robey RW, Lipsey CC, Inglut CT, Thomas JR, Walker JR, Zhou W, Huang HC, Gottesman MM. Identification of NanoLuciferase substrates transported by human ABCB1 and ABCG2 and their zebrafish homologs at the blood-brain barrier. *Molecular Pharmacology.* 2024. doi: 10.1124/molpharm.123.000811.

5.3.5 Viability of Larval Zebrafish in NanoVP

The ultimate goal of this portion of the thesis is to support the development of a zebrafish model of GBM and of the BBB to evaluate PDT-mediated BBB permeabilization as well as efficacy of light-dependent and light-independent NanoVP treatment against individual GBM cells. As a first step, we evaluated tolerability of NanoVP by embryonic zebrafish. TAB5 zebrafish embryos (4 dpf) were incubated with NanoVP in Instant Ocean for either 90 minutes or 24 hours, then transferred to fresh Instant Ocean. Water was changed every 24 hours out to 72 hours (7 dpf). Evaluation of viability (e.g., observation of a beating heart and responsiveness to eyelash touch) revealed no significant time- or concentration-dependent increase after treatment with up to 10 μM NanoVP after 90 minutes (**Figure 5-6A**) or 24 hours (**Figure 5-6B**). We also observed abnormalities in development, including unresponsiveness to eyelash touch, bent tail, cardiac effusion, or underdevelopment. Once again, we found no significant dose- or time-dependent increase in abnormal development after 90 minutes (**Figure 5-7A**) or 24 hours (**Figure 5-7B**) of NanoVP exposure. While many fish developed normally, (**Figure 5-8A, Figure 5-8B**), some developed pericardial effusion (**Figure 5-8C, Figure 5-8D**). bent tails (**Figure 5-8E**), or did not develop at the appropriate rate (**Figure 5-8F**) [237].

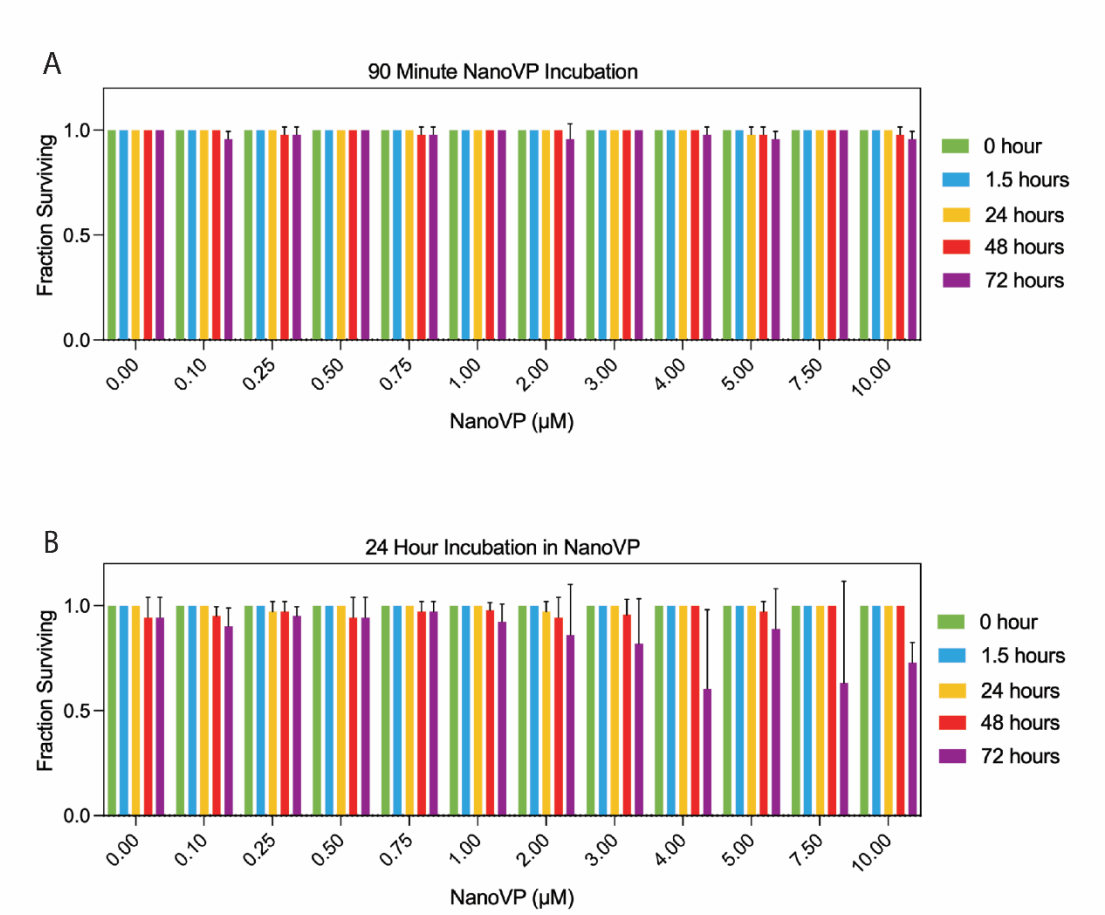

Figure 5-6. Fraction of embryonic zebrafish surviving light-independent NanoVP exposure. Four dpf TAB5 zebrafish (16 per group, 3 groups per concentration) were incubated with NanoVP for either (A) 90 minutes or (B) 24 hours before transfer to fresh Instant Ocean. Fish were assessed for viability by observation of heartbeat and response to eyelash touch at 0, 1.5, 24, 48, and 72 hours. Data represents mean ± SD. No significance was observed by two-way ANOVA.

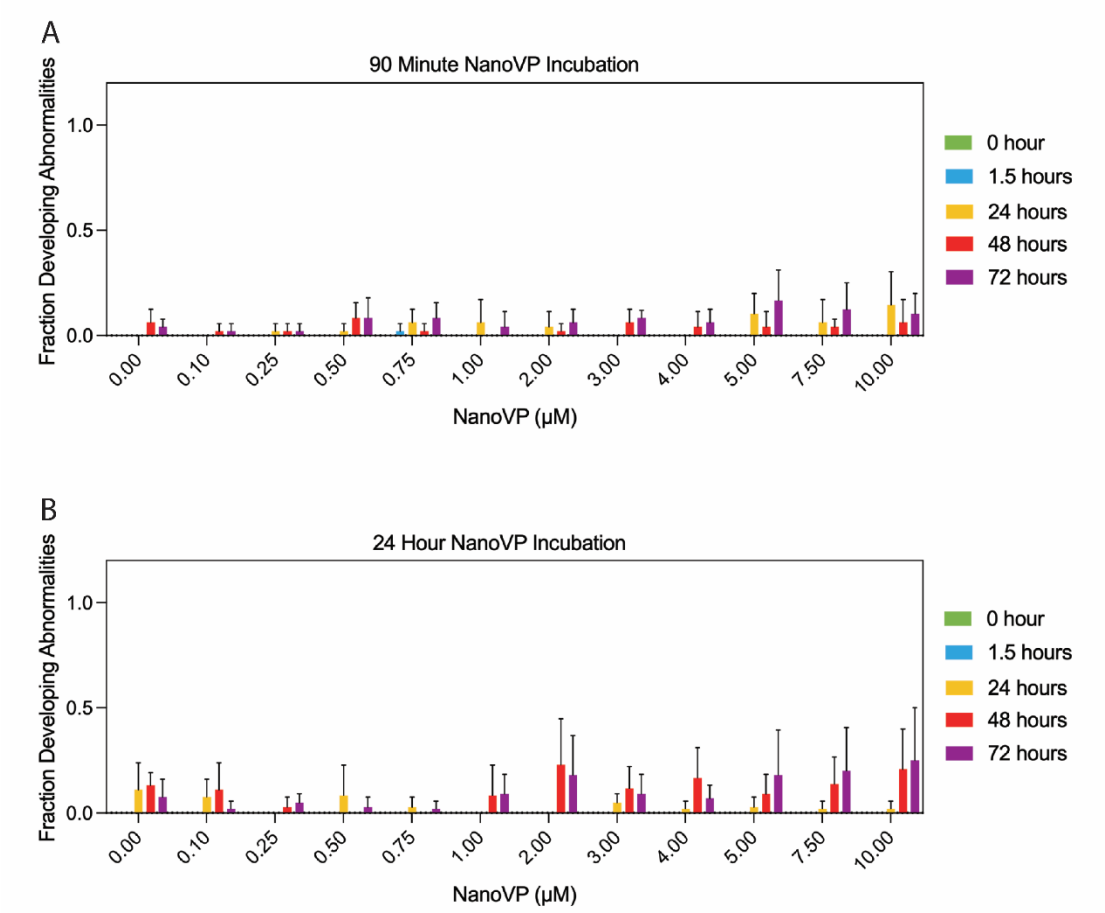

Figure 5-7. Fraction of embryonic zebrafish developing abnormalities after exposure to NanoVP. Four dpf TAB5 zebrafish (16 per group, 3 groups per concentration) were incubated with NanoVP for either (A) 90 minutes or (B) 24 hours before transfer to fresh Instant Ocean. Fish were assessed for normal development by observation at 0, 1.5, 24, 48, and 72 hours. Abnormal development included bent tails, lack of responsiveness to eyelash touch, cardiac effusion, and underdevelopment. Data represents mean ± SD. No significance was observed by two-way ANOVA.

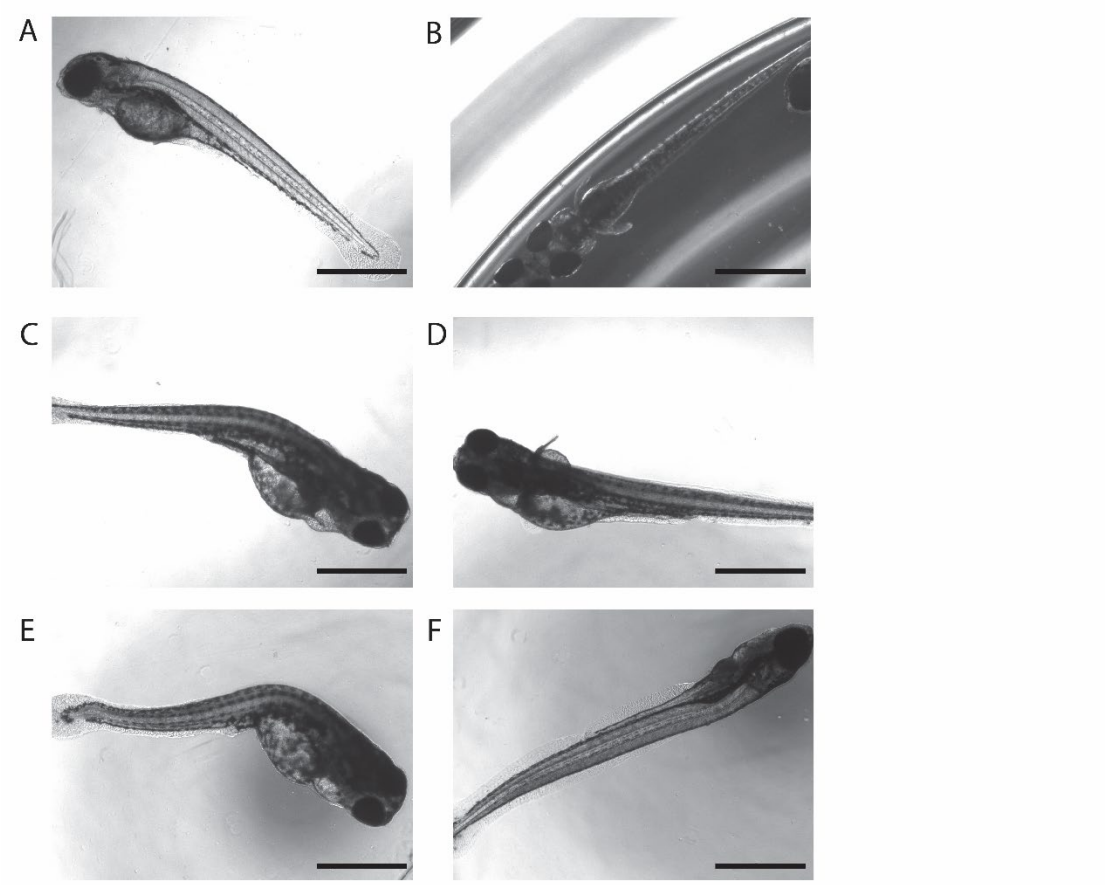

Figure 5-8. Sample images of normal and abnormal embryonic zebrafish. At 4 dpf, TAB5 zebrafish treated with 0 µM NanoVP had normal development as seen by (A) lateral and (B) top view. Samples of pericardial effusion in (C) 5 µM- and (D) 10 µM-treated fish after 24 hours of incubation with NanoVP (embryos are 5 dpf). (E) An embryo with a bent tail and pericardial effusion after 24 hours of treatment with 4 µM NanoVP. (F) An embryo 24 hours after media change after treatment with 10 µM NanoVP for 24 hours was underdeveloped. In all images, scale bar is 750 µm.

5.4 Discussion

The BBB remains a major obstacle to the management of diseases of the central nervous system [238], as most therapeutics cannot effectively enter the brain on their own because of the intact BBB [239]. BBB endothelial cell tight junctions [240] and apical ABC transporters ABCB1 and ABCG2 prevent access to the brain [241] for a number of chemotherapies and targeted therapies [242-244]. While approaches such as focused ultrasound show promise for improving drug delivery across the BBB [245, 246], ABC transporters may still remain a barrier to drug transport even after BBB physical integrity is compromised [247-249]. This challenge underscores the need to identify methodology to disrupt the BBB and ensure inactivation of ABC transporters for maximal drug delivery to the neuropil.

Our goal is to establish a zebrafish model of the BBB to screen for potential BBB disruptors in which introduction of a chemical disruptor permits entry of a NanoLuc substrate into the zebrafish brain by disrupting endothelial cells and/or inhibiting ABC transporters at the BBB. This study supports these efforts by characterizing the brightness, substrate status, and the degree to which various substrates were effluxed. We identified eleven substrates brighter than native coelenterazine (furimazine, cephalofurimazine, 8122, 8129, flourofurimazine, coelenterazine-f, coelenterazine-h, 6403, coelenterazine-fcp, coelenterazine-hcp, coelenterazine-n) when reacted with NanoLuc. This informs substrate choice in the zebrafish model, enabling selection of the substrate most likely to give a strong signal to enhance sensitivity. Understanding which ABC transporter substrates are transported permits deeper probing into potential mechanisms of action of BBB disruptors, as use

of specific NanoLuc substrates in the zebrafish model will elucidate the impact of BBB disruptors on specific ABC transporters. Screening experiments revealed that several NanoLuc substrates tested were also substrates for human ABCB1, zebrafish Abcb4, human ABCG2, and zebrafish Abcg2a. Generally, zebrafish homologs performed similarly to their human counterparts, with a few minor discrepancies between ABCB1 and Abcb4 (e.g. flourofurimazine). There were more discrepancies between ABCG2 and Abcg2a (furimazine, coelenterazine-i, coelenterazine-ip) when evaluated with the statistical cutoff of $p<0.05$. This varied ABC transporter substrate status profile of different NanoLuc substrates may permit probing of the role that individual transporters play at the BBB. Finally, understanding the degree to which ABC transporters efflux NanoLuc substrates may influence substrate choice. More efficiently effluxed substrates, as measured by residual luminescence after 5 minutes of efflux, may further allow for greater specificity of the assay, supporting the use of substrates with lower brightness but different transporter status profiles.

The difference in transporter substrate status of NanoLuc substrates between human and zebrafish homologs may be in part attributable to slight differences in the amino acid residues in the ABC transporter substrate binding pocket. In this study, we found differences in substrate specificity profiles between ABCG2 and Abcg2a. Our recent study indicates that Abcg2a is a zebrafish homolog correlated with ABCG2 in terms of both substrate specificity and localization of expression. We also found that ABCG2 and Abcg2a, while functionally similar, are only 61.4% homologous in amino acid sequence [94]. While further evaluation of the similarity between Abcg2a-d and ABCG2 binding pockets is warranted, the differences in substrate specificity found

here are likely attributable to slight differences in amino acid residues in the transporter binding pocket.

Native coelenterazine and its analogs contain an imidazopyrazinone core, a nitrogen-bearing heterocycle, and three side groups [230]. Although there are only slight differences within the side groups corresponding to different amino acid side chains, the ABC transporter substrate status of these molecules varied greatly. Challenges in connecting molecular features to ABC transporter substrate status have been longstanding [250] and any given *in vitro* screening paradigm has limitations that make meaningful extrapolation difficult [250, 251]. Currently, machine learning approaches appear promising to predict compound-transporter interactions, but these models often require training sets much larger than the panel screened here. Recent reports have identified two furimazine analogs capable of penetrating the BBB, flourofurimazine and cephalofurimazine, enabling enhanced imaging in the brain [231, 232]. Our findings here indicate that these compounds may be substrates of transporters present at the BBB (ABCB1 for flourofurimazine and ABCG2 for cephalofurimazine), indicating that their bioavailability in the brain may be due to an alternate mechanism.

Finally, preliminary work with embryonic zebrafish found that NanoVP is fairly well tolerated by the developing fish. This provides a foundation for future work where tumors may be implanted in fish before PDT or light-independent NanoVP therapy, or use of the bioluminescent BBB model to evaluate PDT-mediated BBB permeabilization.

5.5 Limitations

This study provides a background to support a zebrafish model of the BBB that is in development. We acknowledge that the translation of these findings from cell-based assays to zebrafish studies will require further workup, as stability of the molecule under zebrafish treatment conditions, pharmacokinetics within the zebrafish, the presence of ABC transporters in other parts of the body beyond the BBB, and other components of the NVU may all impact ultimate luminescence readout in the brain. Future work will control for and describe the effects of these potentially confounding factors as the zebrafish model is further developed. A further limitation of this study is that the NanoLuc substrates were screened at a single concentration based on previous literature [233], and their affinities for the studied transporters are not yet known. The use of a single concentration for all substrates permitted identification of relatively brighter substrates and was adequate to detect differences with and without inhibitor for at least one transporter. Future work may aim to better understand the affinities of these substrates towards drug efflux transporters to better understand the mechanisms of BBB disrupting technologies and therapeutics in more complex models.

5.6 Conclusions

Zebrafish offer a unique model to study transporter activity at the BBB. The major challenge in studying BBB integrity is the complexity of the system. Beyond the specialized endothelial cells of the BBB, the NVU provides a supportive role that has yet to be fully recapitulated *in vitro*. Exciting work is being done to advance *in vitro* models through approaches such as biofabrication [252]. Animal models, which more fully describe the BBB and NVU, typically rely on fluorescently-tagged model

molecules to report vessel permeabilization, which often can only be evaluated after euthanasia and tissue processing, requiring time-intensive techniques and sophisticated microscopy and analysis [85]. Mouse models with bioluminescent readouts of ABC transporter activity at the BBB are feasible and do not require euthanasia [227], but still present throughput challenges. In contrast, juvenile zebrafish (up to ~7 dpf) can be handled on the benchtop and assayed in 96-well plates, providing a readily accessible quantitative tool to measure BBB permeability. This model would provide a quantitative measure of BBB permeability, as opposed to more traditional qualitative observations of fluorescently tagged molecules. Towards this goal, our lab has recently characterized zebrafish Abcg2a and Abcb4 transporters as functional homologs of human ABCG2 and ABCB1 and both are expressed at the BBB [95]. Having now established the zebrafish ABC transporter status of NanoLuc substrates, we are developing a transgenic zebrafish model that relies on NanoLuc luciferase luminescence to study the functions of these ABC transporters in determining BBB permeability. Overall, this demonstrates the feasibility of using NanoLuc substrates as a tool to probe the role of ABC transporters in BBB integrity in zebrafish. In addition, it should be noted that knowing whether various NanoLuc substrates are transported by the major multidrug transporters ABCB1 and ABCG2 will facilitate interpretation of results obtained using these new NanoLuc substrates in a variety of cell-based and whole animal assays.

Chapter 6: Conclusions and Future Work

6.1 Thesis Summary

This thesis builds upon Dr. Collin Inglut's discovery that VP can form a nanosuspension in solution when added to water under controlled conditions. He demonstrated that NanoVP was taken up by GBM to a greater extent than liposomal VP, enabling it to serve as a better photosensitizer formulation. He also found that NanoVP-PDT conferred a slight survival benefit over liposomal VP in a flank model of GBM, and indicated that NanoVP-mediated photodynamic priming (PDP) could permeabilize the BBB in rats to a greater extent than 5-ALA.

From this starting point, this thesis aimed to better characterize NanoVP to prepare NanoVP for investigation in larger animals and eventually in the clinic, which is the goal that unites the work in this thesis.

In Chapter 2, the first hurdle was to increase the concentration of NanoVP. Upon investigating two methods to methods to increase concentration, by increasing the concentration of VP in organic solvent and increasing the amount of organic solvent added to water, I observed a change in diameter. From here, I explored additional parameters to understand how the diameter of the nanoaggregate could be modified. This is the most extensive exploration of nanoaggregate modulation at this time, likely because most nanoaggregates or nanocrystals are used commercially, and their characterization may not be published. From here, I sought to evaluate both the long-term stability of NanoVP, the stability of the formulation in various solutions that can

be delivered intravenously, and an automated system to increase the output of NanoVP. The nanoaggregate is stable for well over a year at temperatures above freezing and can be dialyzed into several infusible liquids. The pump system was as good as two well-trained experimenters at making NanoVP. In all, this portion of the thesis provides a strong background for the preparation of NanoVP with several different properties.

In Chapter 3, I addressed the recurring question of how the nanoaggregate behaved in the blood. I first evaluated pharmacokinetics and biodistribution, finding that it behaved similarly to Visudyne. The behavior of the nanoparticles within the blood was also of interest. I had trouble using DLS or fluorescent lifetime imaging microscopy to evaluate particle size upon interaction with serum molecules as the particles were either too small or produced too much background fluorescence. Based on results that showed that NanoVP unquenched when mixed with fetal bovine serum, I tried imaging it *via* TEM after mixing with human serum, which provided evidence that NanoVP dissociated in serum in a concentration-dependent manner. This provided some evidence that NanoVP may become bioavailable by redistributing to biomolecules in the blood. Recent studies indicate that VP in Visudyne redistributes to biomolecules quickly after the introduction into the blood support this. Finally, I sought to understand the bioavailability of NanoVP in the brain. Even though this drug is in clinical trials for the management of GBM, there is scant evidence supporting its ability to get to the brain. My results indicated that NanoVP may enter the brain where the BBB is permeabilized by a tumor, but likely does not accumulate to a significant degree when the BBB is intact.

In Chapter 4, after understanding the biodistribution of NanoVP, I worked to understand its efficacy in orthotopic GBM using a PDX. First, I evaluated uptake and cell killing of NanoVP, free VP, liposomal VP, VP-TBST, and 5-ALA in *ex vivo* GBM39, finding that NanoVP uptake was comparable to free VP in GBM39 cells, and NanoVP killing was comparable to free VP killing after light irradiation. To understand how to treat this tumor *in vivo*, I performed a 3+3 style dose-escalation study to identify tolerable PDT doses using NanoVP. The main adverse event observed was edema, which, when fatal, typically led to animal death in the first 12 hours post-treatment. After identifying a tolerable dose with NanoVP, I performed a survival study. The data indicated the NanoVP-PDT outperformed all other photosensitizer formulations, with significant improvement in survival against untreated mice and mice treated with liposomal VP-PDT. VP is in clinical trials for light-independent applications of the drug. I evaluated cytotoxicity, gap closure, and clonogenicity of GBM cells treated with NanoVP in a light-independent manner, and found that it decreased viability, gap closure rate, and clonogenicity. The values I found to be efficacious were far above those reported in the literature, potentially because many in the literature use YAP-dependent cell lines and primary cells. The next logical step was to combine NanoVP-PDT with light-independent VP. While there was some slight decrease in clonogenic capacity after combination treatment, there was no improvement in cell killing as measured by cell viability assay.

In Chapter 5, in order to extend our understanding of VP's ability to permeabilize the BBB, I contributed to the development of a zebrafish model of the BBB. The model relies on NanoLuciferase expressed behind the BBB, and agents that

disrupt the BBB will permit a detectable bioluminescent signal. Some NanoLuciferase substrates are transported by ABC transporters; as such, the goal of this portion of the project was to identify which NanoLuciferase substrates in a panel of 16 were also transported by the zebrafish and human ABC transporters expressed at the BBB. This permitted the identification of several compounds which could serve as tools to probe specific transporters at the BBB.

6.2 Specific Discoveries

6.2.1 Modulation of NanoVP Parameters

NanoVP's initial formulation had a diameter of around 100 nm and a concentration of <140 μM. Through this work, I developed techniques to tune the diameter between 50 nm and 200 nm and increased the concentration up to 800 μM.

6.2.2 Biodistribution and Pharmacokinetics of NanoVP

The behavior of NanoVP in the blood was unknown. Through TEM, I found that NanoVP dissociates in the blood by decreasing its diameter. Additionally, the ability of VP to enter the brain was not known. I demonstrated that NanoVP is minimally able to cross an intact BBB, and that it may cross a corrupted BBB, but to a low degree. Finally, the bioavailability of NanoVP after oral administration was not known. For patients who may receive high doses of NanoVP for light-independent management of GBM, oral administration is likely preferable to intravenous administration, which is the current clinical standard.

6.2.3 Efficacy of NanoVP-Photodynamic Therapy on Orthotopic Glioblastoma

Intracranial PDT with VP was performed in one dose-finding clinical trial in 2005 (NCT00002647), although its efficacy and safety were not reported. Beyond this, PDT with VP in GBM has not been performed. In this work, I performed a dose-escalation study to find a safe light dose for treatment of orthotopic GBM and demonstrated that the treatment is well-tolerated in mice and provides a survival benefit. I also benchmarked NanoVP-PDT against liposomal VP-PDT, which it outperformed, and 5-ALA, against which it did not show a significant survival difference. In addition to this, I demonstrated that 635 nm light for the activation of PpIX can generate heat, raising a potential concern for ongoing clinical trials using 5-ALA for PDT in GBM.

I also demonstrated that NanoVP may be suitable for the management of GBM as chemotherapy. This provides a new delivery method to explore the light-independent use of VP in GBM and other cancers.

6.2.4 Supporting a Zebrafish Model of the Blood-Brain Barrier

I screened the brightness of several coelenterazine and furimazine analogs, providing an updated reference in the literature. I also identified which of the analogs are transported by human ABCB1 and ABCG2, and their zebrafish multidrug transporter homologs Abcb4 and Abcg2a, providing a reference for future exploration of ABC transporter disruption at the BBB. This also supports homology in the function of the respective human and zebrafish transporters.

6.3 Contributions to the Field

6.3.1 Scientific Contributions

This thesis expands the field of PDT in GBM, as well as of light-independent applications of GBM, in the following ways:

- It expands achievable formulation parameters for a nanosuspension of VP (**Chapter 2**)
- It identifies clinically applicable infusible solutions that NanoVP is stable in, as and identifies a potential pH dependence for stability (**Chapter 2**)
- It identifies appropriate storage conditions for NanoVP as well as tests prolonged stability (**Chapter 2**)
- It develops a technique to make NanoVP in an automated fashion (**Chapter 2**)
- It develops a liquid chromatography-tandem mass spectroscopy technique for the quantification of VP in tissues (**Chapter 3**)
- It quantifies pharmacokinetic and biodistributive properties of NanoVP (**Chapter 3**)
- It demonstrates a mechanism for the dissociation of VP in the blood (**Chapter 3**)
- It demonstrates oral bioavailability of NanoVP (**Chapter 3**)
- It quantifies VP's limited ability to penetrate the BBB (**Chapter 3**)

- It demonstrates the feasibility and efficacy of NanoVP-PDT in orthotopic GBM, and provides evidence that the efficacy may be due to debulking of the tumor (**Chapter 4**)
- It develops a novel monodisperse formulation of VP, TBST-VP (**Chapter 4**)
- It demonstrates improved efficacy over PDT with 5-ALA-induced PpIX in orthotopic GBM, and identifies a possible safety risk in heat generation for 5-ALA-induced PpIX excited with 635 nm light (**Chapter 4**)
- It demonstrates comparable light-independent cytotoxicity of NanoVP and a Visudyne-like formulation of VP, and the potential of NanoVP to reduce gap closure and inhibit clonogenicity in GBM cells (**Chapter 4**)
- It identifies that the dose of VP that is cytotoxic for PDT is not efficacious for light-independent applications of VP (**Chapter 4**)
- It demonstrates limited combinatorial effects of PDT and light-independent applications of VP in cell culture (**Chapter 4**)
- It summarizes the brightness of a panel of 16 NanoLuciferase substrates, and identifies which are transported at ABC transporters relevant to the BBB in humans and zebrafish (**Chapter 5**)

6.3.2 Published Manuscripts

# indicates equal contributions

- **Quinlan JA** #, Inglut CT #, Srivastava P, Rahman I, Stabile J, Gaitan B, Arnau Del Valle C, Baumiller K, Gaur A, Chiou W-A, Karim B, Connolly N, Robey

RW, Woodworth GF, Gottesman MM, Huang HC. Carrier-Free, Amorphous Verteporfin Nanodrug for Enhanced Photodynamic Cancer Therapy and Brain Drug Delivery. *Adv Sci (Weinh)*. 2024;11(17):e2302872. doi:10.1002/advs.202302872

- Yang J #, Ma CH #, **Quinlan JA**, McNaughton K, Lee T, Shin P, Hauser T, Kaluzienski ML, Vig S, Quang TT, Starost MF, Huang HC, Mueller JL. Light-activatable minimally invasive ethyl cellulose ethanol ablation: biodistribution and potential applications. *Bioengineering & Translational Medicine* 2024; e10696. doi.org/10.1002/btm2.10696

- **Quinlan JA**, Baumiller K, Gaur A, Chiow W-A, Robey RW, Gottesman MM, and Huang H-C, "Self-Assembled Verteporfin Nanoparticles for Photodynamic and Light-Independent Therapy in Glioblastoma." *Adv NanoBiomed Res.* 2024;2400098. doi: 10.1002/anbr.202400098.

- **Quinlan JA,** Sabbeneni S, Robey RW, Lipsey CC, Inglut CT, Thomas JR, Walker JR, Zhou W, Huang HC, Gottesman MM. Identification of NanoLuciferase substrates transported by human ABCB1 and ABCG2 and their zebrafish homologs at the blood-brain barrier. *Molecular Pharmacology.* 2024. doi: 10.1124/molpharm.123.000811.

6.3.3 Manuscripts in Preparation

# indicates equal contributions

- Ma CH #, Yang J #, **Quinlan JA**, McNaughton K, Hauser T, Starost M, Mueller JL, Huang HC. Efficacy of light-activatable ethanol injection for the treatment of early-stage unresectable hepatocellular carcinoma. *In preparation.*
- Ma CH, **Quinlan JA**, Huang HC. NanoVP Photobleaching in Swine Peritoneal Organs. *In preparation.*

6.3.4 Oral Presentations

Underline denotes presenter.

- **J. Quinlan**, P. Srivastava, K. Baumiller, C. Arnau del Valle, A. Gaur, R.W. Robey, M. Gottesman, H.C. Huang. Self-assembled verteporfin nanoaggregates for photodynamic therapy in glioblastoma multiforme. July 2024. American Society for Biomaterials. Chicago, IL.
- **J. Quinlan**, K. Baumiller, R. Robey, M. Gottesman, H.C. Huang. Optimization and evaluation of nanoparticle verteporfin formulations. July 2023. World Congress of the International Photodynamic Association. Tampere, Finland.
- **J. Quinlan**, C. Inglut, P. Srivastava, I. Rahman, J. Stabile, B. Gaitan, C. Arnau del Valle, K. Baumiller, A. Gaur, W.-A. Chiou, B. Karim, N. Connolly, R. W. Robey, G. F. Woodworth, M. M. Gottesman, H.-C. Huang. "A nanosuspension of verteporfin improves photodynamic therapy management of glioblastoma." April 2024. NCI-UMD Seminar. College Park, MD.
- C.H. Ma, J. Yang, **J. Quinlan**, K. McNaughton, T. Hauser, J. L. Mueller, H.C. Huang. Photodynamic Therapy for Locally Advanced Unresectable Tumors

with Light-Activatable Ethanol Injection. July 2023. World Congress of the International Photodynamic Association. Tampere, Finland.

- **J. Quinlan**, C. Inglut, K. Baumiller, I. Rahman, H.C. Huang. Excipient-free pure drug photosensitizer nanoparticles for PDT, imaging, and chemotherapy of cancer. January 2023. SPIE Photonics West. San Francisco, CA.

- C.T. Inglut, **J. Quinlan,** I. Rahman, J. Stabile, B. Gaitan, P. Srivastava, W.A. Choiu, B. Karim, N. Connolly, R.W. Robey, G. Woodworth, M.M. Gottesman, H.C. Huang. Clinically relevant pure porphyrin nanoparticles for photodynamic therapy and priming applications. April 2022. SPIE Photonics Europe. Strasbourg. France.

6.3.5 Poster Presentations

Underline denotes presenter

- **J. Quinlan**, P. Srivastava, K. Baumiller, C. Arnau del Valle, A. Gaur, R.W. Robey, M. Gottesman, H.C. Huang. Photodynamic therapy in glioblastoma multiforme using self-assembled verteporfin nanoparticles. July 2024. 39th Annual MD/PhD Student Conference. Breckenridge, CO.

- **J. Quinlan,** W.A. Chiou, R.W. Robey, M.M. Gottesman, H.C. Huang. Transmission electron microscopy study of a nanosuspension of verteporfin and evaluation of stability in human serum. July 2024. Microscopy and Microanalysis. Columbus, OH.

- **J. Quinlan**, A. Gaur, P. Srivastava, C. Arnau del Valle, K. Baumiller, R. Robey, M. M. Gottesman, H.-C. Huang. Comparison of 5-aminolevulinic acid and

verteporfin for photodynamic therapy and YAP-TEAD inhibition in glioblastoma multiforme. February 2024. NIH Graduate Student Symposium. Bethesda, MD.

- **J. Quinlan**, A. Guar, K. Baumiller, R.W. Robey, M.M. Gottesman, H.C. Huang. Verteporfin photodynamic therapy for the treatment of glioblastoma in patient-derived xenograft mouse models. July 2023. World Congress of the International Photodynamic Association. Tampere, Finland.

- **J. Quinlan**, C. T. Inglut, R. W. Robey, J. R. Thomas, H.-C. Huang, M. M. Gottesman. Probing ATP-binding cassette transporter inhibitors *via* a high-throughput bioluminescent assay. May 2023. NIH Center for Cancer Research Young Investigators Symposium. Shady Grove, MD.

- **J. Quinlan**, C. T. Inglut, R. W. Robey, J. R. Thomas, H.-C. Huang, M. M. Gottesman. A cell-based bioluminescent assay for the characterization of ATP binding cassette transporter substrates. February 2023. NIH Graduate Student Symposium. Bethesda, MD.

- D. Muthusamy, S. Vellala, **J. Quinlan**, M. A. Rudek, C. I. Civin, and T. Lowe. "Slow Release of An Antileukemic Artemisinin Analog from An Injectable, Biodegradable In Situ Gelling System." April 2022. Society for Biomaterials. Baltimore, MD.

6. 4 Future Studies

6.4.1 Evaluation of Bioburden in NanoVP

Attempts to produce NanoVP in a sterile manner (sterile DMSO, autoclaved equipment, sterile water, production in biosafety cabinet) were successful. Additionally, NanoVP was able to pass through a 0.22 μm filter. While no NanoVP samples prepared in this study, which were prepared in a nonsterile environment on the benchtop, resulted in contamination in cell culture or in illness or reaction in mice, the bioburden of NanoVP remains to be understood. Attempts to quantify bioburden *via* gelation failed due to the lack of appropriate equipment, and attempts to use colorimetric assays to quantify bioburden failed due to overlapping signal from NanoVP. Additionally, NanoVP was found to be unstable in solutions from prepared IV bags but was stable in house-made solutions of the same materials, indicating presence of an additive that impacts stability. Next steps in the translation of NanoVP will require standard measurements of endotoxin bioburden.

6.4.2 Tangential Flow Filtration to increase NanoVP's Concentration

In this thesis, the concentration was increased *via* modulation of steps in the synthesis method, but limits on stability of nanoparticles were observed. Tangential flow filtration is a widely used technique to concentrate nanoparticles and other nanosuspension. This may be a promising technique to further increase the concentration of NanoVP.

6.4.3 Evaluation of NanoVP Performance in the Blood

Historic literature on Visudyne indicated that VP delivered in organic solvent distributed through the blood and ultimately the body in different manners [170, 171, 184-186, 197]. A next logical step for NanoVP is to mix NanoVP with whole human blood, separate it *via* gradient centrifugation, then analyze which compartments of the blood VP ends up in. Premixing VP with these individual components may also provide a new, organically targeted formulation of the drug.

6.4.4 Evaluation of NanoVP-PDT in Resected Glioblastoma

Our collaborators have made efforts to resect GBM in rodent models [253]. The model tested in this thesis is closer to stereotactic PDT in an unresectable tumor. Testing efficacy in a resection context may permit evaluation of the potential to treat primary tumors post-resection. While not a trivial pursuit, the addition of this technique to the mouse model described here is feasible.

It is also notable that GBM39 cells expressing luciferase can permit 3D rendering of estimated tumor volume (**Figure 6-1**). This may be a useful and unique approach to tracking invasion and viable tumor volume over time post-PDT *in vivo.*

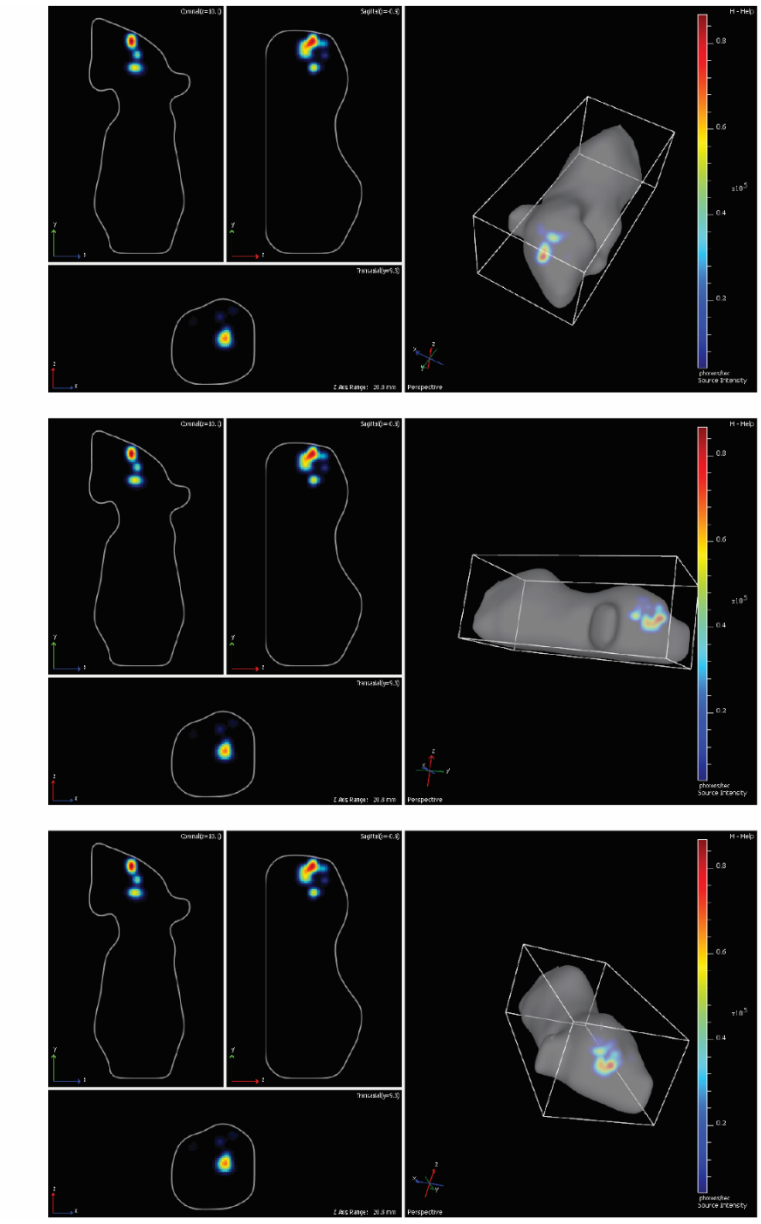

Figure 6-1. Sample 3D renderings of *in vivo* GBM39 tumors. At two weeks post-implantation, IVIS imaging can be used to render approximate volumetric renderings of orthotopic GBM tumors based on bioluminescence after luciferin injection. Outlines in the left panes indicate coronal, sagittal, and transaxial plains. A 3D reconstruction, with the mouse shown in grey and axis orientations in the lower left corner, is shown in the right panels. In all images, color indicates detected bioluminescent light, with red being the most intense light. A main tumor mass with some potential invasion is appreciable.

6.4.5 Evaluation of NanoVP-PDT to Enhance NanoVP Levels in the Brain

We have shown that NanoVP-PDT can inhibit ABC transporters [112, 113, 214] and permeabilize the BBB [109, 110]. As the work here indicates that VP can penetrate an intact BBB to a minimal degree, and that the anticancer combinatorial effect of NanoVP-PDT and light-independent NanoVP is minimal, a logical next step is to use NanoVP-PDP to permeabilize the BBB, then deliver NanoVP at higher doses for application as chemotherapy. Given the apparent bioavailability of orally delivered NanoVP, it may be best to attempt this *via* oral gavage in mice. One can imagine a clinical workflow in which a patient receives either resection with PDT or stereotactic PDT, then orally ingests NanoVP for its application as chemotherapy.

6.4.6 Zebrafish to Evaluate Mechanisms of Photodynamic Therapy-Mediated Blood-Brain Barrier Permeabilization

The utility of VP-PDP to permeabilize the BBB has been established, but the specific mechanisms have not been identified. It appears that both junctional complexes and ABC transporters are impacted by PDP; however, we have yet to demonstrate this dual effect *in vivo*. The zebrafish, as a much higher-throughput model than mice, may be ideal to do this. As we have identified substrates of zebrafish ABC transporters at the BBB, and considering homologies in junctional proteins at the zebrafish BBB [94-96], attempts to histologically verify disruption of junctional proteins and transporters at the BBB may be warranted. Preliminary work in this thesis identified tolerable doses of NanoVP for incubation, and designed a potential holding system to position anesthetized zebrafish during irradiation (**Figure 6-2**).

Figure 6-2. 3D-printed agarose mold to hold embryonic zebrafish during light irradiation. The 3D printed mold is designed to fit within an ibidi chamber slide and to leave indentations in agarose to permit positioning of zebrafish for imaging and light irradiation. The reliefs are the approximate size of 7 dpf embryonic zebrafish, permitting some flexibility in timing of irradiation. Scale bar is 5 mm. Designed and printed by Taya Lee.

6.5 Outlook

This thesis aims to support the clinical translation of NanoVP. I posit that the greatest challenge to NanoVP will be its inability to cross the BBB. While vascular shutdown may result in greater outcomes than in 5-ALA-induced PpIX PDT, one can imagine that this will also be its greatest weakness. The average intercapillary distance in the brain is thought to be ~40 μm [254], indicating the need for nutrient and oxygen transport in the brain. Tissues next to the tumor containing disperse tumor cells that cause recurrence are not resected during surgery out of concern for damage to eloquent tissue. In a similar manner, activation of VP in these vessels causing shutdown of vasculature and subsequent oxygen starvation of juxtatumoral tissue is undesirable. The challenge here will be delivering light at a low enough dose to ensure blood vessel viability but at a high enough dose to ablate tumor cells, if ablation is the therapeutic goal. Without careful dosimetry and carefully delivered light that reflects the geometry of patient tumors, safe and effective PDT in the brain will be challenging. Work preceding this thesis evaluates the impact of NanoVP-PDP on the neuropil, but more extensive evaluation of safety may be required before there is confidence in moving this treatment methodology forward. Additionally, it should be noted that sham surgery resulted in an improvement in survival between untreated mice and NanoVP-PDT treated mice in the PDT survival study. As such, there may be a significant immune-based response that should be evaluated in immunocompetent mice. Finally, NanoVP's use in a light-independent manner is fascinating, but a deeper understanding of its efficacy for single cells behind an intact BBB is needed.

This thesis shows the utility for NanoVP-PDT and potentially the utility for light-independent NanoVP. As discussed earlier, YAP-mediated signaling seems to be potentially effective in several cancer types. It is worth considering that there may be utility for these therapeutic modalities outside of GBM. Tumors that do not present such a challenge to the delivery of the molecule to tumor cells may respond better to this treatment scheme. PDT has shown promise in pancreatic cancer, and colorectal cancer patients are often younger and dealing with more extensive cancer in a region to which light delivery is generally easier. As such, the results presented here should be considered in other types of cancer considering the potential adverse impacts of PDT.

In all, this thesis further prepares NanoVP for NanoVP-PDT, NanoVP-PDP, and NanoVP-mediated YAP/TAZ disruption, regardless of the ultimate tumor type in which it is most effective. Cancer presents an ongoing challenge for the medical community despite remarkable advancements and progress over the past few decades. With the goal of improving the patient's quality of life in mind, any safe progress towards improved treatment outcomes, no matter how incremental, is valuable.

Bibliography

1. Ostrom, Q.T., et al., *CBTRUS Statistical Report: Primary Brain and Other Central Nervous System Tumors Diagnosed in the United States in 2015-2019.* Neuro Oncol, 2022. **24**(Suppl 5): p. v1-v95.
2. Schaff, L.R. and I.K. Mellinghoff, *Glioblastoma and Other Primary Brain Malignancies in Adults: A Review.* JAMA, 2023. **329**(7): p. 574-587.
3. Louis, D.N., et al., *The 2021 WHO Classification of Tumors of the Central Nervous System: a summary.* Neuro Oncol, 2021. **23**(8): p. 1231-1251.
4. Tan, A.C., et al., *Management of glioblastoma: State of the art and future directions.* CA Cancer J Clin, 2020. **70**(4): p. 299-312.
5. Cuddapah, V.A., et al., *A neurocentric perspective on glioma invasion.* Nat Rev Neurosci, 2014. **15**(7): p. 455-65.
6. Campos, B., et al., *A comprehensive profile of recurrent glioblastoma.* Oncogene, 2016. **35**(45): p. 5819-5825.
7. Ron, E., et al., *Tumors of the brain and nervous system after radiotherapy in childhood.* N Engl J Med, 1988. **319**(16): p. 1033-9.
8. Ostrom, Q.T., et al., *Risk factors for childhood and adult primary brain tumors.* Neuro Oncol, 2019. **21**(11): p. 1357-1375.
9. Inskip, P.D., M.S. Linet, and E.F. Heineman, *Etiology of brain tumors in adults.* Epidemiol Rev, 1995. **17**(2): p. 382-414.
10. Wrensch, M., et al., *Epidemiology of primary brain tumors: current concepts and review of the literature.* Neuro Oncol, 2002. **4**(4): p. 278-99.
11. Amirian, E.S., et al., *Approaching a Scientific Consensus on the Association between Allergies and Glioma Risk: A Report from the Glioma International Case-Control Study.* Cancer Epidemiol Biomarkers Prev, 2016. **25**(2): p. 282-90.
12. Yoshikawa, M.H., et al., *Modifiable risk factors for glioblastoma: a systematic review and meta-analysis.* Neurosurg Rev, 2023. **46**(1): p. 143.
13. Brown, T.J., et al., *Association of the Extent of Resection With Survival in Glioblastoma: A Systematic Review and Meta-analysis.* JAMA Oncol, 2016. **2**(11): p. 1460-1469.
14. Karschnia, P., et al., *Evidence-based recommendations on categories for extent of resection in diffuse glioma.* Eur J Cancer, 2021. **149**: p. 23-33.
15. Molinaro, A.M., et al., *Association of Maximal Extent of Resection of Contrast-Enhanced and Non-Contrast-Enhanced Tumor With Survival Within Molecular Subgroups of Patients With Newly Diagnosed Glioblastoma.* JAMA Oncol, 2020. **6**(4): p. 495-503.
16. Hadjipanayis, C.G., G. Widhalm, and W. Stummer, *What is the Surgical Benefit of Utilizing 5-Aminolevulinic Acid for Fluorescence-Guided Surgery of Malignant Gliomas?* Neurosurgery, 2015. **77**(5): p. 663-73.
17. Diez Valle, R., C.G. Hadjipanayis, and W. Stummer, *Established and emerging uses of 5-ALA in the brain: an overview.* J Neurooncol, 2019. **141**(3): p. 487-494.
18. Stupp, R., et al., *Effects of radiotherapy with concomitant and adjuvant temozolomide versus radiotherapy alone on survival in glioblastoma in a*

randomised phase III study: 5-year analysis of the EORTC-NCIC trial. Lancet Oncol, 2009. **10**(5): p. 459-66.
19. Stupp, R., et al., *Radiotherapy plus concomitant and adjuvant temozolomide for glioblastoma.* N Engl J Med, 2005. **352**(10): p. 987-96.
20. Wesolowski, J.R., P. Rajdev, and S.K. Mukherji, *Temozolomide (Temodar).* AJNR Am J Neuroradiol, 2010. **31**(8): p. 1383-4.
21. Hegi, M.E., et al., *MGMT gene silencing and benefit from temozolomide in glioblastoma.* N Engl J Med, 2005. **352**(10): p. 997-1003.
22. Pegg, A.E., *Repair of O(6)-alkylguanine by alkyltransferases.* Mutat Res, 2000. **462**(2-3): p. 83-100.
23. McKinnon, C., et al., *Glioblastoma: clinical presentation, diagnosis, and management.* BMJ, 2021. **374**: p. n1560.
24. McBain, C., et al., *Treatment options for progression or recurrence of glioblastoma: a network meta-analysis.* Cochrane Database Syst Rev, 2021. **5**(1): p. CD013579.
25. Westphal, M., et al., *A phase 3 trial of local chemotherapy with biodegradable carmustine (BCNU) wafers (Gliadel wafers) in patients with primary malignant glioma.* Neuro Oncol, 2003. **5**(2): p. 79-88.
26. Ashby, L.S., K.A. Smith, and B. Stea, *Gliadel wafer implantation combined with standard radiotherapy and concurrent followed by adjuvant temozolomide for treatment of newly diagnosed high-grade glioma: a systematic literature review.* World J Surg Oncol, 2016. **14**(1): p. 225.
27. Attenello, F.J., et al., *Use of Gliadel (BCNU) wafer in the surgical treatment of malignant glioma: a 10-year institutional experience.* Ann Surg Oncol, 2008. **15**(10): p. 2887-93.
28. Champeaux, C. and J. Weller, *Implantation of carmustine wafers (Gliadel((R))) for high-grade glioma treatment. A 9-year nationwide retrospective study.* J Neurooncol, 2020. **147**(1): p. 159-169.
29. Westphal, M., et al., *Gliadel wafer in initial surgery for malignant glioma: long-term follow-up of a multicenter controlled trial.* Acta Neurochir (Wien), 2006. **148**(3): p. 269-75; discussion 275.
30. Pitter, K.L., et al., *Corticosteroids compromise survival in glioblastoma.* Brain, 2016. **139**(Pt 5): p. 1458-71.
31. Alkhalili, K., G. Zenonos, and J.C. Fernandez-Miranda, *Do Corticosteroids Compromise Survival in Glioblastoma?* Neurosurgery, 2016. **79**(4): p. N15-6.
32. Lote, K., et al., *Prevalence and prognostic significance of epilepsy in patients with gliomas.* Eur J Cancer, 1998. **34**(1): p. 98-102.
33. Walbert, T., et al., *SNO and EANO practice guideline update: Anticonvulsant prophylaxis in patients with newly diagnosed brain tumors.* Neuro Oncol, 2021. **23**(11): p. 1835-1844.
34. Saito, M., N.A. Wages, and D. Schiff, *Incidence, risk factors and management of venous thromboembolism in patients with primary CNS lymphoma.* J Neurooncol, 2021. **154**(1): p. 41-47.
35. Salvalaggio, A., et al., *Glioblastoma and brain connectivity: the need for a paradigm shift.* Lancet Neurol, 2024. **23**(7): p. 740-748.

36. De Bonis, P., et al., *The influence of surgery on recurrence pattern of glioblastoma.* Clin Neurol Neurosurg, 2013. **115**(1): p. 37-43.
37. Keime-Guibert, F., et al., *Radiotherapy for glioblastoma in the elderly.* N Engl J Med, 2007. **356**(15): p. 1527-35.
38. Aiyappa-Maudsley, R., A.J. Chalmers, and J.L. Parsons, *Factors affecting the radiation response in glioblastoma.* Neurooncol Adv, 2022. **4**(1): p. vdac156.
39. Stupp, R., et al., *High-grade glioma: ESMO Clinical Practice Guidelines for diagnosis, treatment and follow-up.* Ann Oncol, 2014. **25 Suppl 3**: p. iii93-101.
40. de Goojier, M., et al., *Improved Brain Penetration and Antitumor Efficacy of Temozolomide by Inhibition of ABCB1 and ABCG2.* Neoplasia, 2018. **20**(7): p. 710-720.
41. Portnow, J., et al., *The neuropharmacokinetics of temozolomide in patients with resectable brain tumors: potential implications for the current approach to chemoradiation.* Clin Cancer Res, 2009. **15**(22): p. 7092-8.
42. Kamson, D.O. and S.A. Grossman, *The Role of Temozolomide in Patients With Newly Diagnosed Wild-Type IDH, Unmethylated MGMTp Glioblastoma During the COVID-19 Pandemic.* JAMA Oncol, 2021. **7**(5): p. 675-676.
43. Blumenthal, D.T., et al., *Is more better? The impact of extended adjuvant temozolomide in newly diagnosed glioblastoma: a secondary analysis of EORTC and NRG Oncology/RTOG.* Neuro Oncol, 2017. **19**(8): p. 1119-1126.
44. Mrugala, M.M., *Advances and challenges in the treatment of glioblastoma: a clinician's perspective.* Discov Med, 2013. **15**(83): p. 221-30.
45. Rapp, M., et al., *Recurrence Pattern Analysis of Primary Glioblastoma.* World Neurosurg, 2017. **103**: p. 733-740.
46. van Solinge, T.S., et al., *Advances in local therapy for glioblastoma - taking the fight to the tumour.* Nat Rev Neurol, 2022. **18**(4): p. 221-236.
47. Kalamida, D., et al., *Fever-range hyperthermia vs. hypothermia effect on cancer cell viability, proliferation and HSP90 expression.* PLoS One, 2015. **10**(1): p. e0116021.
48. van der Zee, J., *Heating the patient: a promising approach?* Ann Oncol, 2002. **13**(8): p. 1173-84.
49. Holste, K.G. and D.A. Orringer, *Laser interstitial thermal therapy.* Neurooncol Adv, 2020. **2**(1): p. vdz035.
50. Menovsky, T., et al., *Interstitial laser thermotherapy in neurosurgery: a review.* Acta Neurochir (Wien), 1996. **138**(9): p. 1019-26.
51. Fadel, H.A., et al., *Laser Interstitial Thermal Therapy for First-Line Treatment of Surgically Accessible Recurrent Glioblastoma: Outcomes Compared With a Surgical Cohort.* Neurosurgery, 2022. **91**(5): p. 701-709.
52. Pang, S., et al., *Nanoparticle-assisted, image-guided laser interstitial thermal therapy for cancer treatment.* Wiley Interdiscip Rev Nanomed Nanobiotechnol, 2022. **14**(5): p. e1826.
53. Kim, Y.S., et al., *High-intensity focused ultrasound therapy: an overview for radiologists.* Korean J Radiol, 2008. **9**(4): p. 291-302.

54. Meng, Y., K. Hynynen, and N. Lipsman, *Applications of focused ultrasound in the brain: from thermoablation to drug delivery.* Nat Rev Neurol, 2021. **17**(1): p. 7-22.
55. Mahmoudi, K., et al., *Magnetic hyperthermia therapy for the treatment of glioblastoma: a review of the therapy's history, efficacy and application in humans.* Int J Hyperthermia, 2018. **34**(8): p. 1316-1328.
56. Schwartz, C., et al., *Outcome and toxicity profile of salvage low-dose-rate iodine-125 stereotactic brachytherapy in recurrent high-grade gliomas.* Acta Neurochir (Wien), 2015. **157**(10): p. 1757-64; discussion 1764.
57. Kickingereder, P., et al., *Low-dose rate stereotactic iodine-125 brachytherapy for the treatment of inoperable primary and recurrent glioblastoma: single-center experience with 201 cases.* J Neurooncol, 2014. **120**(3): p. 615-23.
58. Sarria, G.R., et al., *Intraoperative radiotherapy for glioblastoma: an international pooled analysis.* Radiother Oncol, 2020. **142**: p. 162-167.
59. Giordano, F.A., et al., *Intraoperative Radiotherapy in Newly Diagnosed Glioblastoma (INTRAGO): An Open-Label, Dose-Escalation Phase I/II Trial.* Neurosurgery, 2019. **84**(1): p. 41-49.
60. Palavani, L.B., et al., *Efficacy and Safety of Intraoperative Radiotherapy for High-Grade Gliomas: A Systematic Review and Meta-Analysis.* Neurosurg Rev, 2024. **47**(1): p. 47.
61. Mahmoudi, K., et al., *5-aminolevulinic acid photodynamic therapy for the treatment of high-grade gliomas.* J Neurooncol, 2019. **141**(3): p. 595-607.
62. Schipmann, S., et al., *Combination of ALA-induced fluorescence-guided resection and intraoperative open photodynamic therapy for recurrent glioblastoma: case series on a promising dual strategy for local tumor control.* J Neurosurg, 2021. **134**(2): p. 426-436.
63. Eljamel, M.S., C. Goodman, and H. Moseley, *ALA and Photofrin fluorescence-guided resection and repetitive PDT in glioblastoma multiforme: a single centre Phase III randomised controlled trial.* Lasers Med Sci, 2008. **23**(4): p. 361-7.
64. da Silva, E.B., Jr., et al., *Association of 5-aminolevulinic acid fluorescence guided resection with photodynamic therapy in recurrent glioblastoma: a matched cohort study.* Acta Neurochir (Wien), 2024. **166**(1): p. 212.
65. Vermandel, M., et al., *Standardized intraoperative 5-ALA photodynamic therapy for newly diagnosed glioblastoma patients: a preliminary analysis of the INDYGO clinical trial.* J Neurooncol, 2021. **152**(3): p. 501-514.
66. Quach, S., et al., *Interstitial photodynamic therapy for newly diagnosed glioblastoma.* J Neurooncol, 2023. **162**(1): p. 217-223.
67. Sarkaria, J.N., et al., *Is the blood-brain barrier really disrupted in all glioblastomas? A critical assessment of existing clinical data.* Neuro Oncol, 2018. **20**(2): p. 184-191.
68. Bobo, R.H., et al., *Convection-enhanced delivery of macromolecules in the brain.* Proc Natl Acad Sci U S A, 1994. **91**(6): p. 2076-80.
69. Bruce, J.N., et al., *Regression of recurrent malignant gliomas with convection-enhanced delivery of topotecan.* Neurosurgery, 2011. **69**(6): p. 1272-9; discussion 1279-80.

70. Surapaneni, K., et al., *Early Cerebral Blood Volume Changes Predict Progression After Convection-Enhanced Delivery of Topotecan for Recurrent Malignant Glioma.* World Neurosurg, 2015. **84**(1): p. 163-72.
71. Jahangiri, A., et al., *Convection-enhanced delivery in glioblastoma: a review of preclinical and clinical studies.* J Neurosurg, 2017. **126**(1): p. 191-200.
72. Bregy, A., et al., *The role of Gliadel wafers in the treatment of high-grade gliomas.* Expert Rev Anticancer Ther, 2013. **13**(12): p. 1453-61.
73. De Bonis, P., et al., *Safety and efficacy of Gliadel wafers for newly diagnosed and recurrent glioblastoma.* Acta Neurochir (Wien), 2012. **154**(8): p. 1371-8.
74. D'Amico, R.S., et al., *Correction to: Super selective intra-arterial cerebral infusion of modern chemotherapeutics after blood-brain barrier disruption: where are we now, and where we are going.* J Neurooncol, 2020. **147**(2): p. 279.
75. Ellis, J.A., et al., *Reassessing the Role of Intra-Arterial Drug Delivery for Glioblastoma Multiforme Treatment.* J Drug Deliv, 2015. **2015**: p. 405735.
76. Yang, D.Y., et al., *Enhanced antitumor effects of radiotherapy combined local nimustine delivery rendezvousing with oral temozolomide chemotherapy in glioblastoma patients.* J Cancer Res Ther, 2018. **14**(1): p. 78-83.
77. Vogelbaum, M.A. and M.K. Aghi, *Convection-enhanced delivery for the treatment of glioblastoma.* Neuro Oncol, 2015. **17 Suppl 2**(Suppl 2): p. ii3-ii8.
78. Schaeffer, S. and C. Iadecola, *Revisiting the neurovascular unit.* Nat Neurosci, 2021. **24**(9): p. 1198-1209.
79. Banks, W.A., *From blood-brain barrier to blood-brain interface: new opportunities for CNS drug delivery.* Nat Rev Drug Discov, 2016. **15**(4): p. 275-92.
80. Daneman, R. and A. Prat, *The blood-brain barrier.* Cold Spring Harb Perspect Biol, 2015. **7**(1): p. a020412.
81. Chen, Y. and L. Liu, *Modern methods for delivery of drugs across the blood-brain barrier.* Adv Drug Deliv Rev, 2012. **64**(7): p. 640-65.
82. Pardridge, W.M., *The blood-brain barrier: bottleneck in brain drug development.* NeuroRx, 2005. **2**(1): p. 3-14.
83. Basseville, A., et al., *The ABCG2 Multidrug Transporter*. 2015: Springer Chan.
84. Hawkins, B.T. and T.P. Davis, *The blood-brain barrier/neurovascular unit in health and disease.* Pharmacol Rev, 2005. **57**(2): p. 173-85.
85. Kadry, H., B. Noorani, and L. Cucullo, *A blood-brain barrier overview on structure, function, impairment, and biomarkers of integrity.* Fluids and barriers of the CNS, 2020. **17**(1): p. 69.
86. Durmus, S., J.J. Hendrikx, and A.H. Schinkel, *Apical ABC transporters and cancer chemotherapeutic drug disposition.* Adv Cancer Res, 2015. **125**: p. 1-41.
87. Jackson, S., et al., *Model systems for studying the blood-brain barrier: Applications and challenges.* Biomaterials, 2019. **214**: p. 119217.
88. Sohet, F. and R. Daneman, *Genetic mouse models to study blood-brain barrier development and function.* Fluids Barriers CNS, 2013. **10**(1): p. 3.

89. Kim, S.S., et al., *Zebrafish as a Screening Model for Testing the Permeability of Blood-Brain Barrier to Small Molecules.* Zebrafish, 2017. **14**(4): p. 322-330.
90. Umans, R.A. and M.R. Taylor, *Zebrafish as a model to study drug transporters at the blood-brain barrier.* Clin Pharmacol Ther, 2012. **92**(5): p. 567-70.
91. Jeong, J.Y., et al., *Functional and developmental analysis of the blood-brain barrier in zebrafish.* Brain Res Bull, 2008. **75**(5): p. 619-28.
92. Fischer, S., et al., *Abcb4 acts as multixenobiotic transporter and active barrier against chemical uptake in zebrafish (Danio rerio) embryos.* BMC Biol, 2013. **11**: p. 69.
93. Kobayashi, I., et al., *Characterization and localization of side population (SP) cells in zebrafish kidney hematopoietic tissue.* Blood, 2008. **111**(3): p. 1131-7.
94. Thomas, J.R., et al., *Abcg2a is the functional homolog of human ABCG2 expressed at the zebrafish blood-brain barrier.* Fluids Barriers CNS, 2024. **21**(1): p. 27.
95. Robey, R.W., et al., *Characterization and tissue localization of zebrafish homologs of the human ABCB1 multidrug transporter.* Sci Rep, 2021. **11**(1): p. 24150.
96. Hotz, J.M., et al., *ATP-binding cassette transporters at the zebrafish blood-brain barrier and the potential utility of the zebrafish as an in vivo model.* Cancer Drug Resist, 2021. **4**(3): p. 620-633.
97. Schmidt-Erfurth, U. and T. Hasan, *Mechanisms of action of photodynamic therapy with verteporfin for the treatment of age-related macular degeneration.* Surv Ophthalmol, 2000. **45**(3): p. 195-214.
98. Kessel, D. and N.L. Oleinick, *Cell Death Pathways Associated with Photodynamic Therapy: An Update.* Photochem Photobiol, 2018. **94**(2): p. 213-218.
99. Huggett, M.T., et al., *Phase I/II study of verteporfin photodynamic therapy in locally advanced pancreatic cancer.* Br J Cancer, 2014. **110**(7): p. 1698-704.
100. Hanada, Y., et al., *EUS-guided verteporfin photodynamic therapy for pancreatic cancer.* Gastrointest Endosc, 2021. **94**(1): p. 179-186.
101. Briel-Pump, A., et al., *Accumulation of protoporphyrin IX in medulloblastoma cell lines and sensitivity to subsequent photodynamic treatment.* J Photochem Photobiol B, 2018. **189**: p. 298-305.
102. Yang, X., et al., *Effects of Silencing Heme Biosynthesis Enzymes on 5-Aminolevulinic Acid-mediated Protoporphyrin IX Fluorescence and Photodynamic Therapy.* Photochem Photobiol, 2015. **91**(4): p. 923-30.
103. Valerio, J.E., et al., *5-Aminolevulinic Acid-A Biomarker for Worse Prognosis in IDH-Wildtype II Tumors? Evolution of a Fluorescence-Positive Diffuse Astrocytoma: A Case Report.* J Neurol Surg Rep, 2022. **83**(3): p. e95-e99.
104. Inglut, C.T., et al., *Predictors and Limitations of the Penetration Depth of Photodynamic Effects in the Rodent Brain.* Photochem Photobiol, 2020. **96**(2): p. 301-309.
105. Perria, C., et al., *Fast attempts at the photodynamic treatment of human gliomas.* J Neurosurg Sci, 1980. **24**(3-4): p. 119-29.

106. Cheng, M.K., et al., *Effects of photoradiation therapy on normal rat brain.* Neurosurgery, 1984. **15**(6): p. 804-10.
107. Wilson, B.C., P.J. Muller, and J.C. Yanch, *Instrumentation and light dosimetry for intra-operative photodynamic therapy (PDT) of malignant brain tumours.* Phys Med Biol, 1986. **31**(2): p. 125-33.
108. Olzowy, B., et al., *Photoirradiation therapy of experimental malignant glioma with 5-aminolevulinic acid.* J Neurosurg, 2002. **97**(4): p. 970-6.
109. Huang, H.C., et al., *Photodynamic Priming Mitigates Chemotherapeutic Selection Pressures and Improves Drug Delivery.* Cancer Res, 2018. **78**(2): p. 558-571.
110. Inglut, C.T., et al., *Photodynamic Priming Modulates Endothelial Cell-Cell Junction Phenotype for Light-activated Remote Control of Drug Delivery.* IEEE J Sel Top Quantum Electron, 2021. **27**(4).
111. Quinlan, J.A., et al., *Carrier-Free, Amorphous Verteporfin Nanodrug for Enhanced Photodynamic Cancer Therapy and Brain Drug Delivery.* Adv Sci (Weinh), 2024. **11**(17): p. e2302872.
112. Huang, H.C., et al., *Photodynamic Therapy Synergizes with Irinotecan to Overcome Compensatory Mechanisms and Improve Treatment Outcomes in Pancreatic Cancer.* Cancer Res, 2016. **76**(5): p. 1066-77.
113. Liang, B.J., et al., *Mechanistic Insights into Photodynamic Regulation of Adenosine 5'-Triphosphate-Binding Cassette Drug Transporters.* ACS Pharmacol Transl Sci, 2021. **4**(5): p. 1578-1587.
114. Profaci, C., et al., *The blood-brain barrier in health and disease: Important unanswered questions.* The Journal of experimental medicine, 2020. **217**(4): p. e20190062.
115. Chen, B., et al., *Combining vascular and cellular targeting regimens enhances the efficacy of photodynamic therapy.* Int J Radiat Oncol Biol Phys, 2005. **61**(4): p. 1216-26.
116. Nordmann, N.J. and A.P. Michael, *5-Aminolevulinic acid radiodynamic therapy for treatment of high-grade gliomas: A systematic review.* Clin Neurol Neurosurg, 2021. **201**: p. 106430.
117. Bunevicius, A., et al., *Sonodynamic therapy for gliomas.* J Neurooncol, 2022. **156**(1): p. 1-10.
118. Liu-Chittenden, Y., et al., *Genetic and pharmacological disruption of the TEAD-YAP complex suppresses the oncogenic activity of YAP.* Genes Dev, 2012. **26**(12): p. 1300-5.
119. Tome-Garcia, J., et al., *Analysis of chromatin accessibility uncovers TEAD1 as a regulator of migration in human glioblastoma.* Nat Commun, 2018. **9**(1): p. 4020.
120. Barrette, A.M., et al., *Anti-invasive efficacy and survival benefit of the YAP-TEAD inhibitor verteporfin in preclinical glioblastoma models.* Neuro Oncol, 2022. **24**(5): p. 694-707.
121. Vigneswaran, K., et al., *YAP/TAZ Transcriptional Coactivators Create Therapeutic Vulnerability to Verteporfin in EGFR-mutant Glioblastoma.* Clin Cancer Res, 2021. **27**(5): p. 1553-1569.

122. Read, R.D., *Repurposing the drug verteporfin as anti-neoplastic therapy for glioblastoma.* Neuro Oncol, 2022. **24**(5): p. 708-710.
123. Al-Moujahed, A., et al., *Verteporfin inhibits growth of human glioma in vitro without light activation.* Sci Rep, 2017. **7**(1): p. 7602.
124. Shah, S.R., et al., *Verteporfin-Loaded Polymeric Microparticles for Intratumoral Treatment of Brain Cancer.* Mol Pharm, 2019. **16**(4): p. 1433-1443.
125. Brodowska, K., et al., *The clinically used photosensitizer Verteporfin (VP) inhibits YAP-TEAD and human retinoblastoma cell growth in vitro without light activation.* Exp Eye Res, 2014. **124**: p. 67-73.
126. Brouwer, N.J., et al., *Targeting the YAP/TAZ Pathway in Uveal and Conjunctival Melanoma With Verteporfin.* Invest Ophthalmol Vis Sci, 2021. **62**(4): p. 3.
127. Feng, J., et al., *Verteporfin, a suppressor of YAP-TEAD complex, presents promising antitumor properties on ovarian cancer.* Onco Targets Ther, 2016. **9**: p. 5371-81.
128. Song, S., et al., *The Hippo Coactivator YAP1 Mediates EGFR Overexpression and Confers Chemoresistance in Esophageal Cancer.* Clin Cancer Res, 2015. **21**(11): p. 2580-90.
129. Wei, H., et al., *Verteporfin suppresses cell survival, angiogenesis and vasculogenic mimicry of pancreatic ductal adenocarcinoma via disrupting the YAP-TEAD complex.* Cancer Sci, 2017. **108**(3): p. 478-487.
130. Obaid, G., et al., *Nanolipid Formulations of Benzoporphyrin Derivative: Exploring the Dependence of Nanoconstruct Photophysics and Photochemistry on Their Therapeutic Index in Ovarian Cancer Cells.* Photochemistry and Photobiology, 2019. **95**(1): p. 364-377.
131. Guirguis, M., et al., *Membrane composition is a functional determinant of NIR-activable liposomes in orthotopic head and neck cancer.* Nanophotonics, 2021. **10**(12): p. 3169-3185.
132. Baglo, Y., et al., *Porphyrin-lipid assemblies and nanovesicles overcome ABC transporter-mediated photodynamic therapy resistance in cancer cells.* Cancer Lett, 2019. **457**: p. 110-118.
133. Michy, T., et al., *Verteporfin-Loaded Lipid Nanoparticles Improve Ovarian Cancer Photodynamic Therapy In Vitro and In Vivo.* Cancers (Basel), 2019. **11**(11): p. 1760.
134. Chen, Y. and T. Li, *Cellular Uptake Mechanism of Paclitaxel Nanocrystals Determined by Confocal Imaging and Kinetic Measurement.* AAPS J, 2015. **17**(5): p. 1126-34.
135. Zhang, Q., et al., *The anticancer efficacy of paclitaxel liposomes modified with low-toxicity hydrophobic cell-penetrating peptides in breast cancer: an in vitro and in vivo evaluation.* RSC Adv, 2018. **8**(43): p. 24084-24093.
136. Inglut, C.T., et al., *Immunological and Toxicological Considerations for the Design of Liposomes.* Nanomaterials (Basel), 2020. **10**(2).
137. Nance, E.A., et al., *A dense poly(ethylene glycol) coating improves penetration of large polymeric nanoparticles within brain tissue.* Sci Transl Med, 2012. **4**(149): p. 149ra119.

138. Thorne, R.G. and C. Nicholson, *In vivo diffusion analysis with quantum dots and dextrans predicts the width of brain extracellular space.* Proc Natl Acad Sci U S A, 2006. **103**(14): p. 5567-72.
139. Banks, W.A., *Characteristics of compounds that cross the blood-brain barrier.* BMC Neurol, 2009. **9 Suppl 1**(Suppl 1): p. S3.
140. Jacob, S., A.B. Nair, and J. Shah, *Emerging role of nanosuspensions in drug delivery systems.* Biomater Res, 2020. **24**: p. 3.
141. Sinha, B., R.H. Muller, and J.P. Moschwitzer, *Bottom-up approaches for preparing drug nanocrystals: formulations and factors affecting particle size.* Int J Pharm, 2013. **453**(1): p. 126-41.
142. Wang, Y., et al., *Stability of nanosuspensions in drug delivery.* J Control Release, 2013. **172**(3): p. 1126-41.
143. Patravale, V.B., A.A. Date, and R.M. Kulkarni, *Nanosuspensions: a promising drug delivery strategy.* J Pharm Pharmacol, 2004. **56**(7): p. 827-40.
144. Lu, Y., et al., *Development and evaluation of transferrin-stabilized paclitaxel nanocrystal formulation.* J Control Release, 2014. **176**: p. 76-85.
145. Capriotti, K. and J. Capriotti, *Dimethyl Sulfoxide: History, Chemistry, and Clinical Utility in Dermatology.* The Journal of Clinical and Aesthetic Dermatology, 2012. **5**(9): p. 24-26.
146. Jacob, S. and D. Wood, *Dimethyl sulfoxide (DMSO). Toxicology, pharmacology, and clinical experience.* American journal of surgery, 1967. **114**(3): p. 414-426.
147. Madsen, B., et al., *Adverse reactions of dimethyl sulfoxide in humans: a systematic review.* F1000Research, 2024. **7**: p. 1746.
148. Rawls, W., L. Cox, and E. Rovner, *Dimethyl sulfoxide (DMSO) as intravesical therapy for interstitial cystitis/bladder pain syndrome: A review.* Neurourology and urodynamics, 2017. **36**(7): p. 1677-1684.
149. Verheijen, M., et al., *DMSO induces drastic changes in human cellular processes and epigenetic landscape in vitro.* Scientific reports, 2019. **9**(1): p. 4641.
150. Brough, C. and R.O. Williams, 3rd, *Amorphous solid dispersions and nano-crystal technologies for poorly water-soluble drug delivery.* Int J Pharm, 2013. **453**(1): p. 157-66.
151. Mullin, J.W., *5. Nucleation*, in *Crystallization (4th Edition)*. Elsevier.
152. Kulkarni, T.A., et al., *A year-long extended release nanoformulated cabotegravir prodrug.* Nat Mater, 2020. **19**(8): p. 910-920.
153. Gautam, N., et al., *Lipophilic nanocrystal prodrug-release defines the extended pharmacokinetic profiles of a year-long cabotegravir.* Nat Commun, 2021. **12**(1): p. 3453.
154. Sillman, B., et al., *Creation of a long-acting nanoformulated dolutegravir.* Nat Commun, 2018. **9**(1): p. 443.
155. Liu, Y., L. Huang, and F. Liu, *Paclitaxel nanocrystals for overcoming multidrug resistance in cancer.* Mol Pharm, 2010. **7**(3): p. 863-9.
156. Harrison, M.R., et al., *A phase II study of 2-methoxyestradiol (2ME2) NanoCrystal(R) dispersion (NCD) in patients with taxane-refractory,*

metastatic castrate-resistant prostate cancer (CRPC). Invest New Drugs, 2011. **29**(6): p. 1465-74.
157. Jarvis, M., V. Krishnan, and S. Mitragotri, *Nanocrystals: A perspective on translational research and clinical studies.* Bioeng Transl Med, 2019. **4**(1): p. 5-16.
158. Junghanns, J.U. and R.H. Muller, *Nanocrystal technology, drug delivery and clinical applications.* Int J Nanomedicine, 2008. **3**(3): p. 295-309.
159. Muller, R.H., C. Jacobs, and O. Kayser, *Nanosuspensions as particulate drug formulations in therapy. Rationale for development and what we can expect for the future.* Adv Drug Deliv Rev, 2001. **47**(1): p. 3-19.
160. Zhou, M., et al., *Recent Advances in Paclitaxel-based Self-Delivery Nanomedicine for Cancer Therapy.* Curr Med Chem, 2021. **28**(31): p. 6358-6374.
161. Gradishar, W.J., et al., *Phase III trial of nanoparticle albumin-bound paclitaxel compared with polyethylated castor oil-based paclitaxel in women with breast cancer.* J Clin Oncol, 2005. **23**(31): p. 7794-803.
162. Yuan, H., et al., *Albumin Nanoparticle of Paclitaxel (Abraxane) Decreases while Taxol Increases Breast Cancer Stem Cells in Treatment of Triple Negative Breast Cancer.* Mol Pharm, 2020. **17**(7): p. 2275-2286.
163. Li, F., et al., *Different Nanoformulations Alter the Tissue Distribution of Paclitaxel, Which Aligns with Reported Distinct Efficacy and Safety Profiles.* Mol Pharm, 2018. **15**(10): p. 4505-4516.
164. Sofias, A.M., et al., *The battle of "nano" paclitaxel.* Adv Drug Deliv Rev, 2017. **122**: p. 20-30.
165. Aveline, B., T. Hasan, and R.W. Redmond, *Photophysical and photosensitizing properties of benzoporphyrin derivative monoacid ring A (BPD-MA).* Photochem Photobiol, 1994. **59**(3): p. 328-35.
166. Calori, I.R., et al., *Self-aggregation of verteporfin in glioblastoma multiforme cells: a static and time-resolved flourescence study.* Dyes and Pigments, 2020. **182**: p. 108598.
167. Brown, S.B., M. Shillcock, and P. Jones, *Equilibrium and kinetic studies of the aggregation of porphyrins in aqueous solution.* Biochem J, 1976. **153**(2): p. 279-85.
168. Aveline, B.M., T. Hasan, and R.W. Redmond, *The effects of aggregation, protein binding and cellular incorporation on the photophysical properties of benzoporphyrin derivative monoacid ring A (BPDMA).* J Photochem Photobiol B, 1995. **30**(2-3): p. 161-9.
169. Danaei, M., et al., *Impact of Particle Size and Polydispersity Index on the Clinical Applications of Lipidic Nanocarrier Systems.* Pharmaceutics, 2018. **10**(2).
170. Richter, A.M., et al., *Biodistribution of tritiated benzoporphyrin derivative (3H-BPD-MA), a new potent photosensitizer, in normal and tumor-bearing mice.* J Photochem Photobiol B, 1990. **5**(2): p. 231-44.
171. Richter, A.M., et al., *Liposomal delivery of a photosensitizer, benzoporphyrin derivative monoacid ring A (BPD), to tumor tissue in a mouse tumor model.* Photochem Photobiol, 1993. **57**(6): p. 1000-6.

172. Siriwardane, D.A., W. Jiang, and T. Mudalige, *Profiling in-vitro release of verteporfin from VISUDYNE(R) liposomal formulation and investigating verteporfin binding to human serum albumin.* Int J Pharm, 2023. **646**: p. 123449.
173. Sirks, M.J., et al., *Clinical impact of the worldwide shortage of verteporfin (Visudyne(R)) on ophthalmic care.* Acta Ophthalmol, 2022. **100**(7): p. e1522-e1532.
174. Reverchon, E., *Supercritical antisolvent precipitation of micro- and nano-particles.* The Journal of Supercritical Fluids, 1999. **15**(1): p. 1-21.
175. Rizvi, I., et al., *A Combination of Visudyne and a Lipid-anchored Liposomal Formulation of Benzoporphyrin Derivative Enhances Photodynamic Therapy Efficacy in a 3D Model for Ovarian Cancer.* Photochem Photobiol, 2019. **95**(1): p. 419-429.
176. Beck, C., S.V. Dalvi, and R.N. Dave, *Controlled liquid antisolvent precipitation using a rapid mixing device.* Chemical Engineering Science, 2010. **65**(21): p. 5669-5675.
177. Thanh, N.T., N. Maclean, and S. Mahiddine, *Mechanisms of nucleation and growth of nanoparticles in solution.* Chem Rev, 2014. **114**(15): p. 7610-30.
178. Ahmadi Tehrani, A., et al., *Formation of nanosuspensions in bottom-up approach: theories and optimization.* Daru, 2019. **27**(1): p. 451-473.
179. Haberkorn, H., et al., *Early stages of particle formation in precipitation reactions-quinacridone and boehmite as generic examples.* J Colloid Interface Sci, 2003. **259**(1): p. 112-26.
180. Murnane, D., C. Marriott, and G.P. Martin, *Developing an environmentally benign process for the production of microparticles: amphiphilic crystallization.* Eur J Pharm Biopharm, 2008. **69**(1): p. 72-82.
181. Zhao, T., et al., *Engineering the protein corona: Strategies, effects, and future directions in nanoparticle therapeutics.* Biomedicine & pharmacotherapy = Biomedecine & pharmacotherapie, 2024. **175**: p. 116627.
182. Yin, Y., Y. Ma, and H. Ding, *Effect of Nanoparticle Curvature on Its Interaction with Serum Proteins.* Langmuir : the ACS journal of surfaces and colloids, 2024. **40**(29): p. 15205-15213.
183. Chen, C., et al., *Physicochemical and biological characterization of the lipid particles with bovine serum albumin corona.* International journal of biological macromolecules, 2024. **281**(Pt 1): p. 136233.
184. Allison, B.A., et al., *The plasma distribution of benzoporphyrin derivative and the effects of plasma lipoproteins on its biodistribution.* Photochem Photobiol, 1990. **52**(3): p. 501-7.
185. Allison, B.A., et al., *The effects of plasma lipoproteins on in vitro tumor cell killing and in vivo tumor photosensitization with benzoporphyrin derivative.* Photochem Photobiol, 1991. **54**(5): p. 709-15.
186. Allison, B.A., P.H. Pritchard, and J.G. Levy, *Evidence for low-density lipoprotein receptor-mediated uptake of benzoporphyrin derivative.* Br J Cancer, 1994. **69**(5): p. 833-9.
187. Houle, J.M. and A. Strong, *Clinical pharmacokinetics of verteporfin.* J Clin Pharmacol, 2002. **42**(5): p. 547-57.

188. Sasaki, T., et al., *Effect of Proton Pump Inhibitors on Colorectal Cancer.* Int J Mol Sci, 2020. **21**(11): p. 3877.
189. Vaubel, R.A., et al., *Genomic and Phenotypic Characterization of a Broad Panel of Patient-Derived Xenografts Reflects the Diversity of Glioblastoma.* Clin Cancer Res, 2020. **26**(5): p. 1094-1104.
190. Liang, B.J., et al., *Fluorescence-guided photoimmunotherapy using targeted nanotechnology and ML7710 to manage peritoneal carcinomatosis.* Sci Adv, 2023. **9**(36): p. eadi3441.
191. Busetti, A., et al., *High efficiency of benzoporphyrin derivative in the photodynamic therapy of pigmented malignant melanoma.* Br J Cancer, 1999. **79**(5-6): p. 821-4.
192. Gupta, A., et al., *Brain distribution of cetirizine enantiomers: comparison of three different tissue-to-plasma partition coefficients: K(p), K(p,u), and K(p,uu).* Drug Metab Dispos, 2006. **34**(2): p. 318-23.
193. Diehl, K., et al., *A good practice guide to the administration of substances and removal of blood, including routes and volumes.* Journal of applied toxicology : JAT, 2001. **21**(1): p. 15-23.
194. Loryan, I., et al., *Unbound Brain-to-Plasma Partition Coefficient, K(p,uu,brain)-a Game Changing Parameter for CNS Drug Discovery and Development.* Pharm Res, 2022. **39**(7): p. 1321-1341.
195. Wu, J., *The Enhanced Permeability and Retention (EPR) Effect: The Significance of the Concept and Methods to Enhance Its Application.* Journal of personalized medicine, 2021. **11**(8).
196. Steeg, P.S., *The blood-tumour barrier in cancer biology and therapy.* Nat Rev Clin Oncol, 2021. **18**(11): p. 696-714.
197. Richter, A.M., et al., *Photosensitising potency of structural analogues of benzoporphyrin derivative (BPD) in a mouse tumour model.* Br J Cancer, 1991. **63**(1): p. 87-93.
198. Miller, C.R., et al., *Liposome-cell interactions in vitro: effect of liposome surface charge on the binding and endocytosis of conventional and sterically stabilized liposomes.* Biochemistry, 1998. **37**(37): p. 12875-83.
199. Kim, M.M., et al., *National Cancer Institute Collaborative Workshop on Shaping the Landscape of Brain Metastases Research: challenges and recommended priorities.* Lancet Oncol, 2023. **24**(8): p. e344-e354.
200. Bechet, D., et al., *Photodynamic therapy of malignant brain tumours: a complementary approach to conventional therapies.* Cancer Treat Rev, 2014. **40**(2): p. 229-41.
201. Davis, R., et al., *Surgical Inflammation Alters Immune Response to Intraoperative Photodynamic Therapy.* Cancer research communications, 2023. **3**(9): p. 1810-1822.
202. Pan, Y., et al., *Athymic mice reveal a requirement for T-cell-microglia interactions in establishing a microenvironment supportive of Nf1 low-grade glioma growth.* Genes & development, 2018. **32**(7-8): p. 491-496.
203. Andersen, R., et al., *Tumor-Associated Microglia and Macrophages in the Glioblastoma Microenvironment and Their Implications for Therapy.* Cancers, 2021. **13**(17): p. 4255.

204. Li, F., et al., *Photodynamic therapy boosts anti-glioma immunity in mice: a dependence on the activities of T cells and complement C3.* Journal of cellular biochemistry, 2011. **112**(10): p. 3035-3043.
205. Letchuman, V., et al., *Syngeneic murine glioblastoma models: reactionary immune changes and immunotherapy intervention outcomes.* Neurosurgical focus, 2022. **52**(2): p. E5.
206. Munegowda, M., et al., *Efficacy of ruthenium coordination complex-based Rutherrin in a preclinical rat glioblastoma model.* Neuro-oncology advances, 2019. **1**(1): p. vdz006.
207. Fisher, C., et al., *ALA-PpIX mediated photodynamic therapy of malignant gliomas augmented by hypothermia.* PloS one, 2017. **12**(7): p. e0181654.
208. Semyachkina-Glushkovskaya, O., et al., *Photodynamic opening of blood-brain barrier.* Biomedical Optics Express, 2017. **8**(11): p. 5040-5048.
209. Kovacs, Z.I., et al., *Disrupting the blood-brain barrier by focused ultrasound induces sterile inflammation.* Proc Natl Acad Sci U S A, 2017. **114**(1): p. E75-E84.
210. Ji, Y., et al., *Toxicity of photodynamic therapy with photofrin in the normal rat brain.* Lasers Surg Med, 1994. **14**(3): p. 219-28.
211. Winkelman, J.W. and G.H. Collins, *Neurotoxicity of tetraphenylporphinesulfonate TPPS4 and its relation to photodynamic therapy.* Photochem Photobiol, 1987. **46**(5): p. 801-7.
212. Madsen, S.J. and H. Hirschberg, *Site-specific opening of the blood-brain barrier.* J Biophotonics, 2010. **3**(5-6): p. 356-67.
213. Ghasemi, M., et al., *The MTT Assay: Utility, Limitations, Pitfalls, and Interpretation in Bulk and Single-Cell Analysis.* Int J Mol Sci, 2021. **22**(23).
214. Rahman, I., et al., *Photodynamic priming modulates cellular ATP levels to overcome P-glycoprotein-mediated drug efflux in chemoresistant triple-negative breast cancer.* Photochemistry and photobiology, 2024.
215. Rytlewski, J.D., et al., *Photodynamic Therapy Using Hippo Pathway Inhibitor Verteporfin: A Potential Dual Mechanistic Approach in Treatment of Soft Tissue Sarcomas.* Cancers (Basel), 2021. **13**(4): p. 675.
216. Jeising, S., et al., *In-Vitro Use of Verteporfin for Photodynamic Therapy in Glioblastoma.* Photodiagnosis Photodyn Ther, 2022. **40**: p. 103049.
217. Song, M., et al., *Combination of Molecule-Targeted Therapy and Photodynamic Therapy Using Nanoformulated Verteporfin for Effective Uveal Melanoma Treatment.* Mol Pharm, 2024. **21**(5): p. 2340-2350.
218. Baskaran, R., J. Lee, and S. Yang, *Clinical development of photodynamic agents and therapeutic applications.* Biomaterials research, 2018. **22**: p. 25.
219. Feitsma, H. and E. Cuppen, *Zebrafish as a cancer model.* Molecular cancer research : MCR, 2008. **6**(5): p. 685-694.
220. Mione, M. and N. Trede, *The zebrafish as a model for cancer.* Disease models & mechanisms, 2010. **3**(9-10): p. 517-523.
221. Almstedt, E., et al., *Real-time evaluation of glioblastoma growth in patient-specific zebrafish xenografts.* Neuro-oncology, 2022. **24**(5): p. 726-738.

222. Ai, X., et al., *Clinically relevant orthotopic xenograft models of patient-derived glioblastoma in zebrafish.* Disease Models & Mechanisms, 2024. **15**(4): p. dmm049109.
223. Pudelko, L., et al., *An orthotopic glioblastoma animal model suitable for high-throughput screenings.* Neuro-oncology, 2018. **20**(11): p. 1475-1484.
224. Schinkel, A.H., et al., *Disruption of the mouse mdr1a P-glycoprotein gene leads to a deficiency in the blood-brain barrier and to increased sensitivity to drugs.* Cell, 1994. **77**(4): p. 491-502.
225. Kodaira, H., et al., *Kinetic analysis of the cooperation of P-glycoprotein (P-gp/Abcb1) and breast cancer resistance protein (Bcrp/Abcg2) in limiting the brain and testis penetration of erlotinib, flavopiridol, and mitoxantrone.* J Pharmacol Exp Ther, 2010. **333**(3): p. 788-96.
226. Wang, J., et al., *P-glycoprotein (MDR1/ABCB1) and Breast Cancer Resistance Protein (BCRP/ABCG2) affect brain accumulation and intestinal disposition of encorafenib in mice.* Pharmacol Res, 2018. **129**: p. 414-423.
227. Bakhsheshian, J., et al., *Bioluminescent imaging of drug efflux at the blood-brain barrier mediated by the transporter ABCG2.* Proc Natl Acad Sci U S A, 2013. **110**(51): p. 20801-6.
228. England, C.G., E.B. Ehlerding, and W. Cai, *NanoLuc: A Small Luciferase Is Brightening Up the Field of Bioluminescence.* Bioconjug Chem, 2016. **27**(5): p. 1175-1187.
229. Heise, K., et al., *Dual luciferase assay for secreted luciferases based on Gaussia and NanoLuc.* Assay Drug Dev Technol, 2013. **11**(4): p. 244-52.
230. Francis, W.R., et al., *Occurrence of Isopenicillin-N-Synthase Homologs in Bioluminescent Ctenophores and Implications for Coelenterazine Biosynthesis.* PLoS One, 2015. **10**(6): p. e0128742.
231. Su, Y., et al., *Novel NanoLuc substrates enable bright two-population bioluminescence imaging in animals.* Nat Methods, 2020. **17**(8): p. 852-860.
232. Su, Y., et al., *An optimized bioluminescent substrate for non-invasive imaging in the brain.* Nat Chem Biol, 2023. **19**(6): p. 731-739.
233. Huang, R., et al., *ATP-binding cassette transporters modulate both coelenterazine- and D-luciferin-based bioluminescence imaging.* Mol Imaging, 2011. **10**(3): p. 215-26.
234. Robey, R.W., et al., *Inhibition of P-glycoprotein (ABCB1)- and multidrug resistance-associated protein 1 (ABCC1)-mediated transport by the orally administered inhibitor, CBT-1((R)).* Biochem Pharmacol, 2008. **75**(6): p. 1302-12.
235. Basnet, R.M., et al., *Zebrafish Larvae as a Behavioral Model in Neuropharmacology.* Biomedicines, 2019. **7**(1): p. 23.
236. Reside, A.M., et al., *Behavior and brain size of larval zebrafish exposed to environmentally relevant concentrations of beta-methylamino-l-alanine.* Toxicol Sci, 2023. **193**(1): p. 80-89.
237. Kimmel, C., et al., *Stages of embryonic development of the zebrafish.* Developmental dynamics : an official publication of the American Association of Anatomists, 1995. **203**(3): p. 253-310.

238. Gosselet, F., et al., *Central nervous system delivery of molecules across the blood-brain barrier.* Neurochem Int, 2021. **144**: p. 104952.
239. Bhowmik, A., R. Khan, and M.K. Ghosh, *Blood brain barrier: a challenge for effectual therapy of brain tumors.* Biomed Res Int, 2015. **2015**: p. 320941.
240. Luissint, A.C., et al., *Tight junctions at the blood brain barrier: physiological architecture and disease-associated dysregulation.* Fluids Barriers CNS, 2012. **9**(1): p. 23.
241. Begley, D.J., *ABC transporters and the blood-brain barrier.* Curr Pharm Des, 2004. **10**(12): p. 1295-312.
242. Choi, C.H., *ABC transporters as multidrug resistance mechanisms and the development of chemosensitizers for their reversal.* Cancer Cell Int, 2005. **5**: p. 30.
243. Shukla, S., S. Ohnuma, and S.V. Ambudkar, *Improving cancer chemotherapy with modulators of ABC drug transporters.* Curr Drug Targets, 2011. **12**(5): p. 621-30.
244. Anreddy, N., et al., *Tyrosine kinase inhibitors as reversal agents for ABC transporter mediated drug resistance.* Molecules, 2014. **19**(9): p. 13848-77.
245. Gasca-Salas, C., et al., *Blood-brain barrier opening with focused ultrasound in Parkinson's disease dementia.* Nat Commun, 2021. **12**(1): p. 779.
246. Rezai, A.R., et al., *Noninvasive hippocampal blood-brain barrier opening in Alzheimer's disease with focused ultrasound.* Proc Natl Acad Sci U S A, 2020. **117**(17): p. 9180-9182.
247. de Gooijer, M.C., et al., *ATP-binding cassette transporters restrict drug delivery and efficacy against brain tumors even when blood-brain barrier integrity is lost.* Cell Rep Med, 2021. **2**(1): p. 100184.
248. Goutal, S., et al., *Physical blood-brain barrier disruption induced by focused ultrasound does not overcome the transporter-mediated efflux of erlotinib.* J Control Release, 2018. **292**: p. 210-220.
249. Goutal, S., et al., *Imaging the impact of blood-brain barrier disruption induced by focused ultrasound on P-glycoprotein function.* J Control Release, 2023. **361**: p. 483-492.
250. Montanari, F. and G.F. Ecker, *Prediction of drug-ABC-transporter interaction--Recent advances and future challenges.* Adv Drug Deliv Rev, 2015. **86**: p. 17-26.
251. Stouch, T.R. and O. Gudmundsson, *Progress in understanding the structure-activity relationships of P-glycoprotein.* Adv Drug Deliv Rev, 2002. **54**(3): p. 315-28.
252. Aazmi, A., et al., *Vascularizing the brain in vitro.* iScience, 2022. **25**(4): p. 104110.
253. Alomari, S., et al., *Implementation of Minimally Invasive Brain Tumor Resection in Rodents for High Viability Tissue Collection.* J Vis Exp, 2022(183): p. 183.
254. Duvernoy, H., S. Delon, and J.L. Vannson, *The vascularization of the human cerebellar cortex.* Brain Res Bull, 1983. **11**(4): p. 419-80.